Submesoscale processes in the Baltic Sea

Evridiki Chrysagi

Dissertation zur Erlangung des akademischen Grades
doctor rerum naturalium (Dr. rer. nat.) der
Mathematisch-Naturwissenschaftlichen Fakultät
der Universität Rostock

August, 2020

And I think to myself what a wonderful world ...

Gutachter:

1. Prof. Dr. Hans Burchard
   Leibniz-Institut für Ostseeforschung Warnemünde
2. Prof. Dr. .....
   .....

Jahr der Einreichung: 2020

Jahr der Verteidigung: 2020

Eidesstattliche Erklärung

Hiermit erkläre ich an Eides statt, dass ich die vorliegende Dissertationsschrift - abgesehen von der Beratung durch meine akademischen Lehrer - selbst verfasst und keine anderen als die angegebenen Quellen und Hilfsmittel benutzt habe. Diese Arbeit hat weder ganz, noch in Teilen, bereits an anderer Stelle einer Promotionskommission zur Erlangung des Doktorgrades vorgelegen.

Evridiki Chrysagi

Rostock, August 2020

Acknowledgements

First and foremost, I would like to express my sincere gratitude to my supervisor, Hans Burchard. Thank you for always being there for me when I needed you most. For your support and guidance but also for being such a passionate, calm, and optimistic person. Besides my supervisor, I would like to sincerely thank Lars Umlauf for his scientific assistance and his willingness to answer my endless questions. This work would have not been possible without their help. Thank you also for giving me the opportunity to participate in the research cruise in the Baltic Sea. It was a unique experience that I will never forget.

I am grateful to Jeff Carpenter for the time he made available to me and for his inspiring ideas and to Joachim Dippner for the fruitful collaboration. A special thanks to Peter Holtermann for helping me throughout this thesis, to Knut Klingbeil and Ulf Gräwe for their support with the numerical simulations, as well as to Fatemeh Chegini and Berkay Basdurak for all the great discussions. Moreover, I have to mention how grateful I am to Mahdi Aragh for the never-ending scientific discussions, especially during the smoking time, and the long walks during the period of Coronavirus. My sincere thanks to Jen-Ping Peng for making this PhD journey together, to all the PhD students (Marvin Lorenz, Madline Kniebusch, Selina Müller) and all my colleagues in the Leibniz Institute for Baltic Sea Research for the wonderful memories. This work was supported by project T2 (Energy Budget of the Ocean Surface Mixed Layer) of the Collaborative Research Centre TRR-181 on "Energy Transfers in Atmosphere and Ocean", funded by the German Research Foundation, project number 274762653. I am grateful for being part of such an interdisciplinary and multicultural project that provided so many seminars, meetings, and winter schools.

Finally, I would like to thank my family and all my friends back home who, despite being away for so long, they always made me feel that nothing has changed. Thank you for your continued support, for your patience and understanding. But above all thank you for your love.

Zusammenfassung

Jüngste Fortschritte in der hochauflösenden Ozeanmodellierung haben eine neue Klasse von turbulenten Wasserbewegungen, die sogenannte Submesoskale, enthüllt. Die Submesoskale beschreibt relativ kurzlebige Strömungsmuster, die in Form von Wirbeln, Fronten und Filamenten mit horizontalen Skalen zwischen 0.1-10 km und Zeitskalen zwischen Stunden zu Tagen auftreten und typischerweise in der Nähe von größerskaligen Dichtefronten zu finden sind. Das wissenschaftliche Interesse an der Submesoskale, die vor allem in der durchmischten Ozeandeckschicht auftritt, liegt in ihrer Rolle als Prozess des Energietransfers innerhalb der Energiekaskade von geostropher Energie zu kleineren Skalen hin. Weiterhin beeinflusst sie auch die Schichtung des oberen Ozeans, sowie den vertikalen Transport von gelösten Stoffen, was von großer Bedeutung für die marine Biogeochemie ist. Submesoskalige Prozesse können den oberen Ozean durch den Transport von warmem Wasser über kälteres restratifizieren, und so die Tiefe der durchmischten Deckschicht verringern. Untersucht wurde die Submesoskale bis jetzt hauptsächlich in Konfigurationen eines offenen oder idealisierten Ozeans, wobei es noch Fragen bezüglich des Verhaltens bei starker Abkühlung sowie Stürmen gibt. Durch ihre relative leichte Erreichbarkeit wird in dieser Arbeit daher die zentrale Ostsee als natürliches Labor zur Untersuchung der Turbulenz- und Restratifizierungsprozesse durch submesoskalige Prozesse während des Durchzugs mehrerer Stürme genutzt. Hierfür wird ein realistisches, hochauflösendes numerisches Modell der zentralen Ostsee angewendet und die Modellergebnisse mit Fokus auf das östliche Gotlandbecken ausgewertet, da Felddaten in diesem Bereich starke horizontale Dichtegradienten nachgewiesen haben. Die Modellergebnisse zeigen eine starke thermische Frontstruktur, die das gesamte Becken umfasst, aber trotz ihres Auftretens über den gesamten Herbst noch nicht umfassend beschrieben worden ist. Diese großskalige Front bildet energetische submesoskalige Strukturen aus, die sich als langgezogene Filamente und Fronten mit scharfen horizontalen Dichtegradienten, starken Oberflächendivergenzen und erhöhten vertikalen Geschwindigkeiten manifestieren. Die Oberflächensignale dieser Strukturen finden sich auch in der Tiefe der durchmischten Deckschicht wieder, die eine hohe räumliche und zeitliche Variabilität aufweist. Eines der

Hauptresultate dieser Arbeit ist neben der Rolle der Submesoskale als Prozess der schnellen Restratifizierung die Eigenschaft trotz eines Sturms relative flache durchmischte Deckschichten zu erhalten. Diese Restratifizierungsprozesse kompensieren die durch Abkühlung und Windstress erzeugte Durchmischung, und erzeugen so lokale Gebiete von stabil geschichteten Wassermassen.

Abstract

Recent advances in high-resolution numerical modeling of the ocean have revealed a new class of turbulent motion, the so-called submesoscales. Submesoscales are intermediate -scale ephemeral flow structures in the form of vortices, fronts, and filaments with horizontal scales of 0.1-10 km and lifetimes of hours to days, emerging typically in the vicinity of larger scale density fronts. These motions, abundant in the oceanic surface mixed layer, have drawn the attention due to their role on the downscale cascade of geostrophic energy but also due to their ability to change the upper ocean stratification and induce high vertical velocities, both being instrumental for marine biogeochemistry. Submesoscales can restratify, i.e., bring warm water above cold water and reduce the depth of the mixed layer. Those motions have been studied mainly in the context of open ocean simulations and idealized configurations; however, their response during excessive cooling and strong winds, is still unclear. Here, the easily accessible central basin of the Baltic Sea is used as a natural laboratory to study the effect of submesoscale features on the restratification process and near-surface turbulence during the passage of multiple storm events. A realistic high-resolution numerical simulation is used, focusing on the Eastern Gotland Basin, a possible hotspot of submesoscale genesis, with persistent horizontal gradients, as evidenced by field observations. The simulations revealed the existence of a strong thermal frontal structure that covers the entire basin and despite its persistence throughout the autumn period, it has not been reported previously. Cold elongated submesoscale filaments and fronts with sharp horizontal buoyancy gradients, strong surface convergence, and intense vertical velocities arise from this energetic frontal pattern. The surface signature of those features appears also in mixed layer depth, which presents shallow and highly heterogeneous spatial patterns with significant temporal variability. As one of the main results, submesoscales were found not only to induce vigorous and rapid restratification after each wind event but also to maintain shallow mixed layers during storms. Submesoscale restratification compensates for the destratification effect caused by atmospheric buoyancy loss and wind-induced mixing, resulting in stably stratified patches.

Contents

CHAPTER 1

Introduction

Increased resolution in satellite images and numerical ocean models has recently revealed a new class of turbulent motion, confined to the weakly stratified upper ocean, the so-called submesoscales. Submesoscales have drawn the attention due to their crucial role in several physical and biological processes. First, this newly discovered regime has been proposed as a mediator in the down-scale cascade of geostrophic energy. Second, the exclusively high vertical velocities in submesoscale fronts and filaments have been seen to enhance the vertical transport of heat, nutrients, and dissolved gases such as carbon dioxide, thereby connecting the oceanic interior with the surface layer. Different kinds of instabilities along with interleavings, intrusions, strong turbulence and, mixing are typically present in frontal sites. There, the dynamical slumping of isopycnals abruptly changes the mixed layer depth, raising questions regarding its misrepresentation in climate models, where the absence of these subgrid-scale processes can cause significant biases. Although all the above processes are not yet well-understood, it has been suggested that submesoscales might constitute a key component of the Earth's climate. This work tries to shed some light on the modifying effects of submesoscales on upper-ocean stratification and near-surface turbulence during a series of storm events. Using the Baltic Sea as a natural laboratory, new insights are also provided regarding the potential significance of fronts in this brackish marine system.

1.1 Background and motivation

The upper ocean is characterized by a Surface Mixed Layer (SML) with a typical thickness from a few meters to several hundred meters. Being in direct contact with the atmosphere, energetic turbulence driven by winds and atmospheric buoyancy fluxes keeps this layer well-mixed, allowing only a weak density stratification (Garrett, 1996). The oceanic SML is an important region since it controls the exchange of energy, mass, momentum, and heat between the atmosphere and the ocean and can hence, in the long-term mean, regulate the Earth's climate. It is also a biologically important area since it determines the availability of light and nutrients, necessary for primary production and phytoplankton bloom formation. Below the SML, temperature, salinity, and density change rapidly with depth forming the well-known thermocline, halocline, and pycnocline respectively, where turbulence is damped by the increased vertical stratification.

The traditional view of the upper ocean density stratification considers only vertical processes, such as the fluxes of momentum, heat, and freshwater that compete either to destroy or increase the vertical stratification, ignoring the contribution from lateral processes (Large et al., 1994; Umlauf and Burchard, 2005). Yet, as illustrated in Figure 1.1 the SML is a quite complex region, hosting a vast amount of dynamical processes, unique to this layer, such as inertial oscillations, frontal instabilities, and Langmuir turbulence. The pathways of energy, momentum, and tracers in this layer are quite complicated, highly variable, and not sufficiently understood.

Increased resolution in satellite images and numerical ocean models has recently revealed a new dynamical regime, confined to the weakly stratified SML, the so-called submesoscales. Submesoscales are ubiquitous in the oceanic SML (Capet et al., 2008a; McWilliams, 2016) and the motivation of studying them arises from different factors such as their importance for SML restratification (Tandon and Garrett, 1994; Boccaletti et al., 2007; Fox-Kemper et al., 2008) and near-surface biogeochemistry in localized regions (Nurser and Zhang, 2000; Taylor and Ferrari, 2011; Mahadevan, 2016), as well as their role in the energy cascade (Capet et al., 2008c; Molemaker et al., 2010; Brüggemann and Eden, 2015).

Submesoscales are ephemeral features in the form of vortices, fronts, and filaments with horizontal scales of 0.1-10 km and lifetimes of hours to days, concentrating mainly in the upper ocean, where lateral density gradients are more abundant (Thomas et al.,

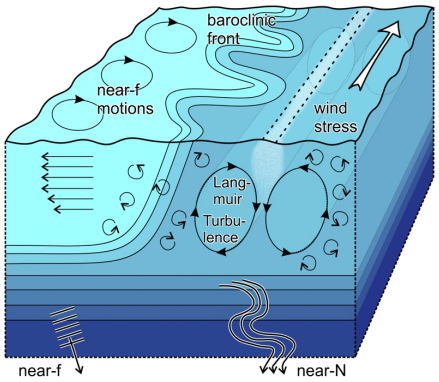

Figure 1.1: Processes in the oceanic surface mixed layer associated with small-scale turbulence. From left to right: inertial oscillations, different wind-driven currents, SML frontal instabilities, and Langmuir turbulence. Internal waves near the inertial and buoyancy frequencies that may be triggered by motions in the SML are also visible at the bottom of the figure. Figure obtained from the Collaborative Research Center TRR-181 proposal on "Energy Transfers in Atmosphere and Ocean", University of Hamburg, 2016.

2013a). These motions present sharp lateral buoyancy gradients, a clear ageostrophic nature with a preference for cyclonic vorticities over anticyclonic, along with strong surface convergence and associated downwelling velocities. Submesoscales emerge spontaneously mainly in the vicinity of mesoscale eddies and strong boundary currents (McWilliams, 2016). Stirring and straining by mesoscale eddies have been seen to contribute to the development of cold elongated submesoscale filaments (Lapeyre and Klein, 2006; Gula et al., 2014), while recent studies (e.g., Brannigan et al., 2017) have shown that submesoscale instabilities can even occur inside mesoscale eddies.

Mixed layer instabilities and strain-induced frontogenesis have been suggested as the main generation mechanisms of surface submesoscale flows (McWilliams, 2016). Submesoscales draw their energy from the available potential energy stored in fronts. Meanders and eddies are developing along fronts, by converting the potential energy residing in the density structure to kinetic energy, while increasing the SML stratification by tilting the nearly vertical isopycnals towards the horizontal. This submesoscale restratification is an important dynamical process, typically ignored in numerical models. As a consequence, ocean models usually present a bias on the representation of Mixed Layer Depth (MLD) (Fox-Kemper et al., 2008) which along with the misrepresentation of the upward heat transport caused by submesoscales (Su et al., 2018), can significantly impact the predictability of climate models.

The ubiquity of submesoscales in the world's upper ocean was first seen from space. By exploiting sun-glint on the sea surface, photographs from space shuttles and synthetic aperture radar (SAR) images revealed a plethora of eddies and linear features that Munk et al. (2000) referred to as "spirals on the sea" (Figure 1.2). Those spirals, visible due to strong surface convergence of surfactants, have short lifetimes, sizes of a few km and they are overwhelmingly cyclonic. A dominance of submesoscale currents was found in most of those sun-glint images although mesoscale patterns were also present (McWilliams, 2016). A characteristic example showing a richness of spirals and filaments along with a pair of interconnected vortices can be seen in Figure 1.2. The image was taken in the Mediterranean Sea after an episode of strong winds and is indicative of the role of atmospheric forcing on energizing those features (see Section 1.3.3).

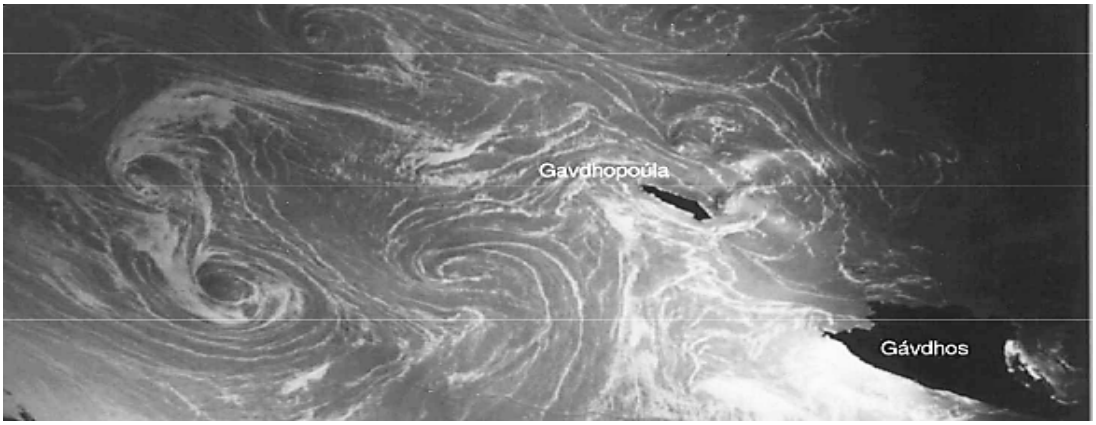

Figure 1.2: Spirals on the sea. A pair of interconnected spirals formed in the Mediterranean Sea, south of Crete island (34.5°N, 24.0°E) in Greece, is visible. The vortex pair presents a stagnation point between the two spirals, the cores of which are aligned with the preconditioning northern wind field (Etesian winds). The image was obtained during the low wind conditions that followed the "Etesian" northern wind system. The sun-glint image was taken by the astronaut Scully-Power from the Shuttle mission on 7 October 1984. Sun-glint and radar backscatter images make the strain patterns visible by exploiting the differential surface roughness that develops when surfactants, originating either from biological activities or oil-spills, are gathered by surface straining into coherent features (Munk et al., 2000).

Although submesoscales are ubiquitous in the SML due to the presence of horizontal density gradients, vertical shear, and weak stratification, recent studies suggest that they can also be found in the deeper layers. While observational evidence for submesoscale generation in the ocean interior is still largely lacking (McWilliams, 2016), realistic simulations of the Antarctic Circumpolar Current performed by Siegelman (2020)

showed that the interior of the ocean, down to 900 m depth, is strongly ageostrophic, presenting numerous submesoscale fronts, filaments, and vortices. This aspect is quite different from the traditional view of a quasigeostrophic balanced ocean interior. Close to the bottom boundary layer, flow-topography interactions can lead to vorticity generation and submesoscale formation, providing a new additional pathway for the dissipation of geostrophic energy (Gula et al., 2015).

Focusing on the oceanic surface layer, another motivation for studying the submesoscale flows apart from their role on MLD and near-surface biogeochemistry is their role on the cascade of geostrophic energy. It is well-known that oceanic motions cover a wide range of spatial and temporal scales, encompassing large-scale dynamical processes that can last hundreds of years and extend up to several kilometers, along with small-scale phenomena with short lifetimes that take place to centimeter scale. Most of the ocean's kinetic energy resides at mesoscale and larger scales (Thomas et al., 2013a). At these scales, the flow is considered to be two-dimensional and is characterized by quasi-geostrophic dynamics, that is known to exhibit an inverse energy cascade, i.e., energy moves upscale (excluding potential dissipation near boundaries) (Charney, 1971). In contrast, the smaller three-dimensional turbulent flow manifests a forward cascade of energy, with the kinetic energy being transferred from the larger towards the smaller dissipation scales, where conversion into heat becomes finally possible.

Given that in geostrophic turbulence the energy moves upscale towards the larger scales, and that the dissipation of energy occurs at the smallest scales, the question that arises here is how can this geostrophically-balanced energy be dissipated. Although several dissipation mechanisms have been proposed (McWilliams, 2016) such as bottom friction, lee-wave generation over topography, and the more recent route to dissipation through anticyclonic, ageostrophic instabilities (Molemaker et al., 2005), it remains unclear whether these processes are sufficient to counter-balance the energy input from the atmospheric forcing and tides (Ferrari and Wunsch, 2009).

It is only recently that submesoscales have been proposed as a pathway for the forward cascade of geostrophic energy (Capet et al., 2008c; Molemaker et al., 2010; Brüggemann and Eden, 2015). This intermediate class of turbulent motion lies between the mesoscale regime and the small scale three-dimensional turbulence, and albeit being partly constrained by geostrophic and hydrostatic balance, it is able to breakdown the balance and exhibits a downscale energy flux towards dissipation and diapycnal mixing (McWilliams, 2016).

Contrary to mesoscale dynamics, where planetary rotation constrains the flow and vertical stratification dominates, the Rossby (Ro) and balanced Richardson (Ri_b) numbers,

$$\mathrm{Ro} = \frac{\zeta}{f}, \quad \mathrm{Ri}_b = \frac{f^2 N^2}{|\nabla_h b|^2}\ , \tag{1.1}$$

are both $\mathcal{O}(1)$ in submesoscale flows (Thomas et al., 2013a). Here, f denotes the planetary vorticity; $\zeta = v_x - u_y$ the vertical component of the relative vorticity, with x and y indexes denoting partial derivatives; $N^2 = \partial b/\partial z$ the square of the buoyancy frequency, where $b = -g(\rho - \rho_0)/\rho_0$ is the buoyancy based on the (potential) density ρ (g is the gravitational acceleration, and ρ_0 a constant reference density); and ∇_h is the horizontal nabla operator. In this thesis, submesoscales will be defined as those flows where the Ro and Ri_b numbers are $\mathcal{O}(1)$. The $\mathrm{Ro} \sim 1$ implies departure from geostrophically balanced dynamics (Molemaker et al., 2010), which assumes $\mathrm{Ro} \ll 1$. This allows the development of a more ageostrophic circulation that despite being partly influenced by Earth's rotation and density stratification (Sullivan and McWilliams, 2018) presents much higher vertical velocities.

In fact, the vertical velocities in the submesoscale regime can be an order of magnitude larger than those induced by mesoscale flows, reaching up to $\sim$ 100 m day^{-1}. Their exceptionally high vertical velocities, the short timescales on which they evolve, and their ability to restratify the SML, makes submesoscales particularly important for gas exchange with the atmosphere and primary production (Klein and Lapeyre, 2009; Lévy et al., 2012; Mahadevan, 2016). Specifically, the strong submesoscale vertical velocities can transport nutrients into the euphotic zone, whereas the dynamical restratification of the SML can decrease the vertical mixing and increase the light exposure with both mechanisms being able to trigger phytoplankton blooms (Taylor and Ferrari, 2011; Lévy et al., 2012). Phytoplankton patchiness, caused by processes such as horizontal stirring and vertical transport of nutrients within submesoscales is present in many satellite images and has been extensively studied (Lapeyre and Klein, 2006; Klein and Lapeyre, 2009; Mahadevan, 2016).

Focusing on the Baltic Sea, a close coupling between physical and biological processes can generally be found due to its shallow depths, irregular bathymetry, and complicated vertical stratification (Kahru et al., 1984). In this brackish marine system, frontal regions are abundant and can act as hotspots of biological activity (Figure 1.3). A number of earlier studies (see e.g., Kahru et al., 1984; Kononen and Nômmann, 1992)

pointed out that fronts in the Baltic Sea are associated with increased primary productivity and elevated zooplankton abundance, whilst playing a crucial role in cyanobacterial bloom formation. More recently, high-resolution satellite images from the Baltic Sea revealed a plethora of submesoscale patterns through their imprint on the fine-scale structuring of cyanobacteria blooms. Figure 1.3 shows that high plankton concentrations coincide with the convergence zones developed inside strong filamentary and frontal features. The richness of these features is such that McWilliams (2016) is referred to as "submesoscale soup". Isolated submesoscale coherent vortices can also be found in the basin, consisting of spiral arms shaped by dense elongated filaments (Figure 1.3).

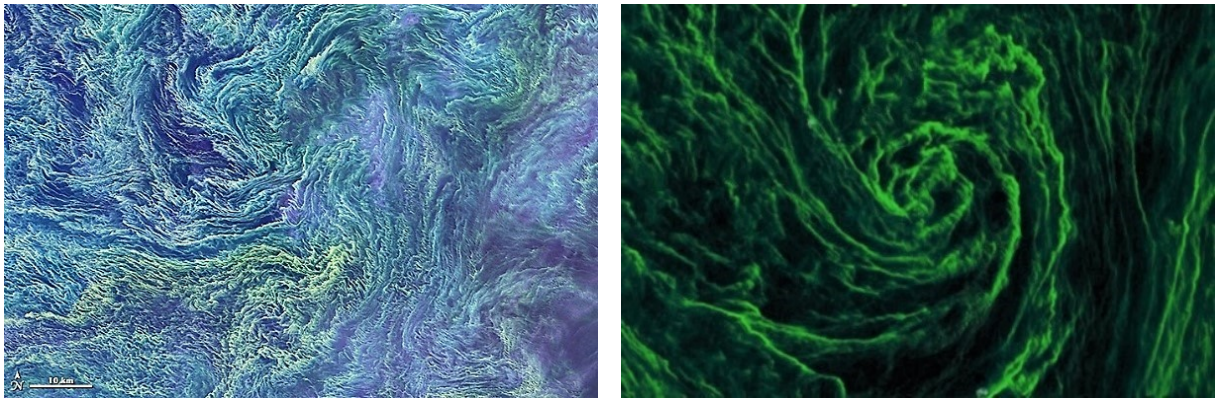

Figure 1.3: Submesoscale patterns in the Baltic Sea identified from their imprint on oceanic biochemistry. Left: Satellite image showing a large bloom of cyanobacteria that occurred inside the "submesoscale soup" formed by multiple frontal and filamentary features, on 11 August 2015 (see Landsat image gallery: https://landsat.visibleearth.nasa.gov/view.php?id=86449). Right: Cyclonic spiral vortex visible from the increased plankton concentration on the regions of strong surface convergence (McWilliams, 2019).

Those images indicate that persistent SML fronts in the Baltic Sea are omnipresent, associated with a wealth of submesoscale features, which suggests that this semi-enclosed brackish system forms an ideal natural laboratory for the study of submesoscale dynamics. The existence of thermohaline fronts is actually a characteristic feature of the Baltic Sea, where complicated lateral and vertical mixing processes between water masses with different characteristics contribute to the formation of its brackish waters (Kahru et al., 1984). Despite the ubiquity of SML fronts and submesoscale features in this non-tidal basin and their well-known implications for SML energetics and biogeochemistry in other marine systems, their properties and dynamics are still largely unexplored in the case of the Baltic Sea.

Motivated by these satellite observations that confirm the existence of persistent lateral density gradients, high-resolution hindcast numerical simulations were conducted in this thesis for studying the submesoscale motions. The numerical simulations were complemented by high-resolution turbulence microstructure data collected across frontal and filamentary features during a field campaign in the easily accessible central basin of the Baltic Sea. The focus is specifically the Eastern Gotland Basin that as will be shown is characterized by a strong and persistent autumn front that acts as a hotspot of submesoscale activity. Cold elongated submesoscale features arise in the vicinity of this front that shallow the MLD and increase the stratification in the SML. The thesis aims at exploring the effects of submesoscale features on near-surface turbulence and MLD variations during the passage of successive storms. It provides also new insights into the potential significance of fronts in the Baltic Sea, where turbulent mixing plays a key role in the dynamics of marine ecosystems.

1.2 Governing equations

This section includes the governing equations along with a scaling analysis that describes our system. Starting from the conservation of mass:

$$\frac{\partial \rho}{\partial t} + \frac{\partial(\rho u)}{\partial x} + \frac{\partial(\rho v)}{\partial y} + \frac{\partial(\rho w)}{\partial z} = 0, \tag{1.2}$$

where $\boldsymbol{u} = (u, v, w)$ are the velocities in the (x, y, z) directions, respectively and ρ is the density of the fluid, the rate of change of density in a moving fluid is:

$$\frac{d\rho}{dt} = \frac{\partial \rho}{\partial t} + u\frac{\partial \rho}{\partial x} + v\frac{\partial \rho}{\partial y} + w\frac{\partial \rho}{\partial z}. \tag{1.3}$$

Combining equations (1.2) and (1.3) gives the continuity equation

$$\frac{1}{\rho}\frac{d\rho}{dt} + \left[\frac{\partial u}{\partial x} + \frac{\partial v}{\partial y} + \frac{\partial w}{\partial z}\right] = 0, \tag{1.4}$$

which in the case of an incompressible, Boussinesq fluid like the sea water, where density variations are considered small, and $[(1/\rho)(d\rho/dt)] = 0$, becomes:

$$\frac{\partial u}{\partial x} + \frac{\partial v}{\partial y} + \frac{\partial w}{\partial z} = 0. \tag{1.5}$$

Under the Boussinesq approximation, the conservation of mass becomes conservation of volume, which practically eliminates sound waves. Considering additionally that the phenomena examined here are relatively small the use of Cartesian coordinates and *f-plane* approximation, are appropriate. The equations relevant for this thesis are the momentum equations, assuming hydrostatic balance, the continuity equation and the buoyancy and density conservation equations, i.e.,

$$\begin{aligned}\frac{Du}{Dt} &= fv - \frac{1}{\rho_0}\frac{\partial p}{\partial x} \\ &+\frac{\partial}{\partial x}\left(2A_h\frac{\partial u}{\partial x}\right) + \frac{\partial}{\partial y}\left(A_h\left(\frac{\partial u}{\partial y}+\frac{\partial v}{\partial x}\right)\right) + \frac{\partial}{\partial z}\left(A_v\frac{\partial u}{\partial z}\right),\end{aligned} \tag{1.6}$$

$$\begin{aligned}\frac{Dv}{Dt} &= -fu - \frac{1}{\rho_0}\frac{\partial p}{\partial y} \\ &+\frac{\partial}{\partial y}\left(2A_h\frac{\partial v}{\partial y}\right) + \frac{\partial}{\partial x}\left(A_h\left(\frac{\partial u}{\partial y}+\frac{\partial v}{\partial x}\right)\right) + \frac{\partial}{\partial z}\left(A_v\frac{\partial v}{\partial z}\right),\end{aligned} \tag{1.7}$$

$$0 = -\frac{\partial p}{\partial z} - \rho g, \tag{1.8}$$

$$\nabla \cdot \boldsymbol{u} = 0, \tag{1.9}$$

$$\frac{D\rho}{Dt} = \frac{\partial}{\partial x}\left(K_h\frac{\partial \rho}{\partial x}\right) + \frac{\partial}{\partial y}\left(K_h\frac{\partial \rho}{\partial y}\right) + \frac{\partial}{\partial z}\left(K_\nu\frac{\partial \rho}{\partial z}\right), \tag{1.10}$$

$$\frac{Db}{Dt} = \frac{\partial}{\partial x}\left(K_h\frac{\partial b}{\partial x}\right) + \frac{\partial}{\partial y}\left(K_h\frac{\partial b}{\partial y}\right) + \frac{\partial}{\partial z}\left(K_\nu\frac{\partial b}{\partial z}\right). \tag{1.11}$$

In the above equations $f = 2\Omega\sin\phi$ is the Coriolis force, A_ν is the vertical eddy viscosity, A_h the horizontal eddy viscosity, K_h the horizontal eddy diffusivity, K_ν the vertical eddy diffusivity, and $D/Dt = \partial/\partial t + \boldsymbol{u}\cdot\nabla$ is the material derivative (Blumberg and Mellor, 1987). In order to account for the unresolved subgrid-scale processes in the

horizontal eddy viscosity, the Smagorinsky (1963) formulation is used, i.e.,

$$A_h = \mathrm{Pr}_t^h K_h = \Delta x \Delta y \sqrt{\left(\frac{\partial u}{\partial x}\right)^2 + \left(\frac{\partial v}{\partial y}\right)^2 + \frac{1}{2}\left(\frac{\partial u}{\partial y} + \frac{\partial v}{\partial x}\right)^2}, \tag{1.12}$$

where Pr_t^h (2 m^2 s^{-1}) is the horizontal Prandtl number and Δx, Δy are the local grid dimensions. Assuming a homogeneous, rapidly rotating and frictionless fluid equations (1.6) and (1.7) give the well-known geostrophic balance:

$$f u_g = -\frac{1}{\rho_0}\frac{\partial p}{\partial y}, \quad -f v_g = -\frac{1}{\rho_0}\frac{\partial p}{\partial x}. \tag{1.13}$$

Geostrophic balance is the essence of large scale fluid dynamics. It states that a balance can exist between the Coriolis force and the pressure gradient which results in a flow along the isobars, with the fluid moving with the high pressure on its right (for the Northern hemisphere). At large and meso scales, departures from this balance are generally considered small. Taking the vertical derivative of Eq. (1.13) and combine them with the hydrostatic balance [Eq. (1.8)] the thermal wind relation can be derived, i.e.,

$$f\frac{\partial u_g}{\partial z} = \frac{g}{\rho_0}\frac{\partial \rho}{\partial y}, \quad f\frac{\partial v_g}{\partial z} = -\frac{g}{\rho_0}\frac{\partial \rho}{\partial x}\,. \tag{1.14}$$

The thermal wind balance indicates that geostrophically balance fronts can be sustained away from the gravitational equilibrium if the lateral density gradients are associated with vertical velocity shears. This results in a baroclinic flow in the sense that velocity changes with depth (Cushman-Roisin and Beckers, 2011). In the case of a mixing event induced by a storm or differential cooling, where the upper ocean is left homogenized but lateral density gradients remain, an adjustment process will follow in the area of the front to flatten the nearly vertical isopycnals (Tandon and Garrett, 1994). In the absence of rotation, it would be expected the lighter water to split above the denser water until an equilibrium state was reached. However, under the influence of Coriolis, geostrophic adjustment takes place, leading the system to adjust towards a thermal wind balance, where the associated isopycnal slumping results to SML restratification and MLD shoaling. As will be discussed later, this geostrophically adjusted state has been seen to be further prone to baroclinic mixed layer instabilities that act to further increase the near-surface stratification (Boccaletti et al., 2007). The shoaling achieved through those instabilities is much larger than the one accomplished due to geostrophic adjustment alone (Mahadevan et al., 2010).

As mentioned earlier, mesoscale flows with horizontal length scales of $\sim \mathcal{O}$ (10-100km) are strongly influenced by Earth's rotation, which leads to Ro $\ll 1$, and by the small depth (H) to length (L) ratio, $\alpha = H/L$. The dynamics of submesoscale features are distinct from mesoscale flows in the sense that now Ro is $\mathcal{O}(1)$. Since the relative vorticity ($\zeta = v_x - u_y$) scales as $\zeta \sim U/L$ and Ro $= \zeta/f$, it follows that Ro $= U/fL$ and the characteristic submesoscale length is $L = U/f$. This length scale can also be expressed in terms of vertical stratification with the following analysis (Thomas et al., 2013a): Assuming thermal wind balance and that $b \equiv -g\rho/\rho_0$, Eq. (1.14) scales as $U \sim b_y H/f$, where b_y is the horizontal buoyancy gradient in y direction, and the length scale becomes $L = b_y H/f^2$. According to Garrett (1996) in the geostrophically adjusted state, the tilting of isopycnals leads to the development of a vertical stratification that can be expressed as, $b_z = b_y^2/f^2$ or by denoting $M^2 \equiv b_y$ in accordance to $N^2 \equiv b_z$ we have that $N^2 = M^4/f^2$. Substituting those relationships to the length scale above, results to $L = M^2 H/f^2$ or $L = NH/f$. Since N and H here concern the mixed layer, it follows that the horizontal length scale L of submesoscales is smaller than the Rossby radius of deformation (Thomas et al., 2013a). Moreover, by defining the bulk Richardson number as Ri $= N^2H^2/U^2$ and Ro $= U/fL$ or Ro $= U/NH$, we see that in this regime Ri $\sim$ Ro$^{-1/2}$ and consequently Ri is also $\mathcal{O}(1)$. Another implication of Ro $\sim$ Ri $\sim \mathcal{O}(1)$ is that the aspect ratio α scales as f/N and since for typical oceanic conditions $f/N \ll 1$ it follows that α is small ($\alpha \ll 1$). This implies that the hydrostatic approximation is valid in the submesoscale regime. In this thesis the balanced Richardson number (Ri$_b$) will be used, instead of the bulk (Ri) one, which based on the above formulations, is given by: Ri$_b = f^2N^2/M^4$.

1.3 Submesoscale processes

1.3.1 Frontogenesis and filamentogenesis

Hoskins (1982) defined fronts as those sites where the horizontal scale in the along-front direction is comparable to the radius of deformation (NH/f), whereas the across-front direction presents much smaller scales along with significant lateral buoyancy contrasts and velocity changes (Figure 1.4, left). Filaments, on the other hand, can be considered as double fronts (Figure 1.4, right). Preexistence of a strong horizontal density difference in combination with an ambient strain flow, that can be provided by mesoscale currents and eddies, creates favorable conditions for frontogenesis and filamentogenesis (Capet et al., 2008b; Gula et al., 2014).

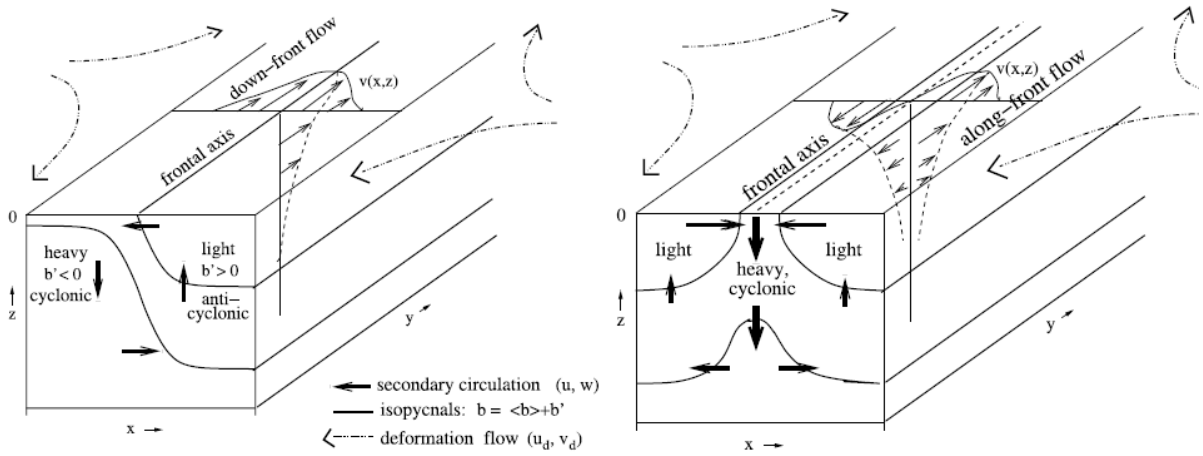

Figure 1.4: Surface frontogenesis (left) and cold filamentary intensification (right). The deformation flow and the lateral buoyancy gradients provide favorable conditions for frontogenesis and filamentogenesis. The flow is partly geostrophic in the along-front direction and ageostrophic in the (x,z)-plane. Downwelling ($w < 0$) and cyclonic vorticity $\zeta/f > 0$ dominates in the center of the filament (right). Figure adopted from McWilliams et al. (2009).

Frontogenesis (Hoskins, 1982) is instrumental in the dynamics of submesoscale processes. It may be understood as the rapid sharpening of lateral density contrasts under the presence of a horizontally confluent deformation flow, that disrupts the geostrophic balance and triggers a secondary ageostrophic circulation (Figure 1.4, left). The role of this ageostrophic circulation is to restore the geostrophic and hydrostatic balances by advectively tilting isopycnals toward the horizontal, i.e., by restratifying the flow. This is accomplished through surface convergence and downwelling on the dense side of the front and upwelling on the light side with the developed downward velocities being stronger than the upward ones. The mechanism of filamentogenesis (Gula et al., 2014) or filamentary intensification (McWilliams et al., 2009) for a cold filament is similar to frontogenesis, but in this case, a two-cell secondary circulation is generated in the cross-filament direction with even stronger surface convergence compared to frontogenesis, and a narrow downwelling channel at the center of the filament (Figure 1.4, right). Under the action of the ageostrophic circulation, which brings light fluid from the edges of the filament towards the center, isopycnals have a tendency to tilt towards the horizontal, and the flow restratifies. According to McWilliams et al. (2009), filamentogenesis for a warm filament is also possible, but the intensification rate is smaller due to surface divergence and associated upwelling in the middle of the filament that retards its narrowing.

Frontogenesis will be typically followed by frontal arrest (frontolysis) and decay, occurring commonly through the development of instabilities. Although the different instability types will be introduced in more detail in the following section, it is worth noting here that while Hoskins and Bretherton (1972) suggest that frontal decay will be accomplished through the development of Kelvin–Helmholtz instabilities, Thomas et al. (2013b) highlights the importance of symmetric instability that will ultimately lead further to a downscale cascade of energy. On the other hand, using high-resolution numerical simulations, Gula et al. (2014) showed that following filamentary arrest, shear instability develops and filaments fragment into a series of submesoscale vortices. Similar behavior was observed also in the high-resolution simulations of Capet et al. (2008a). Sullivan and McWilliams (2018) studied the lifecycle of a cold filament, under the action of different atmospheric forcing scenarios, by using large-eddy simulations. They showed that within less than a day, filamentogenesis is arrested mainly by amplification of turbulence through a small submesoscale horizontal shear instability that leads to a frontal decay and a forward cascade of energy, by further turbulent mixing. Hence, turbulence can act both frontogenetically, by intensifying the gradients through ageostrophic circulation, and frontolytically, by the enhancement of turbulent mixing. Regardless of the instability type, the result is typically a forward energy cascade, that ensures a pathway for the dissipation of mesoscale energy (Capet et al., 2008c). Restratification of the SML and reduction of vertical mixing is also to be expected, that might affect the marine biology in localized areas (Lévy et al., 2012).

1.3.2 Instabilities

Lateral buoyancy gradients in the shape of fronts and filaments are ubiquitous and span all scales of the flow. Frontogenesis and filamentogenesis occur constantly making fronts susceptible to different kinds of instabilities such as symmetric instability (Thomas et al., 2013b), ageostrophic anticyclonic baroclinic instability (Molemaker et al., 2005) and ageostrophic baroclinic Mixed Layer Instabilities (MLIs) (Boccaletti et al., 2007). Several studies (Boccaletti et al., 2007; Fox-Kemper et al., 2008; Mahadevan et al., 2010) have especially highlighted the ability of MLIs to restratify the SML by converting the horizontal density gradients to vertical stratification. As described by Boccaletti et al. (2007), during the passage of a storm increased winds homogenize the upper ocean. Yet the mixed layer keeps harboring weak lateral density gradients. Once the wind ceases, surface cooling generates gravitational overturning, that under the influence of planetary rotation, leads to geostrophic adjustment. The flow is then further susceptible to MLIs that continue to restratify the SML, by dynamically slump-

ing the vertical isopycnals towards the horizontal. MLIs are fast growing features that drive restratification by creating a vertical circulation in the plane normal to the front that flattens the isopycnal structure. The phenomenon is also called Mixed Layer Eddies (MLEs) when MLIs reach finite-amplitude and the disturbances roll up to eddies, with frontogenesis developing in their periphery (Boccaletti et al., 2007; McWilliams, 2016).

As noted by Fox-Kemper et al. (2008), while lateral fluxes are dominated by mesoscale eddies frontal features and MLIs seem to control the vertical fluxes and the upper-ocean stratification. The strength of MLIs depends on the available potential energy stored in fronts, which in turn depends on the horizontal buoyancy gradients and the depth of the SML. Fox-Kemper et al. (2008) proposed a parameterization for the restratification driven by MLIs that scales with the horizontal buoyancy gradient and the depth of the mixed layer, emphasizing the latter as a controlling factor for submesoscale instabilities. It has been suggested that this explains the clear seasonal cycle in submesoscale dynamics (Mensa et al., 2013; Brannigan et al., 2015) with increased activity during fall and winter conditions, when upper-ocean stratification is weak and the SML is deep. Overall, MLIs and frontogenesis have been proposed as the main submesoscale generation mechanisms in the SML (McWilliams, 2016). According to Callies et al. (2016), major differences between the mesoscale-driven surface frontogenesis and MLIs seems to be that the latter energizes the entire depth of the mixed layer and induces larger vertical velocities.

According to the theory (Hoskins, 1974), different kinds of instabilities can occur when the Ertel Potential Vorticity (EPV, q) and the Coriolis parameter take the opposite sign, i.e.,

$$fq = f(f\hat{\boldsymbol{k}} + \nabla \times \boldsymbol{u}) \cdot \nabla b < 0. \tag{1.15}$$

Since this thesis focuses on the Baltic Sea where $f > 0$, negative potential vorticity is considered to be equivalent to $fq < 0$. Under stable stratification ($N^2 > 0$) inertial or centrifugal instability arises when the absolute vorticity ($\zeta_{abs} = f + \zeta$) is negative and specifically when $f\zeta_{abs}N^2 < 0$. If $N^2 < 0$ the well-known gravitational instability or upright convection dominates the flow, which can be considered as the case of a top-heavy fluid. In this case, that might be developed by applying a spatially uniform buoyancy loss in an ocean at rest, convective plumes appear in which the injection of buoyancy vertically is accomplished through an overturning circulation that displaces

the fluid particles (Haine and Marshall, 1998). Another instability, commonly found at fronts is Symmetric Instability (SI). Following the analysis presented in Thomas et al. (2013b), for diagnosing SI it is useful to decompose Eq. (1.15) into two parts, one vertical and one horizontal, i.e.,

$$q = q_{vert} + q_{bc}, \tag{1.16}$$

$$q_{vert} = \zeta_{abs} N^2, \tag{1.17}$$

$$q_{bc} = \left(\frac{\partial u}{\partial z} - \frac{\partial w}{\partial x}\right)\frac{\partial b}{\partial y} + \left(\frac{\partial w}{\partial y} - \frac{\partial v}{\partial z}\right)\frac{\partial b}{\partial x}. \tag{1.18}$$

The vertical component [Eq. (1.17)] or baroclinicity contains the absolute vorticity and the stratification, whereas the horizontal component [Eq. (1.18)] is related to the horizontal terms of vorticity and the lateral buoyancy gradients. Assuming a geostrophically balanced flow $\boldsymbol{u}_g$ in thermal wind balance, Eq. (1.18) becomes:

$$q^g_{bc} = -f\left|\frac{\partial \boldsymbol{u}_g}{\partial z}\right|^2 = -\frac{1}{f}\left|\nabla_h b\right|^2 < 0. \tag{1.19}$$

This indicates that the baroclinic component of potential vorticity q^g_{bc} is responsible for lowering the EPV, leading to $fq < 0$. If additionally $N^2 < 0$ and $|fq^g_{bc}| > |fq_{vert}|$ and $fq_{vert} > 0$ then the instability is called SI. SI can be considered as a hybrid gravitational–centrifugal instability (Haine and Marshall, 1998). It is a shear instability that extracts kinetic energy from the geostrophic flow, leading to SML restratification and a downward transfer of energy to small scales (Thomas et al., 2013b). The downward cascade of energy is accomplished through a secondary Kelvin–Helmholtz instability that arises when SI reaches finite-amplitude (Taylor and Ferrari, 2009). The fluid motion in SI is along the slanting isopycnals (see Figure 2 in Taylor and Ferrari, 2011). The occurrence of hybrid modes, resulting from the combination of the above factors, is generally more often in nature (Haine and Marshall, 1998). SI has been recently observed at the Benguela upwelling system (Peng et al., 2020) and the Kuroshio Current (D'Asaro et al., 2011).

Overall, frontal features, initially in geostrophic and thermal wind balance, are unstable and tend to slump towards the horizontal. Fronts have been seen to become unstable first to SI, where an overturning circulation appears occurring along the isopycnals that slant to the vertical, while later on eddies and meanders might develop with the isopycnal slumping proceeding much faster as a result of baroclinic instabilities (Haine and Marshall, 1998; Taylor and Ferrari, 2011). Ultimately the result will be an increase

in upper-ocean stratification, while in the case of SI a transfer of energy towards the dissipation scales is also possible. The transition from symmetric to baroclinic instability was studied by Stamper and Taylor (2017) in an idealized setting. It is worth noting here that SI is a small scale process and thus large-eddy simulations are commonly used to adequately resolve it (Thomas et al., 2013b, 2016). Although the numerical model used in this work is not able to resolve scales associated with SI, in Chapter 3 it is shown that at least the criteria for SI, as presented above, are fulfilled in many submesoscale features that emerge close to a strong unstable frontal structure.

1.3.3 The role of atmospheric forcing

All the above processes are sensitive to atmospheric forcing, which can act either to enhance or suppress them (Figure 1.5). Surface cooling and "down-front" winds, i.e., winds that act on the direction of the frontal jet, have been shown to reinforce frontal features, and suppress submesoscale restratification (Thomas and Lee, 2005; Mahadevan et al., 2010). The former, by inducing convective mixing and the latter, by creating a wind-driven overturning cell (shown as ψ_w in Figure 1.5a) that acts in the opposite direction of the restratification cell (ψ_e in Figure 1.5a). On the contrary, a potential warming or "up-front" winds will accelerate the restratification, hence increasing the stability of the water column. Boccaletti et al. (2007) used theoretical considerations and idealized simulations to show not only that MLIs can induce restratification after storms, but also that they are fast enough to compete with mixing and restratify the upper ocean between sequential storm events. While Mahadevan et al. (2010) showed that "down-front" winds can arrest the restratification effect of MLIs, Whitt and Taylor (2017) applied high-resolution LES simulations and found that stratification can persist both after and during storm episodes, even under the action of "down-front" winds. On the other hand, Couvelard et al. (2015) focused on the effect of buoyancy loss and showed, by cooling an idealized turbulent jet, that during excessive cooling the deepening of the SML by convection can be counterbalanced by an upward submesoscale buoyancy flux, thus creating shallower mixed layers whereas, after the cooling event, MLIs support quick restratification. This restratification ability of submesoscales during the lifetime of storms is examined in Chapter 4. Here, the use of numerical simulations of the Baltic Sea provides a more realistic scenario compared to the above studies and will help to clarify whether submesoscales are able to maintain shallow mixed layers during storm events.

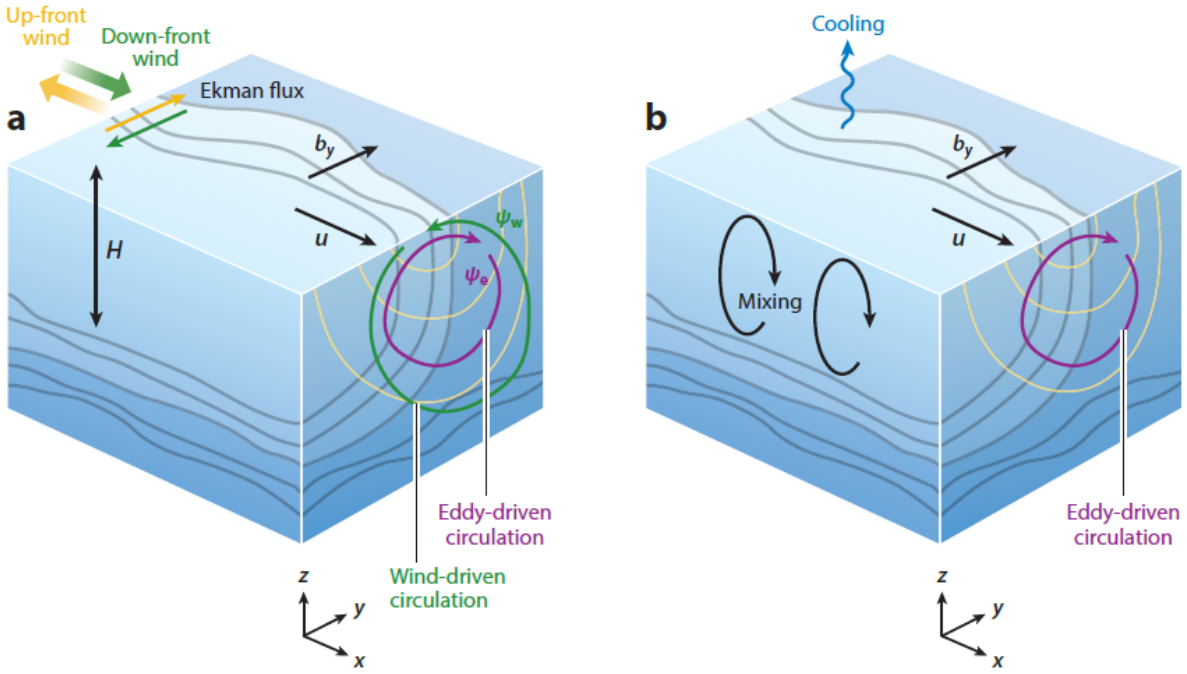

Figure 1.5: The role of atmospheric forcing. Mixed Layer Eddies (MLEs or MLIs see Section 1.3.2) generate a net overturning stream function ψ_e that tends to restratify the SML by slumping the nearly vertical isopycnals towards the horizontal. (a) The "down-front" wind (green thick arrow) reinforces the front by driving a cross-front Ekman transport that advects dense fluid over light fluid. The wind-driven overturning circulation, ψ_w (shown in green) opposes the restratification cell, ψ_e (shown in magenta) by MLEs. On the contrary, "up-front" winds will accelerate the restratification process (not shown). (b) Strong surface cooling can prevent the restratification of the SML by inducing a vertical buoyancy flux that opposes the restratification eddy flux. Here u denotes the along-front velocity, H is the MLD and b_y is the lateral buoyancy gradient. Figure adopted from Mahadevan (2016).

Surface cooling and "down-front" winds can also act to sustain SI, by inducing a destabilizing cross-front Ekman transport where denser fluid is being advected on top of lighter fluid, which lowers the potential vorticity of the surface layer (Thomas et al., 2013b). Taylor and Ferrari (2010) showed that when a strong front is subject to destabilizing atmospheric forcing a two-layer structure appears in the SML. An upper "convective layer" where turbulence is created by buoyancy loss and a lower layer where turbulence is induced by forced SI. High-resolution turbulence microstructure transects across a submesoscale filament, obtained recently in the Benguela upwelling system, confirmed the existence of those distinct turbulent layers (Peng et al., 2020). Enhanced turbulence in a symmetrically unstable front forced by "down-front" winds has also been observed in the Kuroshio Current (D'Asaro et al., 2011). Atmospheric forcing can thus initiate a forward energy cascade in frontal features through the development

of SI. Due to the role of atmospheric forcing on energizing those features, submesoscale flows present a strong seasonality, as opposed to mesoscales, with increased activity during wintertime when the mixed layer, which serves as an energy reservoir, is deep (Mensa et al., 2013; Brannigan et al., 2015).

1.4 Outline and aims

This thesis aims to improve our understanding of the impact of storms on submesoscale motions, from a realistic numerical perspective. Focusing mainly on MLD and mixing, this includes understanding the modifying effects of submesoscales on stratification and near-surface turbulence during a series of sequential storm events. Although this research focuses mainly on the dynamics of submesoscale processes, it provides also new insights into the potential significance of fronts in the Baltic Sea, that despite their ubiquity, their properties and dynamics are still largely unexplored in this brackish marine system. This thesis is organized as follows:

Chapter 2 introduces the study area (Eastern Gotland Basin) and the numerical ocean model that will be used throughout all subsequent chapters. A general description of the numerical model is given first, along with the diagnostic method that will be used in Chapter 5 for estimating the physical and numerical mixing. Then, the simulation setup is described. This is followed by the validation of the numerical model. Results from the high-resolution hindcast simulations are compared with vertical salinity and temperature profiles obtained from long-term monitoring stations, to analyze to what extend the numerical model is able to reproduce the vertical structure of the water column. To test whether the model resolution and setup are appropriate for this study, the simulations are subsequently compared with a high-resolution transect across a typical submesoscale filament, obtained during a field campaign. Finally, remote sensing data are used to validate the spatial distribution of sea surface temperature.

Chapter 3 provides a detailed description of the frontal area that occupies the entire Eastern Gotland Basin. First, the prevalent atmospheric conditions and the persistence of the main frontal pattern during autumn are investigated. Then, the structure and dynamics of submesoscale features are presented. Using several frontal quantities that are indicative of diagnosing the submesoscale flows, it is shown that a plethora of cold submesoscale filaments arises from the main frontal pattern, characterized by sharp lateral gradients, a clear deviation from geostrophy, strong surface convergence and associated downwelling. This is followed by evidence for the occurrence of gravita-

tional and symmetric instability along with a detailed analysis regarding the lifecycle of a dense submesoscale filament.

Chapter 4 focuses on the modulation of MLD by submesoscale motions. First, the ability of those flows to create highly heterogeneous MLD patterns by restratifying the upper-ocean is demonstrated. Using a feature extraction technique to distinguish between small-scale frontal regions and ambient waters, the temporal evolution of MLD is then investigated during the passage of a series of storm episodes. The main question that this chapter aims to address is whether submesoscales can maintain shallow MLDs during storms. The location of the main frontal pattern is also analyzed and its alignment with the isobaths is presented.

Chapter 5 focuses on frontal mixing. First, the simulated physical and numerical mixing is examined. Then, a binning technique is applied in order to evaluate the contribution of the different dynamical processes on the overall mixing and analyze the impact of storm events. Finally, a detailed analysis of the structure of turbulence inside submesoscale frontal regions is provided. The relatively unexplored relationship between processes that enhance turbulence in frontal areas (e.g., wind stress, atmospheric cooling, frontal instabilities, etc.) and SML restratification that has a tendency to suppress turbulence is investigated. The aim of this chapter is to shed light on the complex interplay between (i) wind-induced mixing that reduces surface-layer stratification, (ii) atmospheric buoyancy loss that induces unstable stratification and turbulent convection, and (iii) restratification by lateral processes that tends to counteract both effects. The main findings of this work and the overall implications are summarized and discussed in Chapter 6. Some future directions that this research could move in are also proposed and a general outlook based on the acquired knowledge is finally provided.

This thesis builds up upon the following manuscript submitted for publication on 16 May 2020:

- Chysagi et al. (2020): Chrysagi, E., Holtermann, P., Umlauf, L., Klingbeil, K. and Burchard, H. High-resolution simulations of submesoscale processes in the Baltic Sea: The role of storm events, J. Geophys. Res., submitted (reviews have not been received yet).

The submitted paper deals specifically with Sections 2, 3.1, 3.2, 3.3, 3.3.1, 4.1, 4.2, 5.2.

CHAPTER 2

Study area and methods

Using the easily accessible central basin of the Baltic Sea as a natural laboratory for the study of submesoscale motions, a field campaign (EMB169) was conducted during autumn 2017, to capture those structures. The data from the field campaign are used here to motivate and validate high-resolution (600 m) hindcast numerical simulations. This Chapter starts by introducing the main characteristics of the Eastern Gotland Basin, which is the focus of this study. Then, the basic features of the numerical ocean model and the setup configuration are presented. The model is subsequently validated against vertical salinity and temperature profiles, satellite images, and high-resolution microstructure transects collected during the campaign across submesoscale features.

2.1 Study area

The Baltic Sea is a semi-enclosed, non-tidal, shallow marginal sea connected to the North Sea through the Danish Straits. The bathymetry is quite complex, consisting of several straights and basins, interconnected through narrow sills. The salinity is generally low due to the positive freshwater budget, making the Baltic Sea a brackish marine system. The large amounts of freshwater provided by net precipitation and river runoff at the surface and the inflow of dense saline water in the bottom, originating from the North Sea, drive an estuarine circulation and create a strongly stratified system (Reissmann et al., 2009). Since tides are virtually absent, the Baltic Sea is mainly driven by wind stress and heat fluxes from the atmosphere along with other processes (e.g., bottom gravity currents, river runoff, boundary flows).

The Eastern Gotland Basin (red box in Figure 2.1a), which is the focus of this study, is the second deepest basin of the Baltic Proper with a maximum depth of approximately 250 m. The latitude of the study area is approximately 57°N, corresponding to a local inertial period of $T_f = 2\pi/f \approx 14.3$h, with $f = 1.2 \times 10^{-4}$ s^{-1} denoting the Coriolis parameter. Measurements collected during autumn 2017 at the Gotland Deep and specifically at the position of the monitoring station TF271 (marked as a red dot in Figure 2.1a), show that the basin is permanently stratified, with the lower salinity surface waters being separated from the denser deeper layers through a deep halocline centered around 70 m depth (black line in Figure 2.1b). The depth of the halocline, which varies throughout the year, is determined by advection, wind-induced, and convective mixing (Leppäranta and Myrberg, 2009). The vertical structure of temperature in the basin consists of a well-mixed layer near the surface, bounded below by a seasonal thermocline, that has been eroded down to 30 m depth during the period of the measurements, in fall (red line in Figure 2.1b). The water column exhibits a clear three-layer structure, that is more pronounced in the temperature profile. It consists of a warm surface layer above the sharp thermocline, a cold intermediate layer, and a deep salty layer below the halocline. The intermediate layer, which is located between the halocline and the thermocline, represents the remaining old "winter water" from the previous cooling period.

The strong stratification that characterizes the entire Baltic Sea, acts as a natural lid isolating the surface, oxygen rich waters from the bottom waters. In the absence of tides and due to insufficient diapycnal mixing (Holtermann et al., 2012), the main source of ventilation for the oxygen depleted bottom waters in the deep Gotland Basin, are the

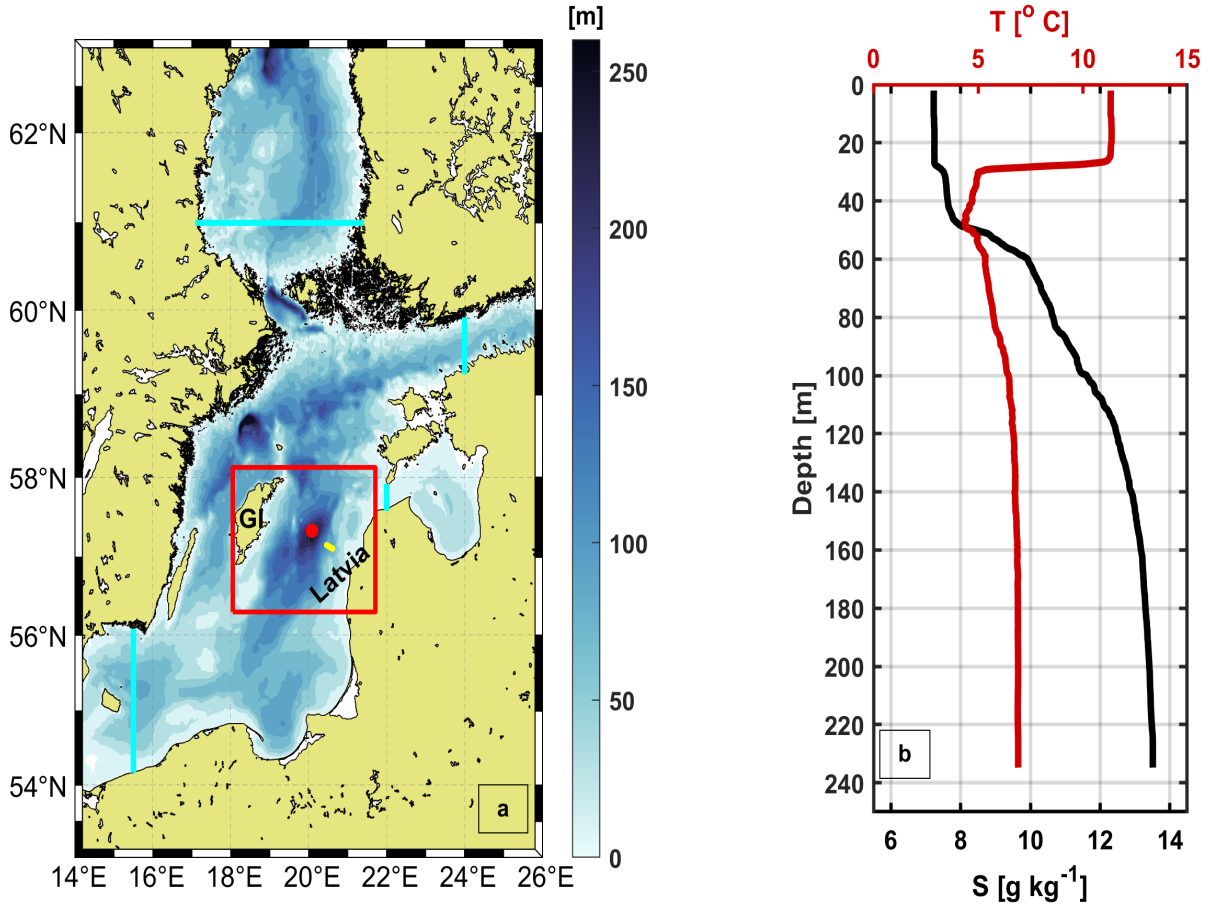

Figure 2.1: (a) Model domain and bathymetry. Cyan lines represent the open boundaries of the model. The red box indicates the study area (Eastern Gotland Basin) that is located between the island of Gotland (GI) and the Latvian coast. The position of the cross-filament transect, examined in Section 2.4.2, is illustrated by the yellow thick line extending from 20.60 to 20.46°W and approximately 57.1°N. The location of the monitoring station TF271 is shown as a red dot. (b) Observed temperature (red) and salinity (black) vertical profiles obtained during the EMB169 field campaign in the vicinity of station TF271, on 18 October 2017.

so-called Major Baltic Inflows (MBIs) (Reissmann et al., 2009). These are short-lived intrusion events that occur on decadal time scales and contribute to the renewal and oxygenation of the deep water, by transporting dense oxygenated water from the North Sea down to the deepest layers. Owing to the ecological importance of MBI events, most studies in the Eastern Gotland Basin have focused on the dynamics of the bottom and intermediate layers and not on surface processes. Thus, very few assessments have been undertaken regarding the surface dynamics in frontal regions, despite their known ubiquity in other seas and their crucial role in primary production and air-sea gas exchange.

Yet, akin to the open ocean, mesoscale fronts are omnipresent in the brackish Baltic Sea. As first noted by J. Pavelson (1988) and discussed by Leppäranta and Myrberg (2009) Baltic Sea fronts can be categorized based on their generation mechanism into (i) quasi-permanent salinity fronts, that are related to the general circulation in the basin or are located at the entrance of large gulfs, (ii) mesoscale salinity fronts, (iii) density compensating fronts that can present strong cross-front thermohaline gradients, and (iv) wind-induced upwelling fronts. It has been suggested that Baltic fronts are sites of abrupt current changes, interleavings, intrusions, strong current shears, and mixing (Kahru et al., 1984), while being simultaneously associated with increased primary productivity, elevated zooplankton abundance and cyanobacterial bloom formation (Kononen and Nômmann, 1992).

Here, numerical simulations are used in order to investigate a strong frontal structure that was captured from high-resolution satellite Sea Surface Temperature (SST) images, during autumn 2017 (see Figures 2.6a, 2.7a in Section 2.4.3). The focus is the Eastern Gotland Basin, where an east-west thermal gradient creates an energetic front that, as will be shown, provides favorable conditions for the formation of submesoscale features. This sharp frontal structure is located between the island of Gotland and the Latvian coast and has an almost latitudinal orientation. It is formed by the general cyclonic circulation in the basin, that advects warmer water from the southern parts of the Baltic Proper to the northeast and strengthens further during upwelling favorable winds, that bring cold water to the surface, close to the island of Gotland and transfer it to the east, through Ekman transport. Although the analysis of the submesoscale structures was chosen to coincide with the EMB169 field campaign (see Section 2.4.2), and hence it is restricted to an almost 20 days interval (17 October - 04 November), in Section 3.2 it is shown that this frontal feature is maintained and persists during the entire autumn. Moreover, additional satellite images (not shown) indicate that the

front exists also for different years and is sustained from approximately late summer to winter. A similar frontal structure with a chain of eddies was observed by Karimova (2012) in spring 2010, through the use of SAR images obtained by Envisat ASAR.

On longer timescales, the lateral density gradients in the Baltic Sea are maintained by the large-scale horizontal circulation which is cyclonic. Salt and heat are transported by the mean circulation and therefore, on the long-term mean, the water is warmer and saltier in the eastern side of the various sub-basins than in the western parts (Leppäranta and Myrberg, 2009). The general circulation is further enhanced by the existence of multiple cyclonic gyres. As in each of the main sub-basins of the Baltic Sea, the large-scale circulation in the Eastern Gotland Basin is characterized by a cyclonic recirculation cell, that on timescales larger than the inertial period, results from the interplay between earth's rotation and depth variations. Using numerical simulations Meier Markus (2007) confirmed not only the existence but also the persistence of this cyclonic circulation, which is located between the Gotland island and the coasts of Latvia and seems to control the annual mean water transport in the basin.

Moreover, during autumn and winter, the entire Baltic Sea is dominated by strong westerly winds, and the circulation is controlled mainly by Ekman dynamics and basin-wide bottom topography (Leppäranta and Myrberg, 2009). In the Eastern Gotland Basin, the prevalence of westerly winds creates an extended coastal upwelling zone at the island of Gotland. The cold upwelled water is advected to the south, southeast by Ekman transport and the general circulation, strengthening the lateral temperature differences between the island of Gotland and the coasts of Latvia.

2.2 The numerical model

The General Estuarine Transport Model (GETM; Burchard and Bolding, 2002) is an open source (see `http://www.getm.eu`), three-dimensional, numerical ocean model. GETM solves the hydrostatic primitive equations on a C-staggered Finite-Volume curvilinear grid, using the Boussinesq approximation, together with transport equations for temperature and salinity. It has been successfully applied in numerous hydrodynamic studies including coastal seas, estuaries, and lakes (e.g., Burchard et al., 2009, 2011; Becherer and Umlauf, 2011; Gräwe et al., 2015), along with studies investigating the dynamics of the Baltic Sea (Holtermann et al., 2014; Burchard et al., 2018; Gräwe et al., 2019). GETM was furthermore used by Vortmeyer-Kley et al. (2019) in order to study

the dynamics of eddies in the surface layer and to create an eddy-census of the central Baltic Sea.

In contrast to the more common z-coordinate or σ-coordinate (terrain-following) models, GETM incorporates also a new adaptive technique for the vertical mesh (Burchard and Beckers, 2004; Hofmeister et al., 2010). Several studies (Hofmeister et al., 2011; Gräwe et al., 2015) have shown that the use of a non-uniform vertical adaptive grid, that follows the evolution of stratification and shear, reduces substantially the pressure gradient errors and the numerical mixing caused by discretization errors of the advection schemes. Additionally, by comparing realistic simulations of the Baltic Sea and the North Sea using adaptive and sigma coordinates, Gräwe et al. (2015) showed that the use of adaptive coordinates can result in a stronger and more realistic mesoscale field. According to Burchard and Beckers (2004), in the case of a front where the vertical gradients are large due to the outcropping of the isopycnals, this adaptation method allows us to better represent frontal structures in the oceanic surface mixed layer. Hence, in the present study, this zooming technique allows us to resolve the outcropping of the isopycnals and the base of the mixed layer with high resolution, providing a more faithful representation of the sharp buoyancy gradients associated with submesoscale structures.

The horizontal viscosity is parameterised here according to Smagorinsky (1963) using a Smagorinsky constant of 0.6, combined with a turbulent Prandtl number of two for tracers. The vertical mixing is parameterized using an algebraic second-moment turbulence closure model (Canuto et al., 2001), extended by two prognostic equations for the turbulent kinetic energy, k, and the dissipation rate ε. The k-ε model, which is discussed in detail in Umlauf and Burchard (2005), is implemented through the use of the General Ocean Turbulence Model (GOTM). GOTM is a one-dimensional water column model that provides state-of-the-art turbulence closure schemes and stability functions. By assuming a steady-state gradient Richardson number of $R_f^{\mathrm{st}} = 0.25$, a value representative for homogeneous shear layers in equilibrium (Burchard and Baumert, 1995), the damping effect of stable stratification on turbulence is quantified. This is equivalent to a flux Richardson number for equilibrium of $R_f^{\mathrm{st}} = 0.18$ (Umlauf et al., 2003), which can be further reformulated as a mixing coefficient for equilibrium conditions such as, $\Gamma^{\mathrm{st}} = R_f^{\mathrm{st}}/(1 - R_f^{\mathrm{st}}) = 0.22$ (Umlauf et al., 2003; Burchard and Hetland, 2010). This value is slightly larger than the canonical value of $\Gamma = 0.2$ (Osborn, 1980). In order to account for the lack of mixing in the interior stratified region due to e.g. internal wave breaking, a background turbulent kinetic energy level of

$k_{\min} = 10^{-7}$ m^{2}s^{-2} is applied in the k-ε model, together with a clipping of the turbulent length scale as proposed by Galperin et al. (1988). The parameterization feeds back into the turbulent diffusivity as a non-constant contribution depending on stratification.

The temporal discretization of GETM is based on an explicit mode splitting technique, using a two-way volume-conserving coupling of the barotropic and baroclinic modes (Burchard and Bolding, 2002). For minimizing the numerical smoothing of gradients, the advection of momentum and tracers is discretized, using a second-order Total Variation Diminishing (TVD) scheme with a Superbee limiter, in a directional split mode (Pietrzak, 1998). Superbee is a well-known anti-dissipative scheme, i.e, increases the energy in the system, and its performance has been tested and compared with other advection schemes in experiments of lateral shear and baroclinic instabilities (Mohammadi-Aragh et al., 2015).

Another important feature in GETM is the inclusion of a diagnostic method for separating and estimating the physical and numerical mixing of tracers (Burchard and Rennau, 2008). In this diagnostic method, which will be used in Section 5.1 for evaluating the frontal mixing, the numerical mixing $\chi^{num}(s)$ of any tracer s, caused by the discretization errors of the selected advection scheme ($\mathcal{A}$), is calculated locally and treated as the decay rate between the advected square of the tracer and the square of the advected tracer, ie.,

$$\chi^{num}(s) = \frac{\mathcal{A}\{s^2\} - (\mathcal{A}\{s\})^2}{\Delta t}, \tag{2.1}$$

where Δt is the internal timestep (Gräwe et al., 2015). The physical mixing on the other hand, that is considered as the decay rate of tracer variance (Burchard and Rennau, 2008), is:

$$\chi^{phy}(s) = 2K_h\left(\frac{\partial s}{\partial x}\right)^2 + 2K_h\left(\frac{\partial s}{\partial y}\right)^2 + 2K_\nu\left(\frac{\partial s}{\partial z}\right)^2, \tag{2.2}$$

where K_h and K_ν are the horizontal and vertical diffusivities respectively and χ^{phy} the physical mixing. Both mixing quantities χ^{num} and χ^{phy} can be directly compared (Burchard and Rennau, 2008; Gräwe et al., 2015).

In order to extend the results of Burchard and Rennau (2008), Klingbeil et al. (2014) defined the fluxes of the second moment in terms of fluxes of the first moment instead of having an independent discretization of the prognostic equation for the sec-

ond moment, resulting in a more solid approach with better runtime performance. A 3D dissipation analysis for quantifying the physically and numerically induced loss of kinetic energy was also proposed by Klingbeil et al. (2014) and has been implemented in GETM.

2.3 Simulation setup

The simulation setup used in this thesis is similar to the one used by Holtermann et al. (2014) for investigating the different dynamical mechanisms that contribute to the deep water mixing rates in the central Baltic Sea. Here, the focus is on the upper ocean, where submesoscale processes are more pronounced and the aim is to explore the dynamics and mixing inside frontal and filamentary features during the lifetime of storms. The numerical domain covers the entire central Baltic Sea and specifically the area from 15.5° to 24.0°W, and from 54.2° to 60.6°N which is known as the Baltic Proper (Figure 2.1a). However, the analysis is narrowed down to the Eastern Gotland Basin (red box in Figure 2.1a) where, as will be shown in the following, during autumn 2017 a strong lateral temperature front created favorable conditions for the formation of cold elongated submesoscale filaments.

The horizontal resolution of the numerical model is anisotropic and varies in the zonal direction from 501 to 597 m. The meridional resolution is between 597 and 598 m, resulting in total to 929x1200 horizontal grid points. According to Fennel et al. (1991), the first baroclinic Rossby radius in the Baltic Proper, during the period of interest, is approximately 5 km, hence processes with analogous scales are fully resolved by the model. To fully resolve the submesoscales horizontal grid resolutions below the Rossby radius of deformation (usually below 1 km) are required (Thomas et al., 2013a; McWilliams, 2016). Several studies (e.g., Capet et al., 2008a,b; Brannigan et al., 2015) have shown that as the resolution is made finer, a dynamical transition occurs since the sharpening of lateral density gradients gives rise to higher complexity structures and spontaneous emergence of submesoscale features. The horizontal resolution applied here is expected to be sufficient for allowing the development of submesoscale fronts and filaments. The vertical resolution consists of 100 flexible adaptive layers with a minimum surface layer thickness of 0.3 m and a maximum of 1 m for the first 50 levels, in order to better resolve the dynamics of the surface boundary layer. The barotropic time step is 3 s with a baroclinic splitting factor of 15, to guarantee numerical stability. The numerical domain and the model bathymetry are shown in Figure 2.1a.

The initial conditions were obtained by continuing the numerical simulations from Holtermann et al. (2014) for the years 2007 until 2016. The resulting temperature and salinity profiles from the model output were subsequently combined with Conductivity-Temperature-Depth (CTD) profiles of the central Baltic Sea, available from the HELCOM database (http://www.helcom.fi). This was done in order to start the simulations from the most realistic state, especially in the deeper waters. The combination was performed by applying a distance-weighted algorithm, based on a Gaussian function with a standard deviation of 10 nm. This means that directly at a profile position the initial data is the CTD data, in 10 nm distance 61% is taken from the cast and the rest from the model output. The simulation was then run freely without further nudging from 1 February 2016 to 31 December 2017. The open boundary conditions (shown with cyan lines in Figure 2.1a) were obtained from the 1 nm Baltic Sea model of Gräwe et al. (2019), using a one-way nesting approach. Thus, hourly output of temperature, salinity, sea surface elevation, and depth-averaged velocities from the 1 nm model, are provided as input for the inner, higher resolution domain.

The atmospheric forcing was provided by the operational model of the National German Weather Service (DWD) with a spatial resolution of 7 km and a temporal resolution of 3 h. Several studies (e.g., Meier Markus, 2007; Holtermann et al., 2014; Placke et al., 2018) have shown that models tend to underestimate the depth of the halocline and thermocline, in the offshore region of the Eastern Gotland Basin. In the high-resolution simulations applied here this underestimation can be attributed to the lack of wind gustiness since, during autumn, both the halocline and the thermocline positions are controlled mainly by wind-induced mixing. Therefore, the wind speed was increased by 15% to account for the lack of gustiness that results from the low temporal resolution of the atmospheric model. This choice was further justified by time-limited meteorological measurements obtained during the field campaign, clearly showing that the DWD data slightly underestimate the variations of the wind field in the Eastern Gotland Basin, during the period of interest (Figure 2.2). The atmospheric variables provided by the DWD model were further used for calculating the air-sea fluxes of momentum, heat, and freshwater, based on the bulk formulas of Kondo (1975). Freshwater input from rivers entering the domain was modeled using monthly river discharge data of the rivers Emån, Mälaren, Neman, Vistula, and Pregolya.

The simulation was run from 1 January 2016 to 31 December 2017. Yet, the study period is restricted from 17 October until 4 November 2017, with the intent to simulate dynamical features observed during the EMB169 research campaign, that took place at

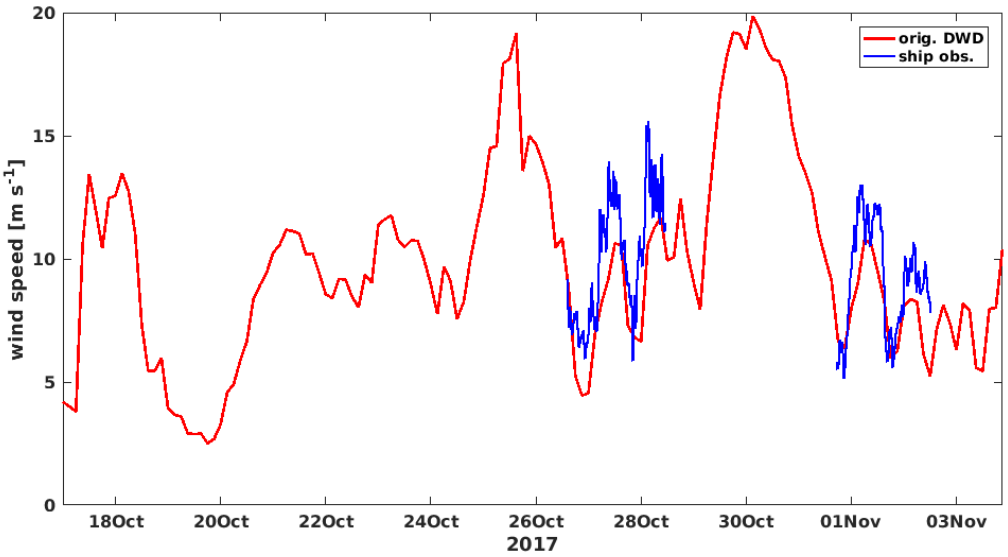

Figure 2.2: Comparison between the original wind speed data from the operational model of the German Weather Service (DWD, red line) and the ship-based measurements collected during the field campaign (blue line), close to the monitoring station TF271. The comparison shows the underestimation of the wind field by the DWD atmospheric dataset. The observations present large data gaps due to two storm episodes (25 October and 30 October) that passed over the field site during the period of the field campaign.

the Eastern Gotland Basin, during that period. For those 18 days, all the 2D and full 3D fields were saved as hourly averages. For the rest of the simulation period, only surface fields and vertical profiles at specific locations that correspond to monitoring stations were stored and were used for validating the model. The simulations presented here were performed using computational resources from the North-German Supercomputing Alliance (HLRN) system.

2.4 Model validation

Although the scope of this study is not to achieve a one to one comparison between observations and model simulations, the model validation is still considered crucial for obtaining some degree of realism. To illustrate the good agreement between simulations and observations, of the most relevant features for this study, satellite images were used along with measurements obtained during the EMB169 field campaign as well as long-term hydrographic data from the HELCOM standard monitoring program. The hydrographic data, presented in the following section, concerns the monitoring station TF271 which is located at the Gotland Deep (marked with a red dot in Figure 2.1a). The EMB169 cruise is analyzed in detail in Section 2.4.2.

2.4.1 Monitoring data

To analyze to what extend the numerical model is able to reproduce the vertical structure of the water column, vertical profiles of temperature and salinity were used. For the years 2016 and 2017, several profiles are available from the monitoring station TF271 (Figure 2.1a). Here, three representative profiles from three different months were chosen and the comparison with the simulated ones shows that the model is in good agreement with the observations both for temperature and for salinity (Figure 2.3a,b,c). The timeseries of near-surface temperature, extending from February 2016 until the end of 2017, indicate that the simulated temperatures compare favorably with the observed ones throughout the entire period (Figure 2.3d). Small deviations are found in surface salinity especially during late summer (Figure 2.3e). Nevertheless, these deviations are not expected to affect the results presented here, since the horizontal density differences in most of the submesoscale structures that emerge in the study area, are mainly controlled by the temperature contrasts and not by salinity. The role of salinity and temperature on setting the lateral density gradients is analyzed in more detail in Section 3.3.1.

For the period of interest (17 October - 4 November), several measurements were obtained during the field campaign at the same position as the monitoring station and in the surrounding area. An exemplary comparison of an individual simulated and observed vertical profile for temperature and salinity is shown in Figure 2.4. The profile was obtained near station TF271 during the first day of the campaign, on 18 October 2017. The model is seen to provide an excellent representation of the vertical struc-

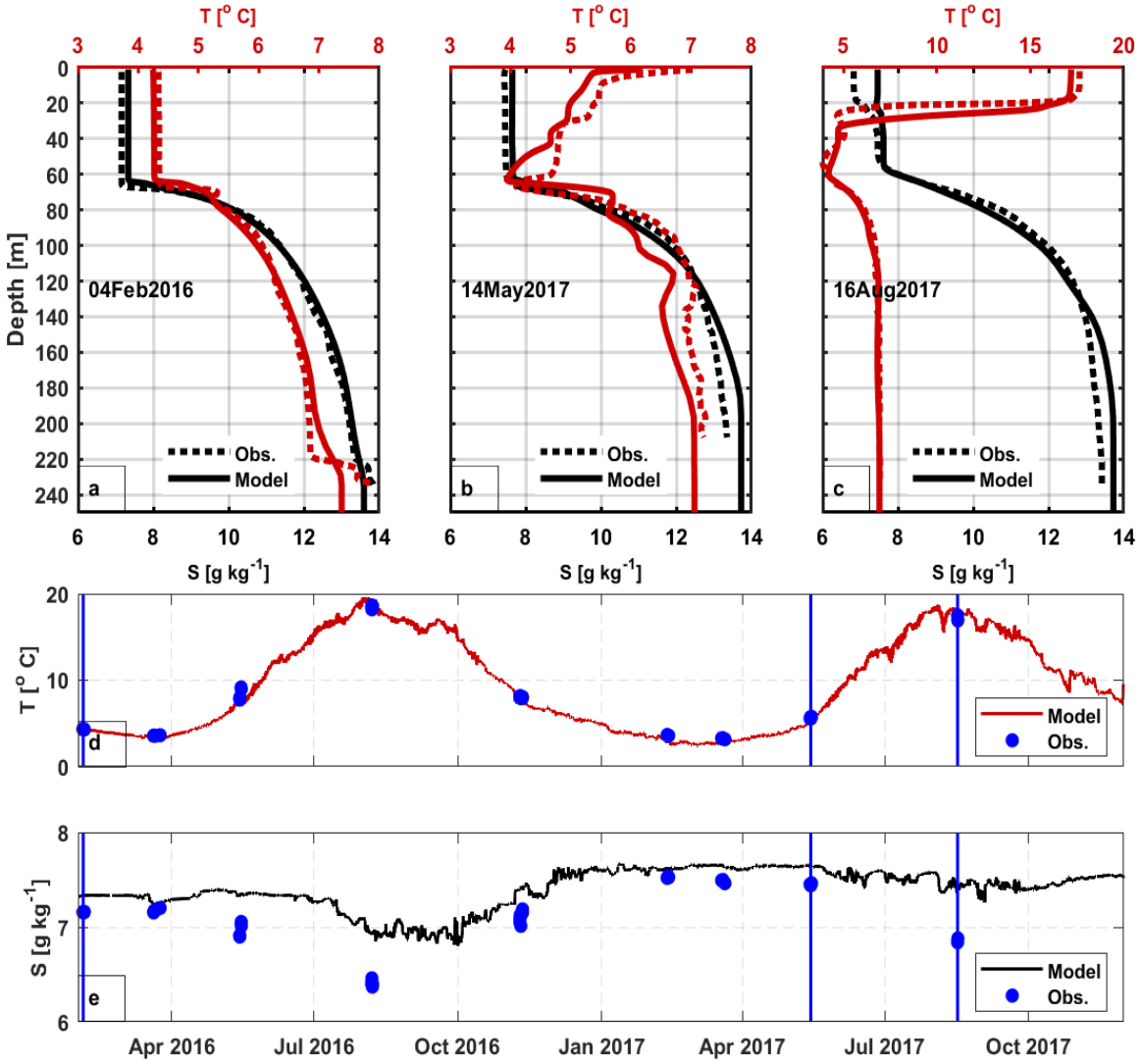

Figure 2.3: Model validation using the data from the monitoring station TF271. Observed (dashed line) and simulated (continuous line) temperature (red) and salinity (black) profiles on (a) 04 February 2016, (b) 14 May 2017, and (c) 16 August 2017. Vertically averaged (2-20m) timeseries of temperature (d) and salinity (e) with observations marked as blue dots. The vertical blue lines correspond to the profiles shown in (a)-(c). The location of the station TF271 is marked as red dot in Figure 2.1a

ture of the water column. The low salinity that characterizes the basin and the depth of the halocline, which is located around 70 m during the period of the measurements, is perfectly reproduced by the numerical model. In the deeper layers, where salinity increases due to salt water inflows, the simulated salinity is slightly larger than the observed one. The temperature profile presents minor differences at the surface, with the modeled temperatures being slightly colder than the observed ones (Figure 2.4). Nevertheless, in Section 2.4.3 it is shown that in other positions, such as close to the

coast of Latvia, the simulated surface temperatures are to some degree warmer than the observations. Figure 2.4 clearly shows that the depth of the surface layer, which is important for the submesoscale processes, is predicted with good accuracy.

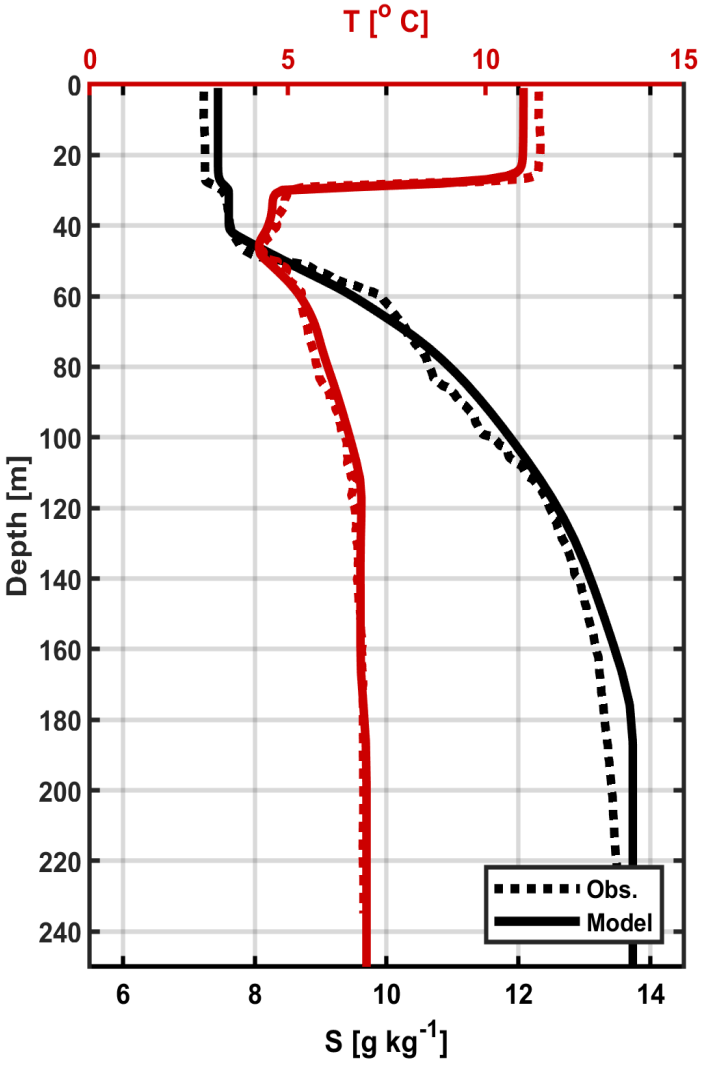

Figure 2.4: Comparison between the observed (dashed line) and simulated (continuous line) temperature (red) and salinity (black) profiles. The measured profiles were obtained during the EMB169 field campaign in the vicinity of the monitoring station TF271, on 18 October 2017.

2.4.2 Ship-based measurements

Several hydrographic and turbulence measurements were obtained during a four-week (16 October - 04 November, cruise EMB169) field campaign, with R/V Elisabeth Mann Borgese. The EMB169 campaign, which was conducted in the Eastern Gotland Basin, was dedicated to measuring submesoscale structures in the SML. Using a free-falling turbulence microstructure profiler, several high-resolution turbulence and CTD transects were collected across multiple frontal and filamentary features. One of those transects is illustrated in Figure 2.5a. The measurements were interrupted two times due to intense storms (see Section 3.1) that passed over the field site, whereas the resulting cloud cover prohibited the repeated detection of the strongest frontal structures from satellite images.

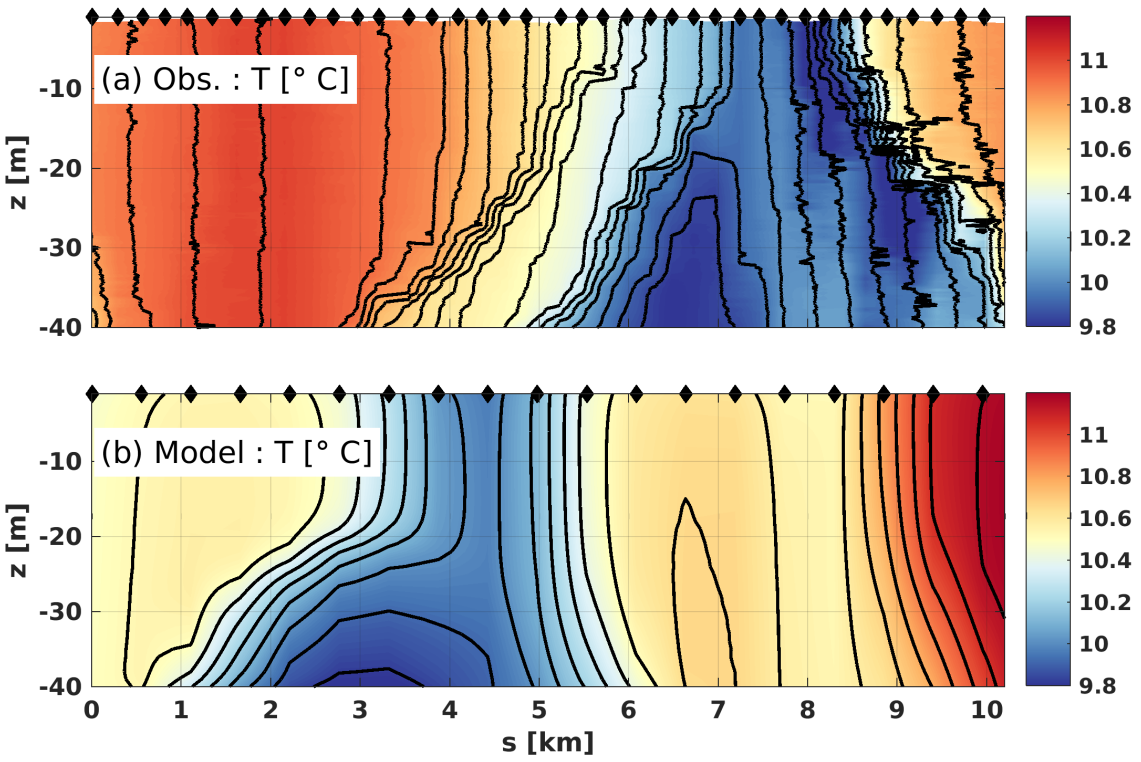

Figure 2.5: Vertical structure of a cold submesoscale filament. (a) High-resolution microstructure temperature data collected during the EMB169 field campaign, on 31 October 2017 from 20:00 until 24:00 UTC. (b) Temperature snapshot from the numerical model for 31 October 2017 20:00 UTC. Black contours denote isopycnals with a spacing of 0.01 kg m^{-3}. The x-axis indicates the total length of the transect with s=0 km corresponding to the beginning of the transect. Black markers show the positions of individual microstructure casts in (a), and indicate the model resolution in (b). The position of the transect on the map is shown in Figure 2.1a with a yellow line.

Here, a representative high-resolution temperature transect is presented that was collected across a relatively weak, yet fully-shaped cold filament (Figure 2.5a). The location of this approximately 10 km long transect, obtained on 31 October 2017 from 20:00 until 24:00 UTC, is indicated in Figure 2.1 with a yellow line. The orientation of the transect is from west to east, extending from 20.60 to 20.46°W and approximately 57.1°N. The high horizontal resolution of the transect which is approximately 300 m allows us to efficiently resolve submesoscale structures in the surface layer (see black markers in Figure 2.5a).

Model results are compared with this high-resolution transect as can been seen in Figure 2.5. The position, length, orientation, and timing of this transect were exactly identical in the simulations and observations, respectively. In view of this, and the non-linearity of the problem, the agreement between the model and the observations is striking. Beyond a small offset of the center of the simulated filament relative to the observations, all main characteristics of the filament (width, depth, density contrast, etc.) are well reproduced by the numerical model (Figure 2.5b). This provides support to the assumption that the model resolution and setup are appropriate for this analysis. The acquired observational data from the EMB169 campaign revealed that the Eastern Gotland Basin is rich in submesoscale features. These data served not only for validating the model but also as a motivation for the current research.

2.4.3 Satellite data

To validate the spatial distribution of the simulated Sea Surface Temperature (SST) high-resolution satellite images are required. Figure 2.6 shows an exemplary comparison between the model results and high-resolution satellite data obtained from the Visible and Infrared Imager/Radiometer Suite (VIIRS) just before the field campaign, on 10 October. It is evident that the model (Figure 2.6b) is able to reproduce the observed surface temperature structure (Figure 2.6a) in the entire basin. The simulated east-west temperature differences found between the coast of Latvia and the island of Gotland are in good agreement with the remote sensing data (Figure 2.6a). The cold water observed at the northern tip of Gotland island is due to the beginning of an upwelling episode, more pronounced in the next days (see Figure 2.7).

During the field campaign, high-resolution satellite data from VIIRS or MODIS (MOderate Resolution Imaging Spectroradiometer) were rare due to the excessive cloud

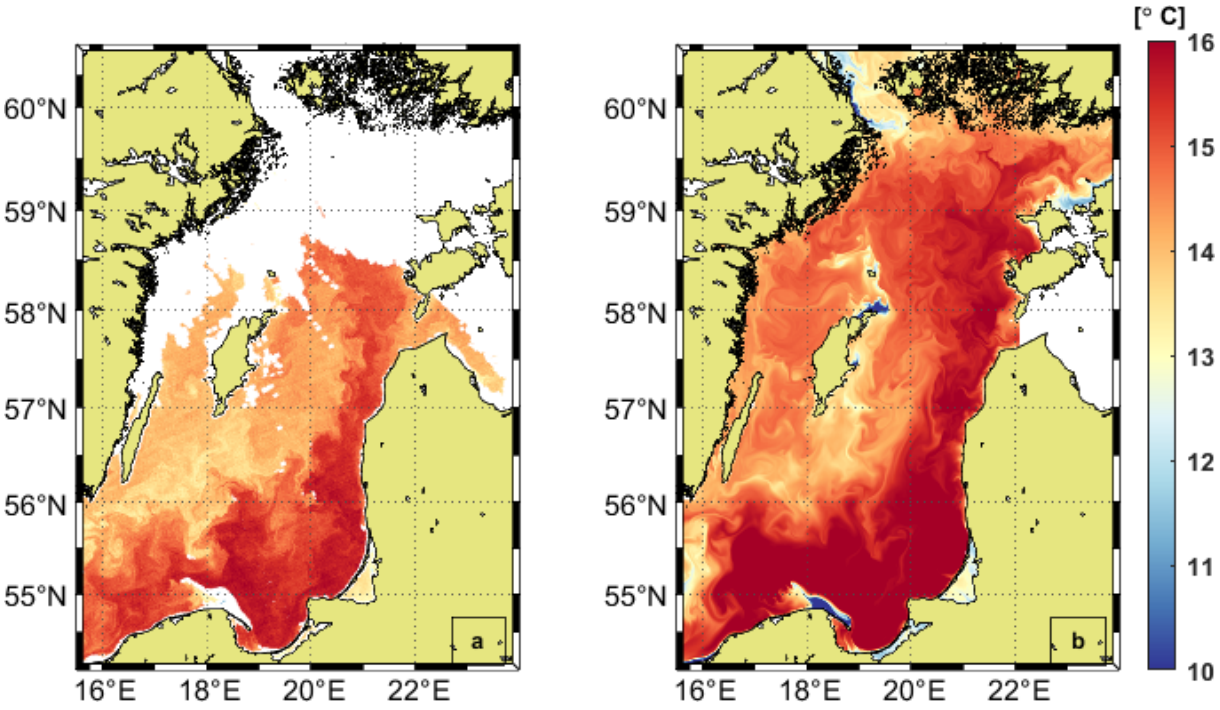

Figure 2.6: Model validation one week before the field campaign. SST snapshot of the Baltic Proper from (a) remote sensing data (Visible and Infrared Imager/Radiometer Suite) and (b) from the numerical model. Both panels are for 10 October 2017. White areas in (a) indicate missing data due to cloud cover. The resolution of the satellite data is ∼1 km, whereas for the numerical model a horizontal grid size of around 600 m is used.

cover. The only available satellite image is from 19 October, yet with significant data gaps. Thus, a daily average SST satellite product from BSH agency (German Federal Maritime and Hydrographic Agency) is used in order to show the model performance for the period of interest (Figure 2.7). This product combines several daily satellite overflights and a manual cloud detection scheme to reduce the number of data gaps. The numerical model is generally able to realistically reproduce key features of the surface dynamics of the Baltic Proper (Figure 2.7b). On 18 October, intense westerly-southwesterly winds created an extended coastal upwelling zone with lower temperatures around the island of Gotland that were still evident on 19 October. Both the position and the strength of the upwelling area are well reproduced by the simulations. As explained earlier, close to the coast of Latvia waters with higher temperatures are advected from the southwest to the northeast. The numerical model slightly overestimates the warmer temperatures in the eastern part of the Gotland Basin, close to the coast of Latvia. Regarding the rest of the numerical domain, there are no significant differences between the simulated and observed SST.

In the Eastern Gotland Basin, the most striking feature is the strong lateral temperature gradient of more than 3 K found between the island of Gotland and the coast of Latvia (Figure 2.7). It is evident that both the strength and the position of this front are well captured by the model. The correct representation of the lateral temperature contrasts by the numerical model is essential since the density differences in this frontal structure and in the associated submesoscale features are found to be controlled by the temperature (see Section 3.3.1). This frontal structure that as will be shown in Section 3.2, constitutes a persistent feature during autumn 2017, has also been observed in other years. Specifically, Karimova (2012) presented a similar frontal structure with a chain of eddies through the use of SAR images for 2010. Clearly, the frontal region hosts a variety of elongated cold filaments. The main characteristics of these dynamical features are well represented by the model, and filament gradients are even more pronounced in the fine resolution simulation (∼600 m) compared to the slightly coarser resolution satellite product (∼1 km). Fronts and filaments with weaker temperature contrasts can be identified in the entire Baltic Proper, whereas relatively high temperature gradients appear in the northern part of the basin, in the entrance of the Gulf of Bothnia.

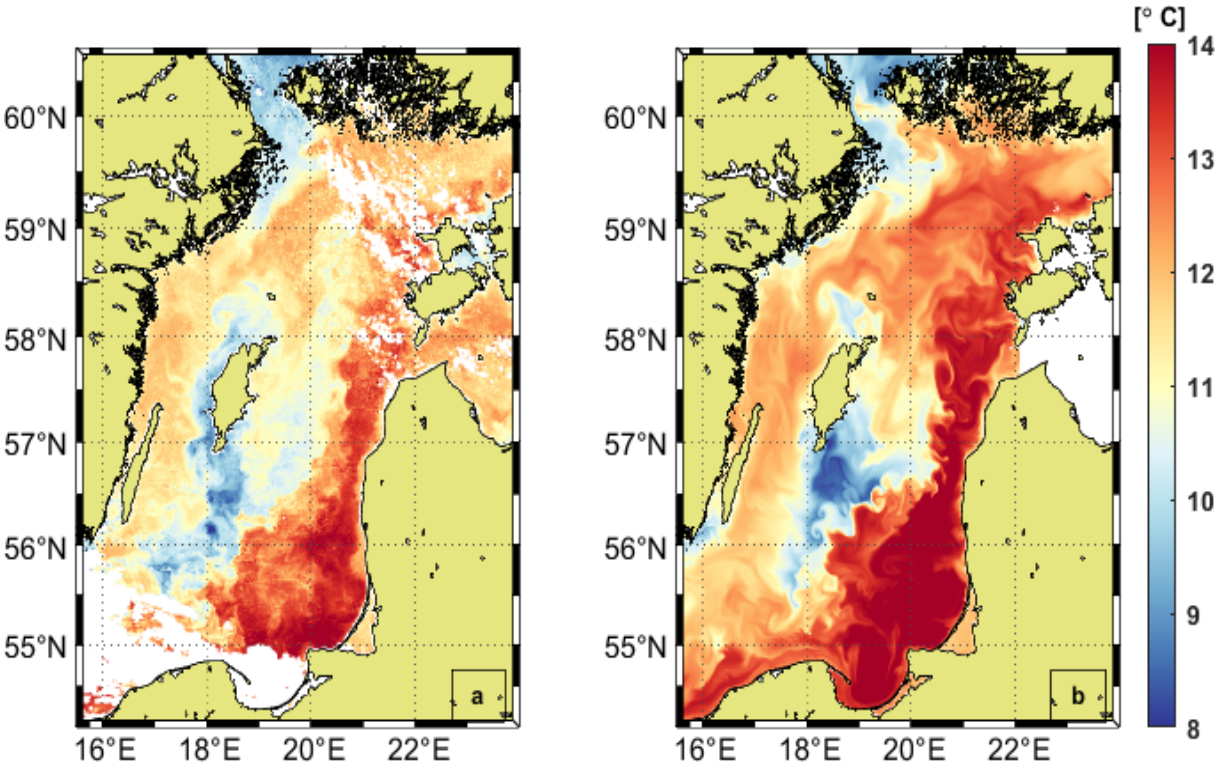

Figure 2.7: Model validation using satellite data. Daily averaged SST field in the Baltic Proper from (a) observations (satellite product from the Federal Maritime and Hydrographic Agency of Germany (BSH)) and (b) from the numerical model. Both panels are for 19 October 2017. White areas in (a) indicate missing data due to cloud cover.

CHAPTER 3

The frontal region

Motivated by satellite images of the Baltic Sea that show cyanobacteria blooms forming in regions of strong submesoscale filaments and fronts (Figure 1.3), this chapter aims to explore the ubiquity of those structures and provide a first picture of the submesoscale dynamics, in this semi-enclosed basin where submesoscale studies are still largely lacking. By performing realistic high-resolution numerical simulations of the Eastern Gotland Basin a strong thermal frontal structure, acting as a hotspot of submesoscale activity has been revealed. Although this front seems to be maintained throughout the autumn period, it has not been reported previously. This chapter starts by exploring the prevalent atmospheric conditions because surface wind stress and buoyancy forcing have the ability to either enhance or suppress submesoscale activity. Next, the generation mechanism and the persistence of the front during the fall season are presented. Subsequently, the structure and the dynamics of the frontal area are investigated with a particular focus on the submesoscale regime. Several frontal quantities that are indicative of diagnosing submesoscale flows are presented along with the preponderance of submesoscales close to the unstable frontal pattern. This is followed by an analysis of gravitational and symmetric instability, with the former found to dominate the entire basin apart from the frontal area. Finally, the lifecycle of a typical cold submesoscale filament, from its generation until its destruction, is described.

3.1 Atmospheric conditions

The evolution of atmospheric forcing is crucial for frontal dynamics as wind and buoyancy fluxes have the ability to energize or suppress the frontal processes. Specifically, the surface buoyancy flux (B_0, Figure 3.1b), that includes both the air-heat and freshwater fluxes, can act either to stabilize or destabilize the water column by changing the surface density, that is,

$$B_0 = -g\alpha Q_0 / (\rho C_p) + g\beta (E - P) S_0, \tag{3.1}$$

where g denotes the gravitational acceleration, α the effective thermal expansion coefficient, Q_0 the net heat flux entering the ocean, ρ the density of seawater, C_p the specific heat capacity (here, taken to be $C_p = 4000$ J kg^{-1} K^{-1}), β the effective haline contraction coefficient, E the evaporation, P the precipitation and S_0 the surface salinity (Cronin and Sprintall, 2001). Note here that Eq. (3.1) is written in such a way that positive B_0 values denote loss of buoyancy from the ocean to the atmosphere, describing destabilizing conditions. For the calculations, the COARE 3.0 bulk algorithm of Fairall et al. (2003) is used.

The spatially averaged wind speed and direction over the Eastern Gotland Basin, along with the buoyancy flux (B_0) and air temperature (T_{air}), for the period of interest, is illustrated in Figure 3.1. During this period three main wind events occurred in the basin. The first storm passed over the field site around 18 October 2017 with south-southwesterly winds, the second around 25 October with pronounced southerly winds, and the third one on 30 October with northerly winds (Figure 3.1a). During those storm events, the wind speed and direction were spatially uniform over the entire basin. A maximum value of 20 m s^{-1} was observed during the last storm, whereas the lowest wind speeds were found on 19 October, with values as small as $\sim$ 2 m s^{-1}. The upwelling favorable winds during the first two wind episodes created an extended coastal upwelling zone near the island of Gotland. Based on the frontal orientation the winds can be further characterized as approximately "down-front" during the first two storms, and "up-front" during the third one (Thomas and Lee, 2005). In Chapter 4 it is shown that the upwelling favorable winds during the first wind event and the extremely calm weather conditions that followed, contributed to the strong restratification of the surface mixed layer by submesoscale features.

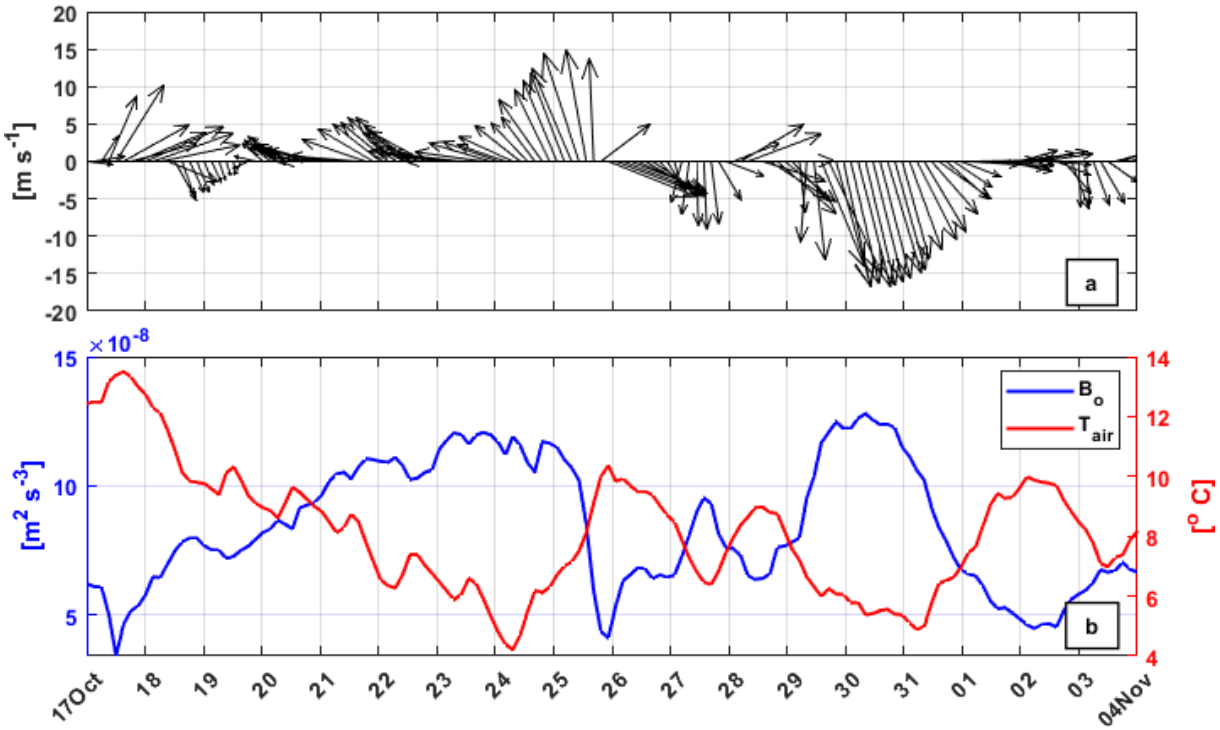

Figure 3.1: Evolution of spatially averaged atmospheric forcing over the Eastern Gotland Basin during October/November2017. (a) Wind speed and direction, (b) upward surface buoyancy flux (B_0, blue) and air temperature (T_{air}, red).

The surface buoyancy flux B_0 was positive throughout the period of interest, implying an upward destabilizing flux, resulting in buoyancy loss (Figure 3.1b). As expected, the buoyancy loss increases (blue line in Figure 3.1b) when the air temperature decreases (red line in Figure 3.1b). The freshwater flux (not shown) had generally a small contribution to B_0 except for the second storm, on 25 October. During that day, the strong winds were followed by intense precipitation. This intense precipitation in combination with the increased T_{air} led to a sharp decrease in B_0.

The strong buoyancy loss observed throughout the entire period and the intense winds clearly have a tendency to reduce near-surface stratification and keep the surface layer well mixed. Yet, in Chapter 4, it is shown that after each of the sequential storm events a fast and intense surface-layer restratification is observed in the vicinity of the frontal structures. Figure 3.1 shows that potential excessive heating, after the passage of the storms, is not the reason for the observed restratification. Conversely, it will be shown that the bulk of the restratification occurs in patches, inside strong submesoscale features that emerge after each sequential storm event. These submesoscale patterns can compensate for the destratifying effect of the atmospheric forcing by restratifying the

upper ocean, through a dynamical slumping of the lateral density gradients, yielding regions with shallow mixed layers. This can have implications for ocean models where currently, only the restratification due to surface heating is included, whereas the impact of submesoscales on the evolution of SML (unless resolved) is completely ignored (Fox-Kemper et al., 2008).

3.2 Frontal pattern during autumn

A strong east-west thermal front was identified in the Eastern Gotland Basin by the numerical simulations, during autumn 2017; available satellite images (not shown) confirm its existence for different years. The mean SST conditions in the basin along with the surface circulation and the density field are shown in Figure 3.2a. The frontal structure which persisted throughout October - November 2017, can be seen both from the spatial differences in temperature and the density structure (Figure 3.2a). The elongated front occupies the entire Eastern Gotland Basin with an approximately southwest-northeast orientation.

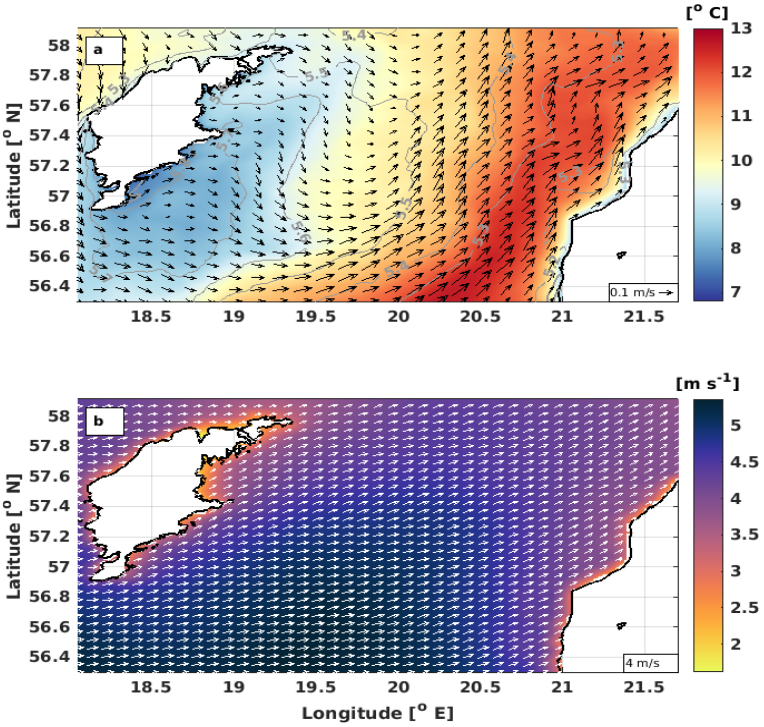

Figure 3.2: (a) Mean Sea Surface Temperature (SST) and surface circulation in the Eastern Gotland Basin for the period 01 October - 31 November 2017. Gray contours denote isopycnals with a 0.1 kg m^{-3} interval. (b) Mean wind speed and direction (arrows) for the same period.

The prevalence of westerly-southwesterly winds over the basin (Figure 3.2b), create an intense coastal upwelling zone south and southeast of the island of Gotland (Figure 3.2a). The cold $\sim 8^{\circ}$C upwelled water is carried to the eastern part of the basin, through Ekman transport, where it meets the relatively warm waters, near the coast of Latvia. This warmer water is characterized by mean surface temperatures of approximately 12°C. It is transported mainly from the southwestern part of the Baltic Proper to the northeast by a mean surface meandering current that is part of the general cyclonic circulation in the basin. The cold upwelled water on the west and the warm water on the east create a strong and persistent lateral thermal gradient.

Another process that might also contribute to the intensification of the frontal structure is the differential cooling between the well-mixed, down to the bottom, shallow waters in the east, and the more stratified deep waters in the west. In the northern part of the basin, relatively cold water with a northern Baltic Proper origin and temperatures around 10°C might enhance further the temperature differences in this area. The aforementioned processes contributed not only to the development of a strong lateral front but also to its maintenance, from late summer to early winter. This frontal pattern is the most remarkable structure in the surface layer of the study area and acts as a hotspot of submesoscale genesis (see Section 3.3).

3.3 Submesoscale features

3.3.1 Main characteristics

Several frontal quantities that are indicative of the submesoscale regime are presented as snapshots in Figure 3.3, after the passage of the first storm. As previously mentioned, the first storm passed over the field site on 18 October (Figure 3.1) with upwelling favorable winds that strengthened the lateral temperature differences, whereas the pronounced calm weather conditions that followed, contributed to the further enhancement of submesoscale features. Various submesoscale fronts and filaments at different stages of development can be identified from the near-surface temperature structure (Figure 3.3a). Both warm and cold filaments appear in the domain, with the latter being more abundant than the former. It has been suggested that the reason for the dominance of cold filaments is the direction of the secondary circulation. According to McWilliams et al. (2009) in the case of a cold filament subject to filamentogenesis a two-celled secondary circulation is generated in the cross filament direction with intense surface convergence and a narrow downwelling channel in the middle of the

filament, whereas in warm filaments surface divergence and upward velocities dominate, decreasing the rate of filamentary narrowing.

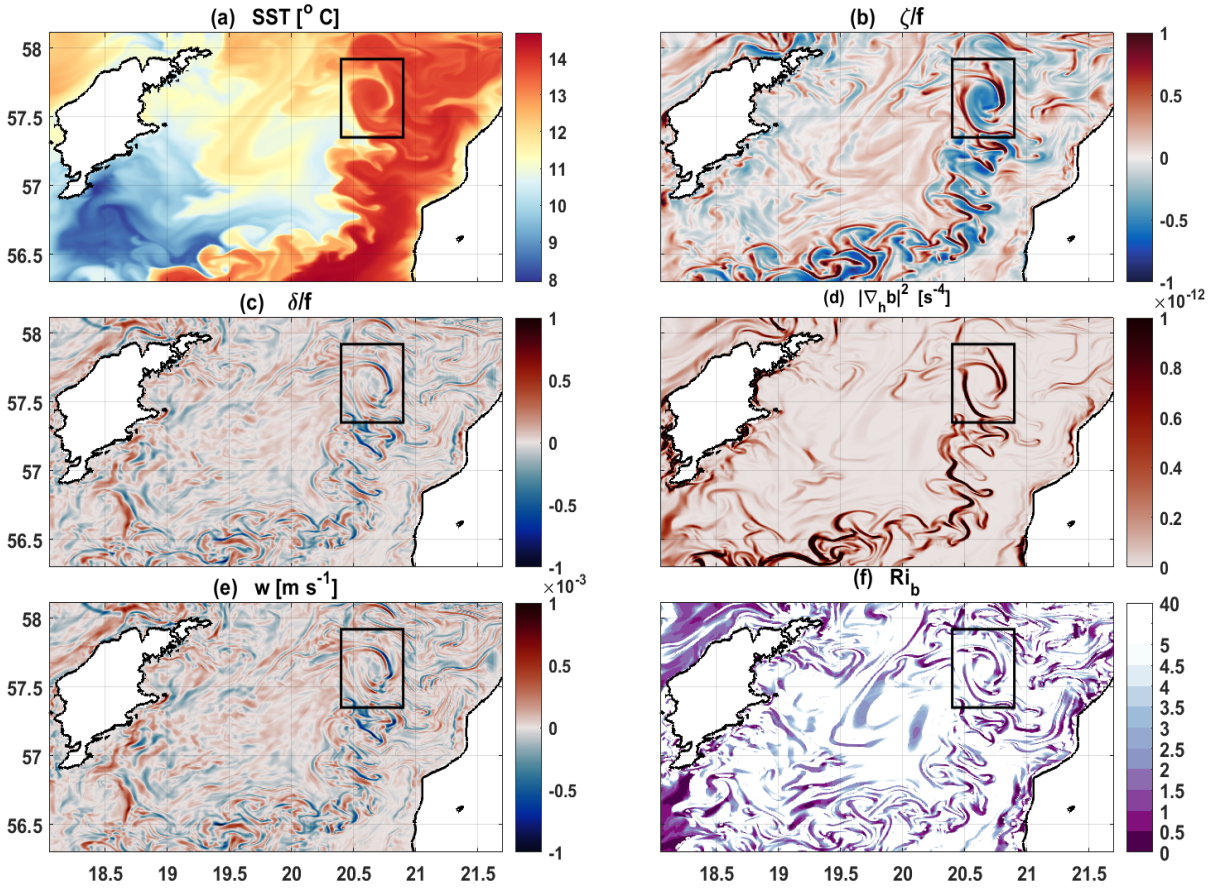

Figure 3.3: Frontal quantities representative of the submesoscale nature of the flow. (a) SST, (b) Rossby number (relative vorticity ζ normalized by the Coriolis frequency f). Positive values denote cyclonic vorticity. (c) Divergence normalized by f. Negative values denote convergence. (d) Frontal sharpness defined here as $|\nabla_h b|^2$, (e) vertical velocity at 10 m depth and (f) balanced Richardson number. The black rectangles indicate the position of the filament shown in Figure 3.8. All patterns are near-surface instantaneous fields for 12:00 UTC 19 October 2017.

The cold filaments are quite strong in some cases with more than 2°K temperature difference relative to the surrounding area (Figure 3.3a). As expected, the stronger filaments i.e., the ones with the highest lateral buoyancy gradients (Figure 3.3d), are concentrated at the flanks of the main frontal pattern as frontal regions are auxiliary in energizing submesoscale features. These strong frontal and filamentary features exhibit $\mathcal{O}(1)$ Ro and Ri_b dynamics [see Eq. (1.1)], thus belong to the submesoscale regime (Figures 3.3b,f). The Ri_b is mainly positive in this snapshot as it is associated with daytime with calm weather conditions. Both positive and negative Ro appear in the study

site, with the former being confined to thinner areas, inside the filaments. The prevalence of positive Ro values inside the filaments (Figure 3.3b) indicates that cyclonic vorticity ($\zeta = v_x - u_y$) dominates over anticyclonic vorticity, suggesting that those structures are strongly skewed. Actually several studies (e.g., Hoskins and Bretherton, 1972; Rudnick, 2001) have pointed out that when Ro $= \mathcal{O}(1)$ the upper ocean is characterized by a strong positive asymmetry for ζ that decays at the base of the mixed layer. A detailed analysis regarding this asymmetry is provided in Section 5.1.2, where the skewness in ζ is shown in relation to temperature mixing.

The vertical velocities are particularly intense inside the filaments, reaching up to $\mathcal{O}(10^{-3})$ m s^{-1} in some cases (Figure 3.3e). Downward velocities are higher than the upward ones with the narrow downwelling occurring in the middle of the cold filaments. As mentioned in Chapter 1, strong surface convergence and intense ageostrophic secondary circulation are expected to arise during frontogenesis to restore the geostrophic balance (Hoskins, 1982; McWilliams et al., 2009). This is consistent with the observation that the vertical velocity and the horizontal divergence, i.e.,

$$\delta = u_x + v_y \ , \tag{3.2}$$

exhibit the same alternate patterns of positive and negative values (Gula et al., 2014), with the downwelling corresponding to convergence lines and vice versa (Figures 3.3c,e). Despite the complexity of the different processes involved, there is a remarkable correspondence between the various quantities presented in Figure 3.3, which is indicative of the submesoscale nature of the flow. Extreme gradients in buoyancy, a clear deviation from geostrophy, significant surface convergence, and associated downwelling are the signature of the $\mathcal{O}(1)$ Ro and Ri$_b$ features, as shown in previous submesoscale studies (Mahadevan and Tandon, 2006; Capet et al., 2008b; Gula et al., 2014).

The main frontal pattern, which occupies the entire eastern part of the Gotland Basin, has an almost meridional orientation parallel to the isobaths (see gray contours in Figure 3.4a). The frontal alignment with the isobaths is presented in detail in Section 4.3 using probability maps of the stronger lateral buoyancy gradients. In this brackish basin, the surface salinity (Figure 3.4b) is generally low with maximum values in this snapshot detected at the south-eastern part of the Gotland island where coastal upwelling, induced by the preceding south-westerly winds, resulted in a transport of more saline waters from the deeper layers to the ocean surface. The minimum salinities detected along the coast of Latvia seem to originate from the Vistula river (located

further to the south at the Gdańsk basin; the freshwater discharge veers initially to the North and gets subsequently transported to the Eastern Gotland Basin) while other tributaries north of Gdańsk basin can also contribute to the observed low salinities.

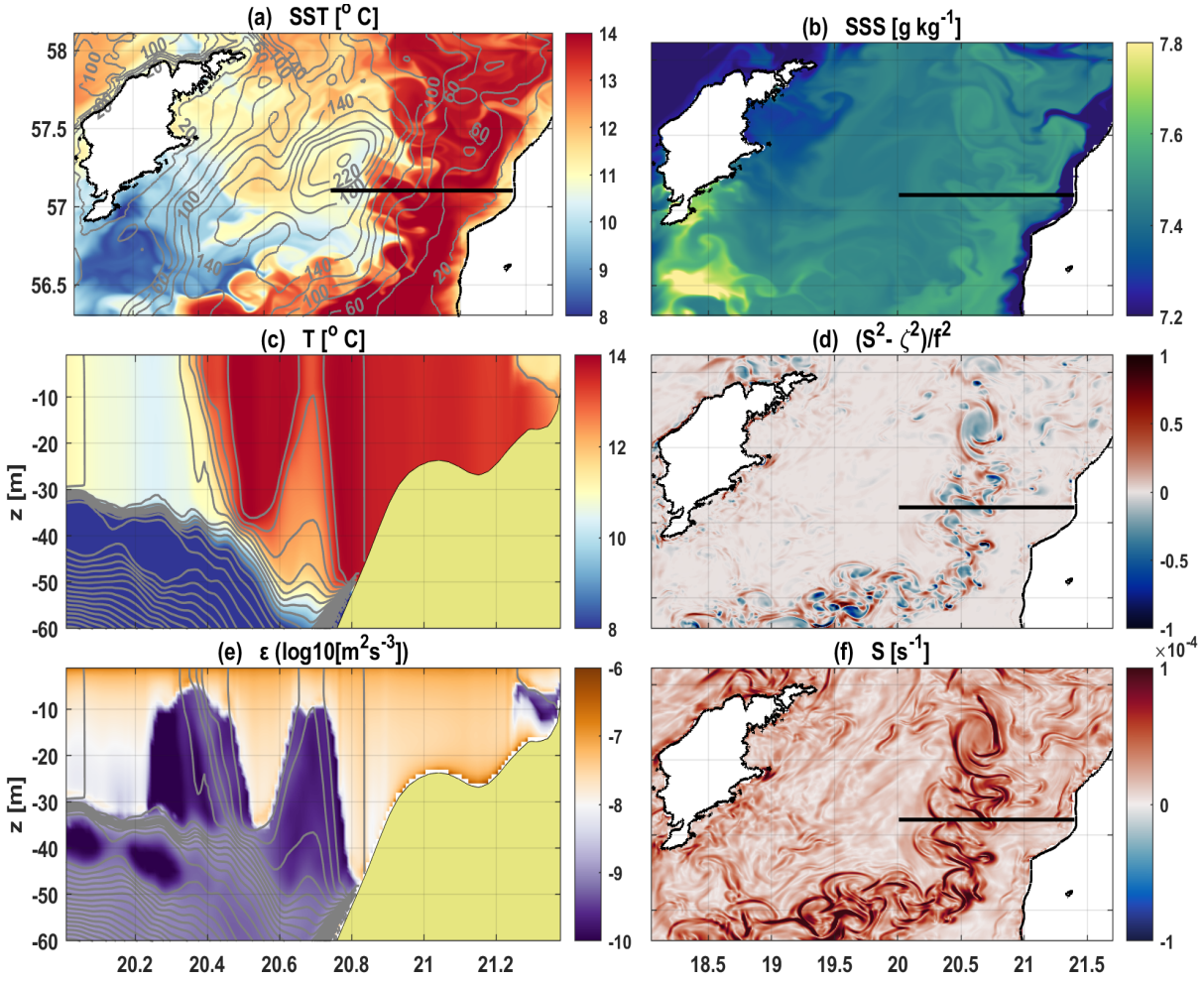

Figure 3.4: (a) Sea Surface Temperature (SST). The black line indicates the location of the transect displayed in panels (c),(d). (b) Sea Surface Salinity (SSS), (c) vertical temperature structure across a cold front (∼20.4°E) and an elongated filament (∼20.7°E). (d) Okubo-Weiss parameter normalized by f^2, (e) dissipation rate (ε) and (f) horizontal strain rate (S). Gray contours in (a) denote the bathymetry in the area, whereas in (c) and (e) indicate the vertical structure of the isopycnals. All patterns are snapshots for 22:00 UTC 19 October 2017, a few hours after Figure 3.3.

In order to quantify the relative contribution of salinity and temperature differences in setting the horizontal density gradients in the submesoscale features, the density ratio $R = \alpha\Delta T/\beta\Delta S$ was calculated (Rudnick and Ferrari, 1999). Here, α and β denote the thermal and haline expansion coefficients respectively. The R across any typical submesoscale filament, arising from the main frontal pattern, was significantly larger

than one (almost five in some cases), suggesting that the lateral density gradients are mostly controlled by the temperature differences. This further indicates that the use of satellite SST images for detecting those features and validating the numerical model is quite an appropriate method. Unlike the main frontal pattern, intense lateral salinity gradients can be identified along the coasts of Latvia where a thin salinity front appears, presenting a density ratio R of ∼0.7.

The existence of strong lateral buoyancy contrasts in combination with a straining environment creates favorable conditions for frontogenesis and filamentogenesis (Gula et al., 2014). The horizontal strain rate (S):

$$\mathrm{S} = \sqrt{(u_x - v_y)^2 + (v_x + u_y)^2}\ , \tag{3.3}$$

that acts in general either frontogenetically, by intensifying the lateral density gradients or frontolytically by weakening the gradients, presents a local maxima along the main frontal structure (Figure 3.4f). It should be noted that a decomposition as presented in Gula et al. (2014) has not been applied, and thus, Figure 3.4f illustrates the total strain. This includes both the strain induced by the geostrophic flow and the strain induced by the ageostrophic secondary flow, as a response to the ambient straining environment.

It is evident that the spatial distribution of the flow consists of straight continuous filaments but also of curved or fragmented ones (Figure 3.4a). The different shapes suggest different stages of lifecycle, associated either with frontal intensification or frontal breakup (Capet et al., 2008b; Gula et al., 2014). The thin elongated filaments with lateral widths of $\mathcal{O}(1)$ km are quite ephemeral, sustained for periods between a few hours to a few days before they typically break up into smaller vortices. This will be shown in detail in Section 3.3.3. The signature of vortical and filamentary structures can be seen more clearly by using the Okubo-Weiss (OW) parameter (Okubo, 1970), i.e.,

$$\mathrm{OW} = S^2 - \zeta^2\ , \tag{3.4}$$

that includes both the strain rate (S) and the relative vorticity ($\zeta = v_x - u_y$), therefore typically used to distinguish between strain dominated and vorticity dominated flows. Several studies (e.g., Klein and Lapeyre, 2009; Mensa et al., 2013) have shown that since strain generally tends to stretch and expand, it is relevant to more hyperbolical structures like filaments whereas vorticity, that tends to fold, concerns more

elliptical features like vortices. In agreement with those studies, the OW parameter is positive inside the strong filaments, some of which are still in the intensification stage (Figure 3.4d). Outside of the filaments, however, negative OW values dominate. This indicates (1) pre-existent vortices that act to stretch and deform the filaments, like the small vortex seen around 20.7°E and 57.6°N (see also Figure 3.9), (2) smaller vortical structures that arise during filamentary fragmentation (more visible in the last panel of Figure 3.9). Although in mesoscale flows, regions of high strain rates are distinct from those with large relative vorticities, Figure 3.4d clearly shows that this is not the case in the submesoscale regime, where high strain and high vorticity areas coincide due to large shear (Mahadevan and Tandon, 2006). A detailed analysis regarding the dynamics of eddies in the surface layer of the central Baltic Sea is provided by Vortmeyer-Kley et al. (2019) who found, by using different eddy detection methods, that the Baltic Sea is dominated mainly by cyclonic eddies.

The vertical temperature structure across a representative submesoscale front and a cold filament are shown in Figure 3.4c. Sharp temperature gradients at the edges of both submesoscale patterns result in a local outcropping of the isopycnals from around 40-60 m depth (gray contours in Figure 3.4c,e). Both features emerge close to the topographic slope. Enhanced dissipation rates (ε) are observed in the surface layer where relatively intense winds increase the upper-ocean turbulence (Figure 3.4e). Yet, in the frontal and the filamentary structure, lower ε values are found. This suggests that submesoscale patterns have the ability to shelter the surrounding regions from becoming turbulent. The "shadowing" of the mixed layer turbulence by fronts was also observed during the EMB169 field campaign through high-resolution turbulence microstructure measurements obtained from a glider (Carpenter et al., 2020).

3.3.2 Gravitational and symmetric instability

Different kinds of instabilities can occur in the oceanic SML, as described in Chapter 1, with Symmetric Instability (SI) being one of them. SI commonly found in the presence of horizontal density gradients is a shear instability, that has drawn much attention due to its role on the forward cascade of geostrophic energy. Here, results are presented showing initially the well-known gravitational instability (or upright convection) and then evidence pointing to symmetric instability (slantwise convection).

During the study period excessive cooling and/or strong winds (see Figure 3.1 for atmospheric conditions) dominated over the entire Eastern Gotland Basin, resulting in

an unstable SML stratification, commonly found during wintertime conditions (Reissmann et al., 2009). The response of the upper-ocean stratification to different atmospheric forcing conditions is shown in Figures 3.5a,b and 3.6a using the buoyancy frequency squared, N^2. On 19 October (Figure 3.5a), calm wind conditions during night and relatively strong cooling resulted in winter and/or nighttime convection whereas on 30 October (Figure 3.5b), during the peak of the last storm, wind-induced mixing and excessive cooling modified further the upper-ocean stratification. Gravitational overturning, associated with denser fluid overlying lighter fluid, seems to dominate in these cases, leading to a preponderance of negative N^2 values. Interestingly, however, stable stratification ($N^2 > 0$) is observed in localized patches, particularly evident in Figure 3.5a. Those patches are seen to coincide with the sharp horizontal thermal gradients, present in Figure 3.4a. This provides the first evidence of the ability of submesoscale features to compensate for the destratifying effect of atmospheric forcing and increase the vertical stratification of the upper-ocean, both during (Figure 3.5b) and after (Figure 3.5a) intense storm episodes. A detailed analysis regarding the submesoscale restratification and the role of atmospheric forcing is provided in Chapter 4.

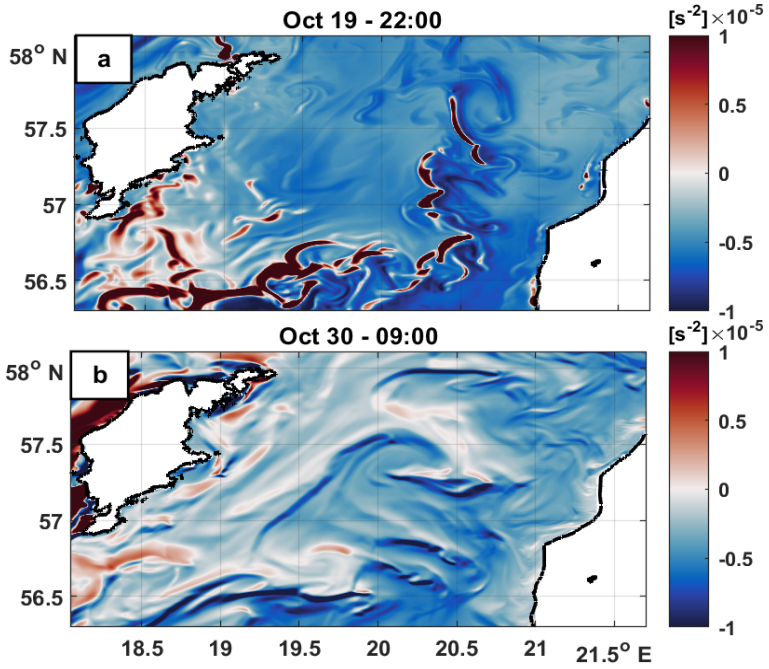

Figure 3.5: Buoyancy frequency squared N^2 (a) during the low wind conditions and relatively strong cooling, that followed the first wind event (19 October) and (b) during the last storm episode (30 October) that presented the highest wind speeds (for the atmospheric conditions see Figure 3.1). Both panels indicate near-surface instantaneous fields. Negative and positive N^2 values correspond to unstable and stable stratification, respectively. Values close to zero indicate neutral stability. Panel (a) corresponds to the same instance in time as Figure 3.4

In order to examine whether the conditions for SI are fulfilled in the Eastern Gotland Basin, different parameters relevant to this kind of instability are illustrated in Figure 3.6. Here, a snapshot (17 October) was chosen that represents the state in the basin during periods with relatively weak cooling. During that day, increased near-surface stratification is observed in most parts of the basin (Figure 3.6a). A lateral zone can be identified, with more stably stratified waters occupying the western side of the frontal structure whereas neutral or unstable stratification dominates the eastern part. This zone, found also on 25 October and 2 November, seems to arise during each low B_0 episode that follows the intense storm events.

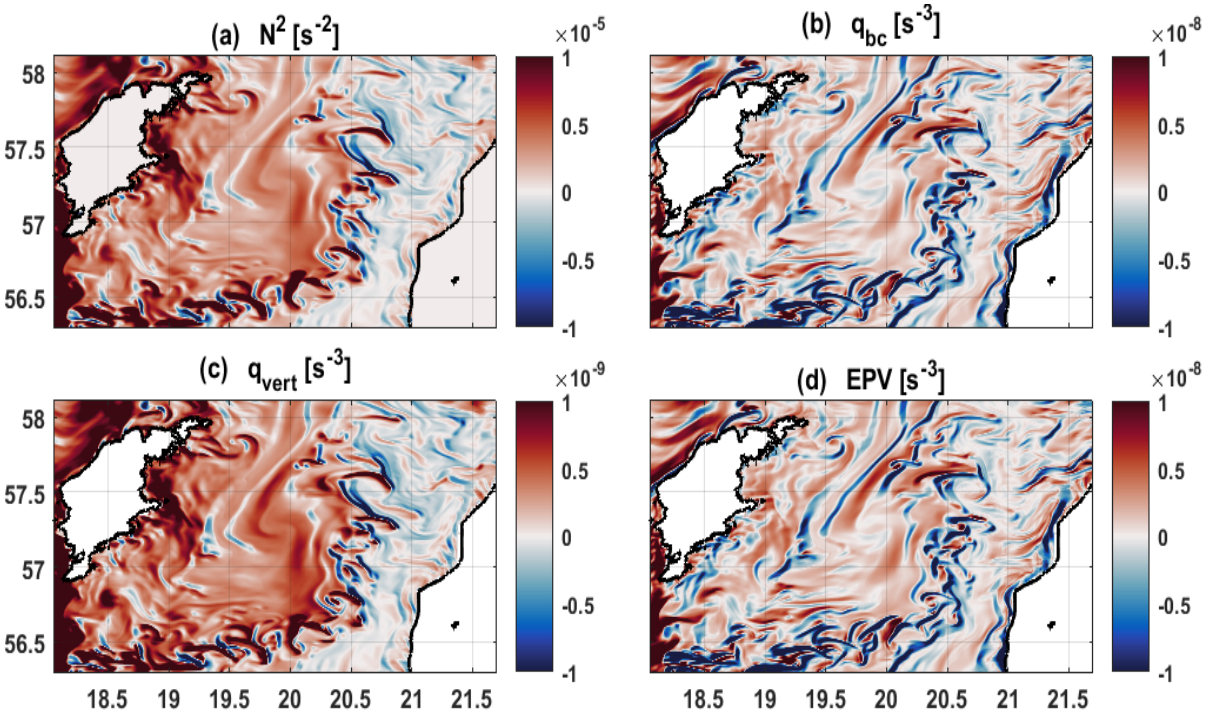

Figure 3.6: Investigation of Symmetric Instability (SI). (a) Buoyancy frequency squared N^2, (b) horizontal component of potential vorticity q_{bc}, (c) vertical component of potential vorticity q_{vert} and (d) Ertel Potential Vorticity (EPV). All patterns are near-surface instantaneous fields for 14:00 UTC 17 October 2017, a day representative of weak atmospheric buoyancy loss conditions.

Several regions, especially close to the main frontal pattern, are seen to fulfill the conditions for SI (see Chapter 1), presenting enhanced positive N^2 and q_{vert} values with $|q_{bc}| > q_{vert}$ (Figure 3.6). In those regions, the absolute vorticity ($f + \zeta$) takes the same sign with the Coriolis parameter, and the EPV the opposite sign of the Coriolis. This results in negative EPV values, indicating that SI is possible to occur. Figure 3.6 shows that the SI criteria are met mainly in the strong frontal and filamentary features that

emerge from the main frontal pattern. During the rest of the days, when strong winds or intense cooling dominate, SI is confined in small localized $N^2 > 0$ patches, that are formed by the sharp submesoscale features (not shown).

In order to examine further the effect of atmospheric forcing, timeseries of regions where SI is possible to occur is illustrated in Figure 3.7. The timeseries shows specifically the fraction of symmetrically unstable areas found in the basin during the period of interest, based on the SI criteria presented in Chapter 1 (see also Thomas et al., 2013b). The magnitude of the mean wind speed is also shown for comparison, whereas its direction is illustrated in Figure 3.1a. Note here, that although the wind direction was generally highly variable throughout the study period, during the sequential storm episodes both the wind speed and its direction remained spatially uniform over the basin. The fraction of symmetrically unstable areas is seen to increase during the first two storm episodes reaching almost up to 30% on 25 October. During those two episodes, the wind was blowing from a southern direction and can thus be characterized as "down-front" with respect to the frontal orientation. In contrast during the 30 October storm when "up-front" winds dominated in the basin, the SI areas are significantly reduced ($\sim$ 10%). During the rest of the days, almost 15% of the total domain (Eastern Gotland Basin) is found to be symmetrically unstable, a value that is still large considering that gravitational instability largely dominates.

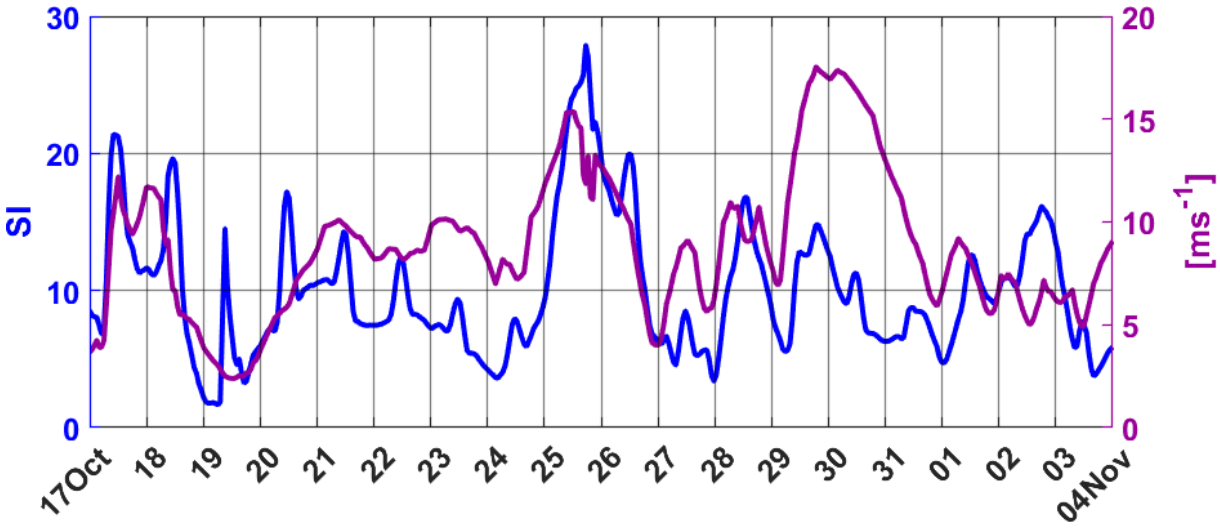

Figure 3.7: Temporal evolution of symmetrically unstable areas. Percentage of the total domain (Eastern Gotland Basin) where SI is possible to occur (blue line) and spatially averaged wind speed over the entire basin (purple line). The SI timeseries concerns near-surface fields and specifically for 5 m depth.

Note here, that in order to adequately resolve such a small scale instability as the SI high-resolution large-eddy simulations are commonly used (Thomas et al., 2013b, 2016). With the high-resolution numerical model used here, only the SI criteria can be investigated. Nevertheless, SI seems to be reinforced during storms, when strong "down-front" winds dominate, in agreement with previous findings (Thomas et al., 2013b, 2016). Several studies have shown that in the presence of lateral buoyancy gradients, gravitational overturning can be modified by thermal wind shear so that overturning occurs along the isopycnals that slant to the vertical when SI develops. This slantwise convection is further susceptible to baroclinic instabilities that accelerate the isopycnal slumping resulting in an increase of surface stratification (Haine and Marshall, 1998; Taylor and Ferrari, 2010).

3.3.3 The lifecycle of a submesoscale filament

In this section, the evolution of a cold submesoscale filament is investigated, from its generation until its destruction. In the previous sections, multiple submesoscale features were identified from the spatial distribution of the flow. The temporal evolution of dense elongated filaments is more evident, however, when focusing on individual patterns. An exemplary strong filament, formed at the vicinity of the main frontal pattern (see Figure 3.3 for position) is illustrated in Figure 3.8. This is a typical sharp filament, presenting high lateral buoyancy gradients, $|\nabla_h b|^2$, and a submesoscale width of around 6km. Note here the black contour that surrounds the filament in Figure 3.8a. This indicates the strong $|\nabla_h b|^2$ threshold ($|\nabla_h b|^2 = 10^{-13}$ s^{-4}) that will be used in the next chapters for isolating the strongest submesoscale features. This is a typical submesoscale filament presenting $\mathcal{O}(1)$ Ro and Ri_b number dynamics, with strong Ri_b values in its periphery and high cyclonic vorticities (positive Ro) in its center.

The complete lifecycle of this submesoscale filament from its initial formation and intensification through filamentogenesis, until its fragmentation is illustrated in Figure 3.9. The cold filament, which can be identified by the horizontal differences in temperature, started to form on 17 October and it was completely destroyed after almost three days. This is indicative of the ephemeral nature of submesoscale features (Lévy et al., 2012; Thomas et al., 2013a), as opposed to the larger scale mesoscale structures that can be maintained for several months. The existence of this lateral thermal gradient in combination with the ambient straining environment created favorable conditions for filamentogenesis (Capet et al., 2008a; Gula et al., 2014). The initially almost

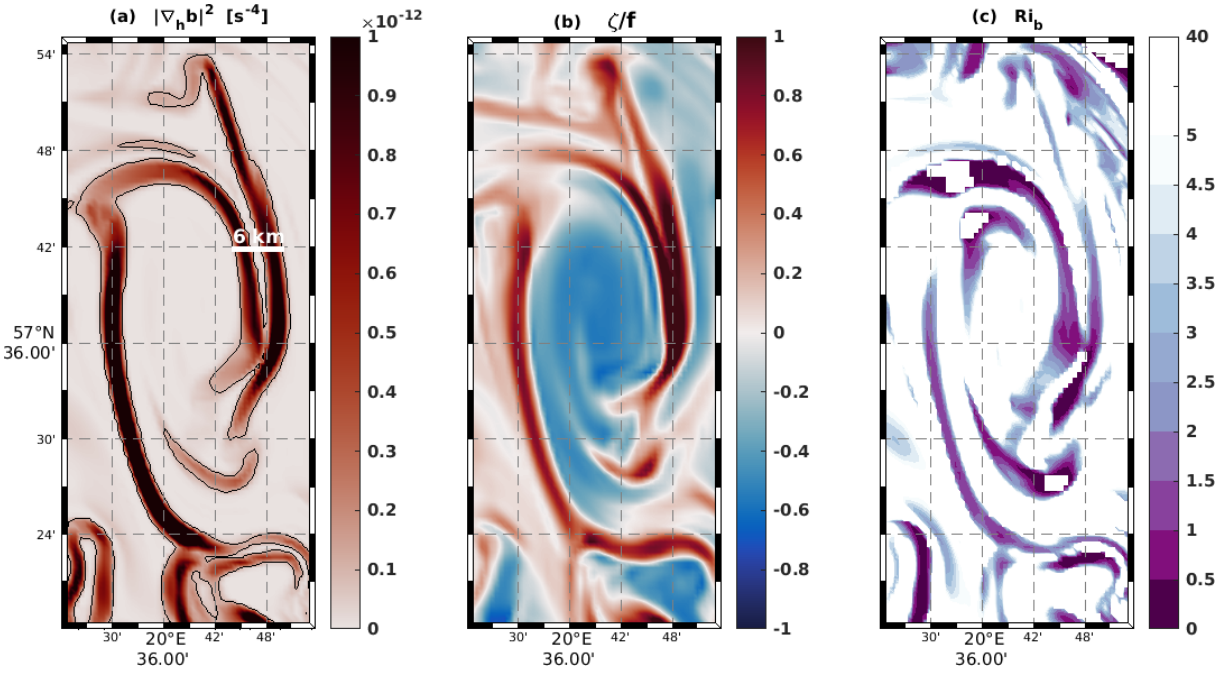

Figure 3.8: Submesoscale dense filament during the intensification phase. (a) Frontal sharpness defined as $|\nabla_h b|^2$. The black contour denotes the 10^{-13} s^{-4} threshold that is used in the following sections to delineate the sharp fronts and filaments. (b) Relative vorticity ζ normalized by the Coriolis frequency f. (c) Balanced Richardson number (only positive values are plotted). All patterns are near-surface instantaneous fields for the same instance in time as Figure 3.3. The width of the filament is around 6 km and its position is shown with a black rectangle in Figure 3.3.

elongated filament is seen to sharpen and become more curved as it gets stretched and deformed by the local shear flow and a small anticyclonic eddy that is developed on its western side.

During 18 - 19 October the filament was furthermore subject to "up-front" winds on its eastern side and "down-front" winds on its western side (see magenta arrows in Figure 3.9). The "down-front" winds contributed to the further intensification of the filament on its western side. Following the filamentogenesis stage, filamentary arrest dominated and the filament ultimately fragmented into a small vortex (last panel of Figure 3.9). This filamentary fragmentation has been seen by the high-resolution idealized simulations of Capet et al. (2008a) and by the realistic Gulf Stream simulations of Gula et al. (2014), both reporting that filaments might finally break into a train of submesoscales vortices due to development of small scale instabilities. The reason for this filamentary arrest can also be the restriction imposed by the model resolution that might lead to an artificially arrest when the width of the filament, which constantly

shrinks during filamentogenesis, comes close to the horizontal grid resolution of the model (McWilliams et al., 2015; Sullivan and McWilliams, 2018).

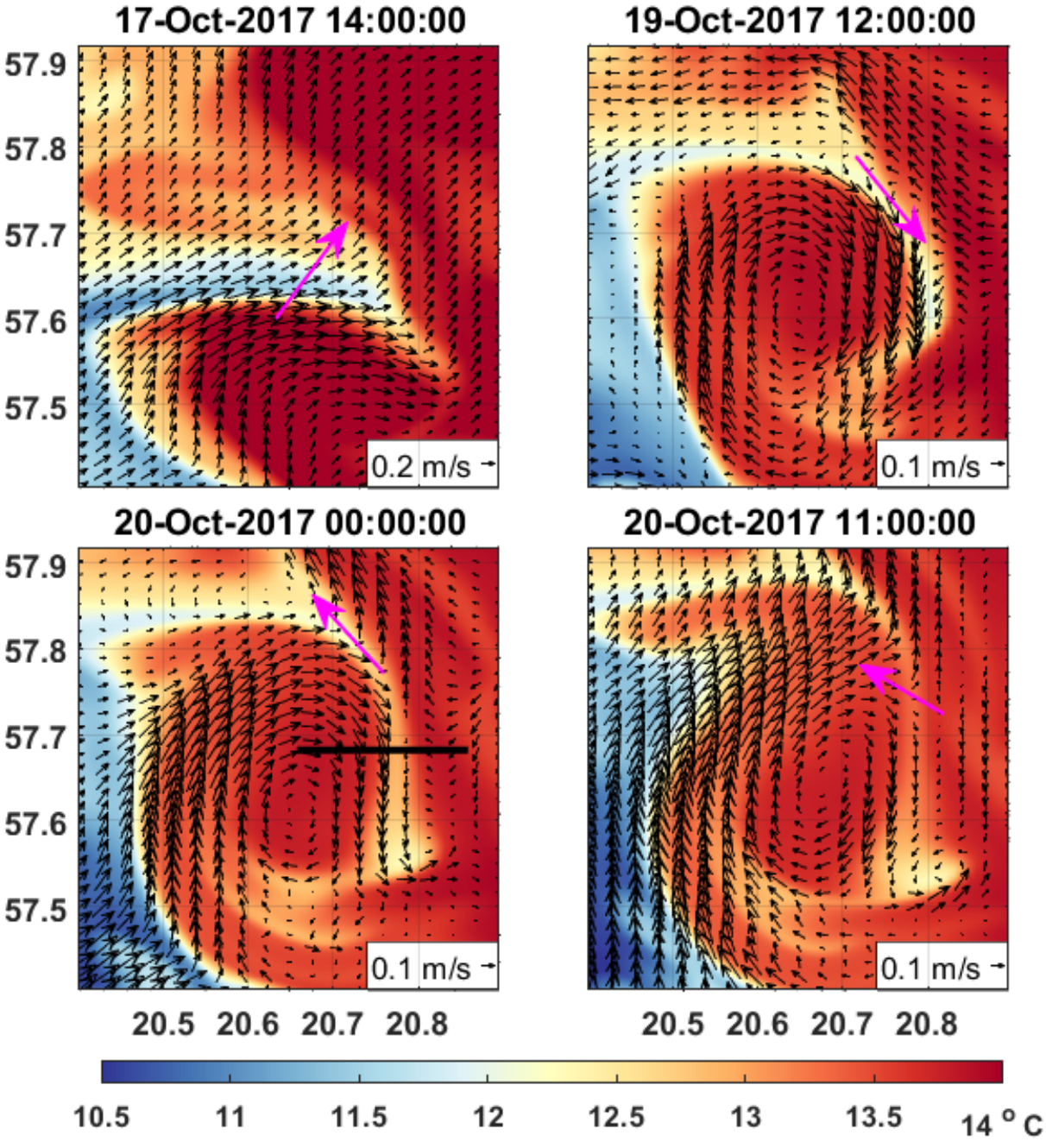

Figure 3.9: Lifecycle of a cold submesoscale filament. Instantaneous patterns of SST during the formation stage, the filamentogenesis process and the subsequent filamentary arrest. Black arrows indicate the surface circulation in the area of the filament. Magenta arrows show the approximate wind direction relative to the orientation of the filament. The black line in the third panel indicates the position of the transect shown in Figure 3.10.

A vertical cross-section of the filament along the black line of Figure 3.9 is shown in Figure 3.10, for 20 October. The vertical structure is typical of a submesoscale filament during the filamentogenesis processes, just before the filamentary arrest. During this stage, the filament is seen to present a temperature contrast of more than 1 K (Figure 3.10a). The Ro number shows high positive $\mathcal{O}(1)$ values in the center of the filament, with the maximum values appearing from the surface until $\sim$20 m depth. A local outcropping of the isopycnals is observed from around 40 m depth, which is slightly shallower than the outcropping seen in the filament of Figure 3.4. The strong secondary ageostrophic circulation that emerges decreases the width of the filament to approximately 2 km while sharpening the lateral buoyancy gradients (Figure 3.10b). The intense surface convergence of the flow towards the center of the filament creates a narrow downwelling channel in its middle with extremely high vertical velocities (Figure 3.10d,e). This secondary circulation emerges to restore the geostrophic balance and tends to dynamically slump the vertical isopycnals towards the horizontal. Generally, this small scale ageostrophic circulation is expected to emerge each time that the relative vorticity approaches the value of the Coriolis parameter (Ro $\sim$1), as first noted by Hoskins and Bretherton (1972).

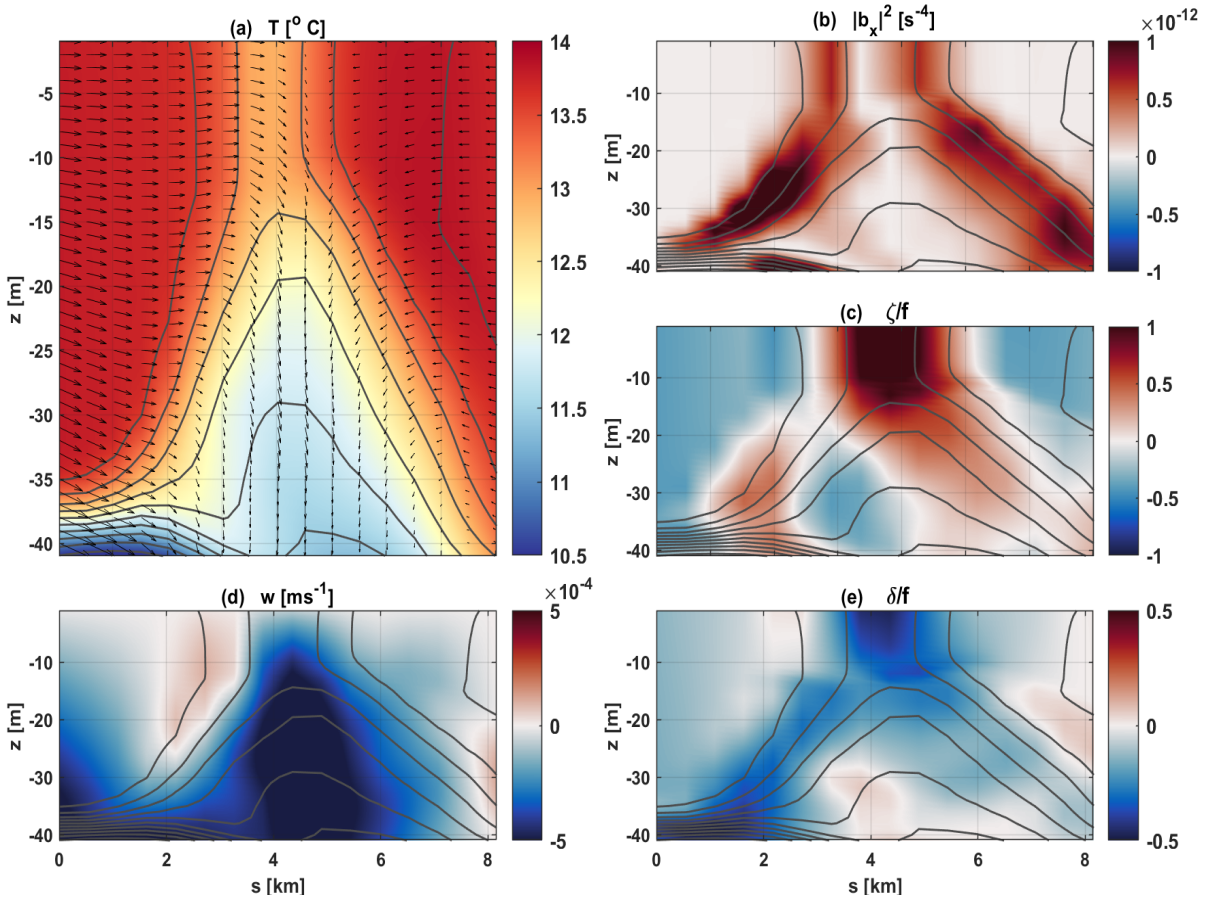

Figure 3.10: Vertical cross section of a submesoscale filament during the intensification phase. (a) Temperature structure with the secondary ageostrophic circulation shown with black arrows. (b) Lateral buoyancy gradient squared, (c) Rossby number, (d) vertical velocity, (e) divergence normalized by f. Gray contours in all panels denote isopycnals with a spacing of 0.05 kg m^{-3}. The x-axis indicates the total length of the transect with s=0 km corresponding to the beginning of the transect. The exact position of the transect is shown with a black line in Figure 3.9.

CHAPTER 4

Mixed layer depth modulation

Submesoscales manifest different kinds of instabilities that have the ability to restratify the Surface Mixed Layer (SML) by tilting the nearly vertical isopycnals towards the horizontal, thereby shoaling the Mixed Layer Depth (MLD). This shoaling can affect the marine biology in localized regions and might as well lead to biases in coarse resolution ocean models, where this subgrid-scale process is typically ignored in the existent SML parameterizations. This chapter aims to investigate the modulation of MLD by submesoscale flows during the passage of successive storm events by focusing on the Eastern Gotland Basin, that as shown earlier, is characterized by rich submesoscale activity. Here, the use of high-resolution numerical simulations extends previous idealized simulations (e.g., Couvelard et al., 2015; Whitt and Taylor, 2017) towards more realistic scenarios. First, the ability of submesoscales to create shallow and highly heterogeneous MLDs is highlighted. Then, the evolution of the SML stratification is examined during a series of wind episodes, in the presence of sharp lateral density gradients. Subsequently, the orientation of the front is explored in relation to the local bathymetry. The main question addressed in this chapter is whether submesoscales are able to maintain shallow MLDs during storms and quickly restratify the upper-ocean between several storm events.

4.1 Shoaling of the mixed layer

The upper ocean is characterized by a SML with a typical thickness from a few meters to several hundred meters (Garrett, 1996), within which the density is almost vertically homogeneous. Despite the significance of this layer, its exact determination is still arbitrary. It is commonly based on a threshold method according to which, the MLD is the depth at which temperature (sometimes even salinity) or potential density changes by a given threshold value relative to the one at a reference depth close to the surface (de Boyer Montégut et al., 2004). Here, following the approach of de Boyer Montégut et al. (2004), the MLD is diagnosed from the density field, based on a 0.03 kg m^{-3} criterion (i.e., $\Delta\rho = \rho\mid_z - \rho\mid_{z=0} > 0.03$ kg m^{-3}).

The Eastern Gotland Basin is generally characterized by strong stratification (see Section 2.1). During the study period (17 October - 04 November 2017) a mean MLD of approximately 35 m (Figure 4.1a) in its center is observed. Minimum MLD values are found close to the coast, whereas the deepest mixed layers of around 50 m are located close to the 60 m bathymetric contour, between the Gotland Deep and the coasts of Latvia. At these shallow regions, the MLD does not present significant changes, as indicated by the small values in its standard deviation (Figure 4.1b). The highest standard deviation values are found deeper, and specifically at the same position where the main frontal pattern appears (see Figure 3.2). There, the standard deviation is almost double compared to the ambient waters (16 m versus 9 m) which, as will be shown below, is indicative of the large modulation of the MLD by submesoscales.

A sequence of MLD snapshots for two different days, reveals the efficiency of frontal and filamentary patterns in reducing the MLD through restratification, i.e., bring warm water above cold water (Figure 4.2). By comparing Figure 4.2a,b with Figure 4.2c,d it is evident that the shallower MLDs correspond to the highest lateral buoyancy gradients, $|\nabla_h b|^2$. The most effective MLD shoaling is found for $|\nabla_h b|^2$ above 10^{-13} s^{-4}, which is identical to the threshold introduced in Section 3.3.3, in the context of Figure 3.8a, to delineate pronounced filamentary features. This threshold will be thus used in the following sections to distinguish between the small-scale frontal regions and ambient waters. The signature of the cold submesoscale filaments shown earlier (see Figure 3.3) is imprinted also in the MLD. Due to the tilting of the isopycnals during the restratification process, the shallowest stratification is found at the edges of these features, that present also the highest lateral buoyancy contrasts. Note here the highly heterogeneous MLD patterns formed by the strong frontal structures.

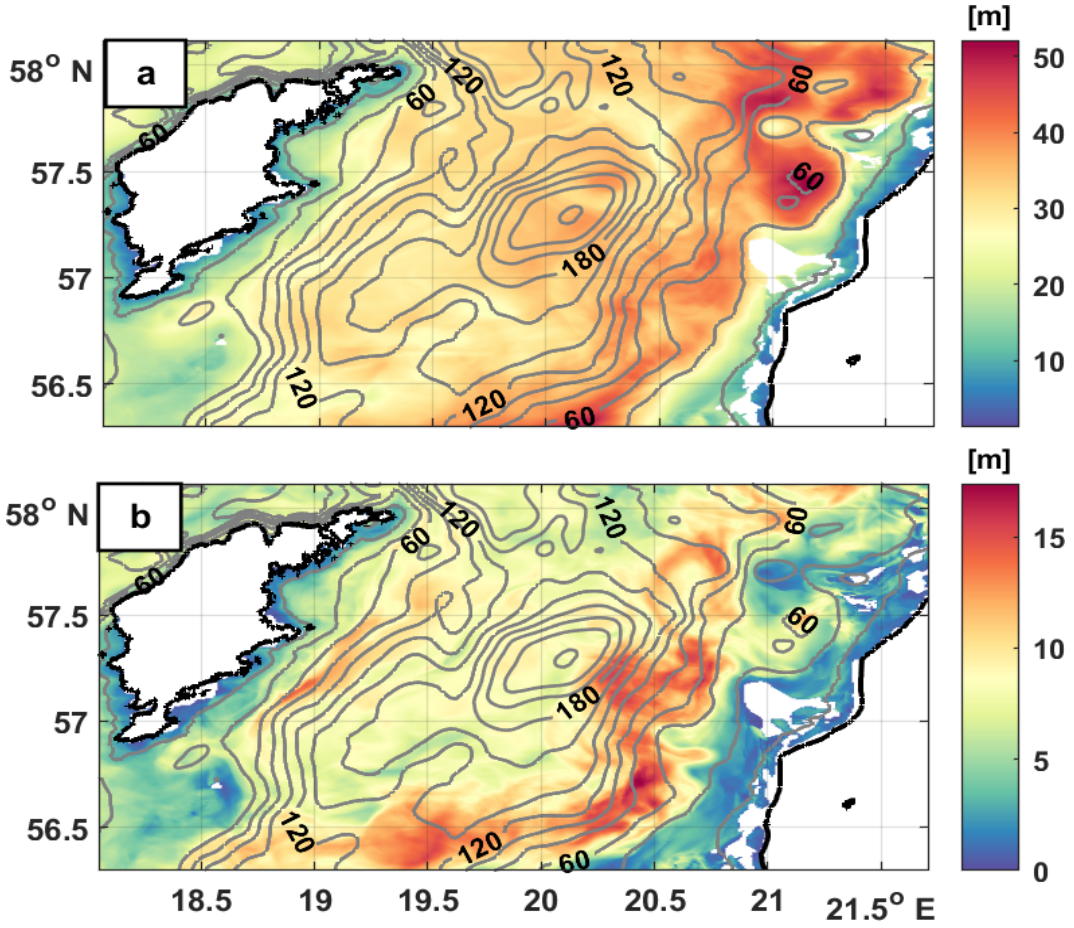

Figure 4.1: (a) Mean Mixed Layer Depth (MLD) and (b) standard deviation of the MLD in the Eastern Gotland Basin during the period of interest (17 October - 04 November 2017). Gray contours indicate the bathymetry in the area with a 20 m interval. White areas show waters well-mixed down to the bottom, more pronounced near the coast of Latvia.

The MLD is substantially shallower in the frontal and filamentary features compared to the ambient waters (Figure 4.2), with the difference being more evident in Figure 4.2b , where the successive wind events have deepened considerably the MLD. At this time, the largest MLD of 50-60 m outside the frontal areas is contrasted by a MLD of only 10-20 m in the center of the filaments. The eastern part of the basin is occupied mainly by waters well-mixed down to the bottom (shown as white areas in Figures 4.2a,b). According to Leppäranta and Myrberg (2009), the strong bathymetric difference between the Latvia coast and the Gotland Deep yields, in the long-term mean, a lateral zone with waters mixed down to the bottom in the shallower eastern parts of the Gotland Basin, and more stratified waters, in the deeper western areas. In the deeper areas, the strong stratification that underlies the SML most likely serves to constrain the enhanced deepening of the MLD during the intense wind events.

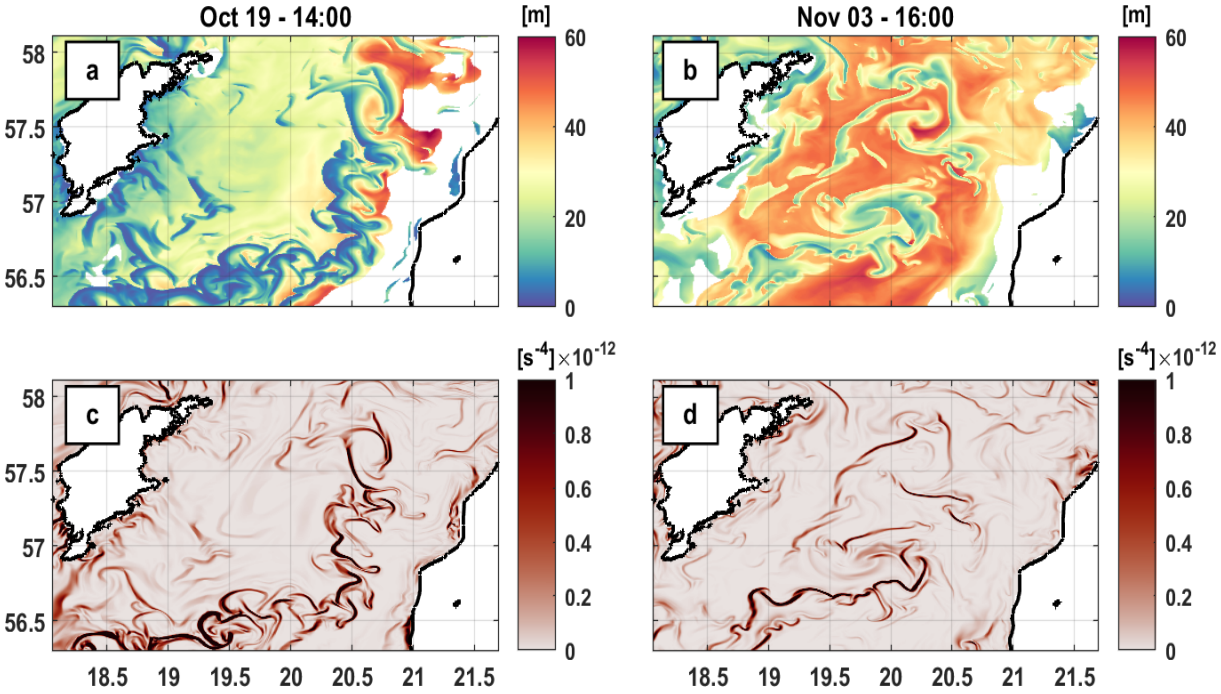

Figure 4.2: Shoaling of the mixed layer by submesoscale features. (a,b) Plane view of MLD and (c,d) frontal sharpness, defined here as $|\nabla_h b|^2$, during low wind conditions (19 October, same instance in time as Figure 3.3) and during the restratification phase that followed the successive wind events (03 November). White areas in panels (a) and (b) indicate waters well-mixed down to the bottom that are more pronounced close to the coast of Latvia.

4.2 Evolution of the mixed layer

In order to investigate the spatial and temporal evolution of the MLD, a Hovmöller diagram is used here (Figure 4.3). Since the main frontal pattern is characterized by an approximately meridional orientation (see Sections 3.2 and 4.3), the zonally averaged MLD as a function of time was chosen. The MLD is highly variable during the study period presenting minimum values in the locations that correspond to the strong lateral density gradients. At the beginning of the study period, the sharp submesoscale filaments and fronts occupied almost the entire domain with an approximately north-south orientation, extending from 56.4°S to 57.8°N, as can be seen by their imprint on MLD (Figure 4.3, see also 4.2c and 3.3). The upwelling favorable winds during the 18 October wind event and the calm weather conditions that followed (for atmospheric conditions see Figure 3.1) contributed to the strengthening of the lateral temperature contrasts and to the development of energetic filaments that reduced further the MLD to ∼15 m (Figure 4.3).

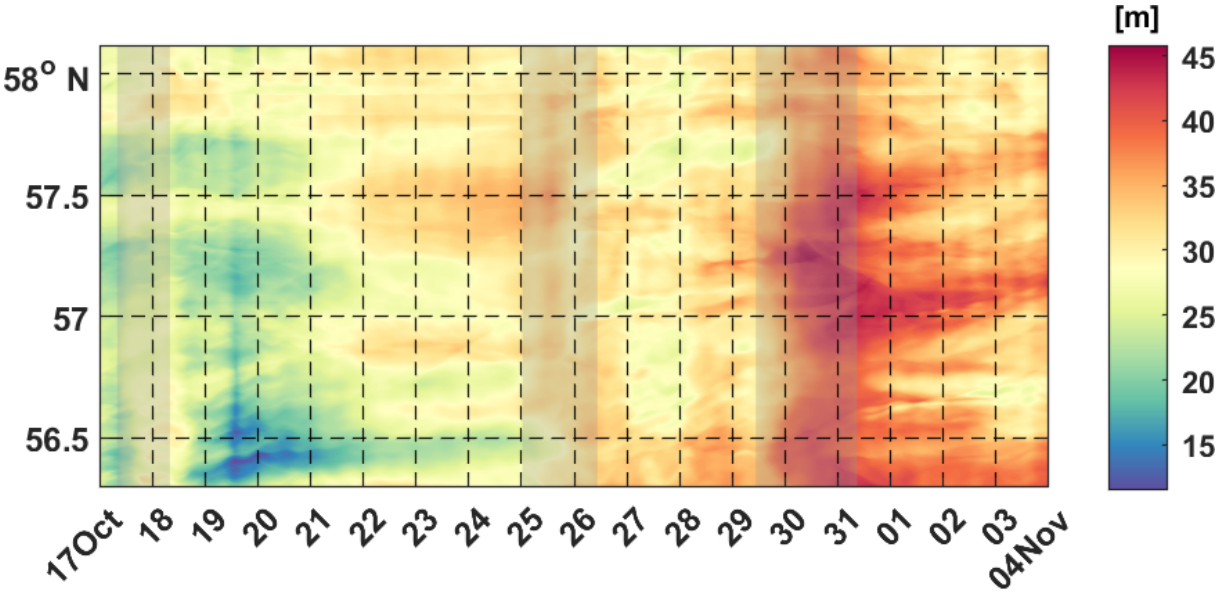

Figure 4.3: Hovmöller diagram of the zonally averaged MLD during the entire study period. Gray shaded areas indicate the approximate duration of the three successive wind episodes (for atmospheric conditions see Figure 3.1).

The succeeding days, and before the first intense storm (25 October), the shoaling of the SML remained more pronounced in the southern parts of the basin. The 25 October wind episode deepens and homogenizes the SML. The emergence of filaments and the restratification phase that begins when the wind subsides shallow the SML approximately by 10 m (from 35 to 25 m), but the shoaling is quickly interrupted by the next storm (30 October) that deepens it substantially again (Figure 4.3). This sequence of continuous wind phenomena generates an intense MLD variability, where for the same location, e.g., at 56.5 °N, almost 25 m difference in 5 days is found. This variability is more pronounced inside the submesoscale features, although away from the filaments, surface convection due to atmospheric cooling and wind-induced turbulence, also modifies the SML.

To better assess the effect of storms on MLD and compare its response inside and outside fronts, the flow was decomposed into frontal and non-frontal regions. This was done by applying a feature extraction method, based on the most relevant flow characteristic (Mohammadi-Aragh et al., 2018, 2020). Motivated by the good correlation between the sharp horizontal density gradients and the shallow MLDs (Figure 4.2), the frontal regions were defined based on a lateral buoyancy gradient threshold, i.e., $|\nabla_h b|^2 > 10^{-13}$ s^{-4}. Note here that all results presented in the following are not overly sensitive with respect to small changes in this threshold value. For clarity, frontal and non-frontal regions defined according to this criterion will be designated hereinafter

as "Front" and "No-Front", respectively. Using this criterion, binary maps were constructed and applied to MLD (Figure 4.4). A comparison with the Ro number maps (see Figure 3.3b) indicates that this technique is capable of isolating the $\mathcal{O}(1)$ Ro fronts and filaments.

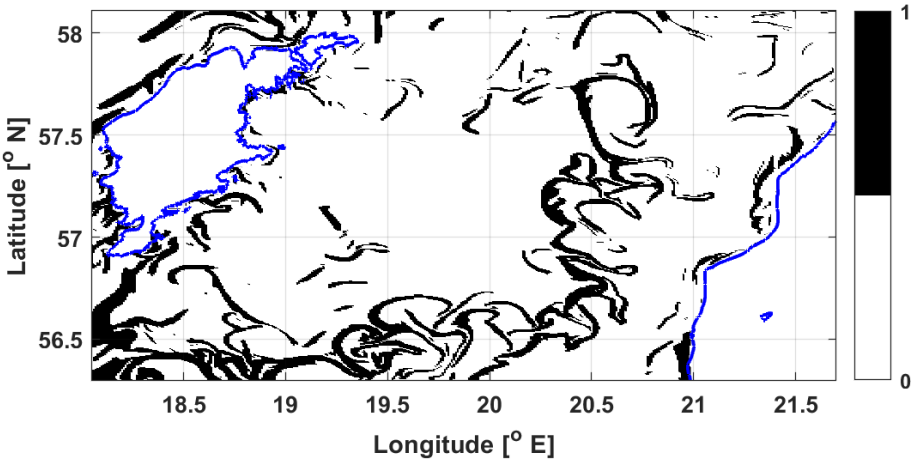

Figure 4.4: Binary map snapshot constructed based on the feature extraction method. Black regions correspond to sharp fronts and filaments defined as those features where, $|\nabla_h b|^2 > 10^{-13}$ s^{-4} ("Front"). White areas correspond to the ambient waters ("No-Front").

The fractions of the study area (Eastern Gotland Basin) occupied by the "Front" (blue line) and "No-Front" (red line) regions, respectively are shown in Figure 4.5a. Although only around 14% of the total domain is occupied by strong frontal features (blue line in Figure 4.5a), their effect on MLD is significant, as will be shown in the following. High-gradient frontal features, often characterized by submesoscale dynamics as previously mentioned, are seen to be more abundant at the beginning of the study period when the coastal upwelling and the calm weather conditions contributed to their horizontal extension and to the enhancement of density contrasts. During storms, however, the "Front" fraction decreases since intense winds act to destroy the gradients. At the end of the study period, the sharp filaments that developed after the 30 October wind event, cover only a small fraction of the domain.

The response of the MLD to storms, which is the main focus of this chapter, can be seen in Figure 4.5b. Three different regions are illustrated termed analogously to the definition used above. (I) "MLD": basin-averaged MLD that includes the entire domain; (II) "MLD-Front": MLD averaged over all small-scale frontal regions based on the $|\nabla_h b|^2$ criterion; and (III) "MLD No-Front": MLD averaged over the non-frontal

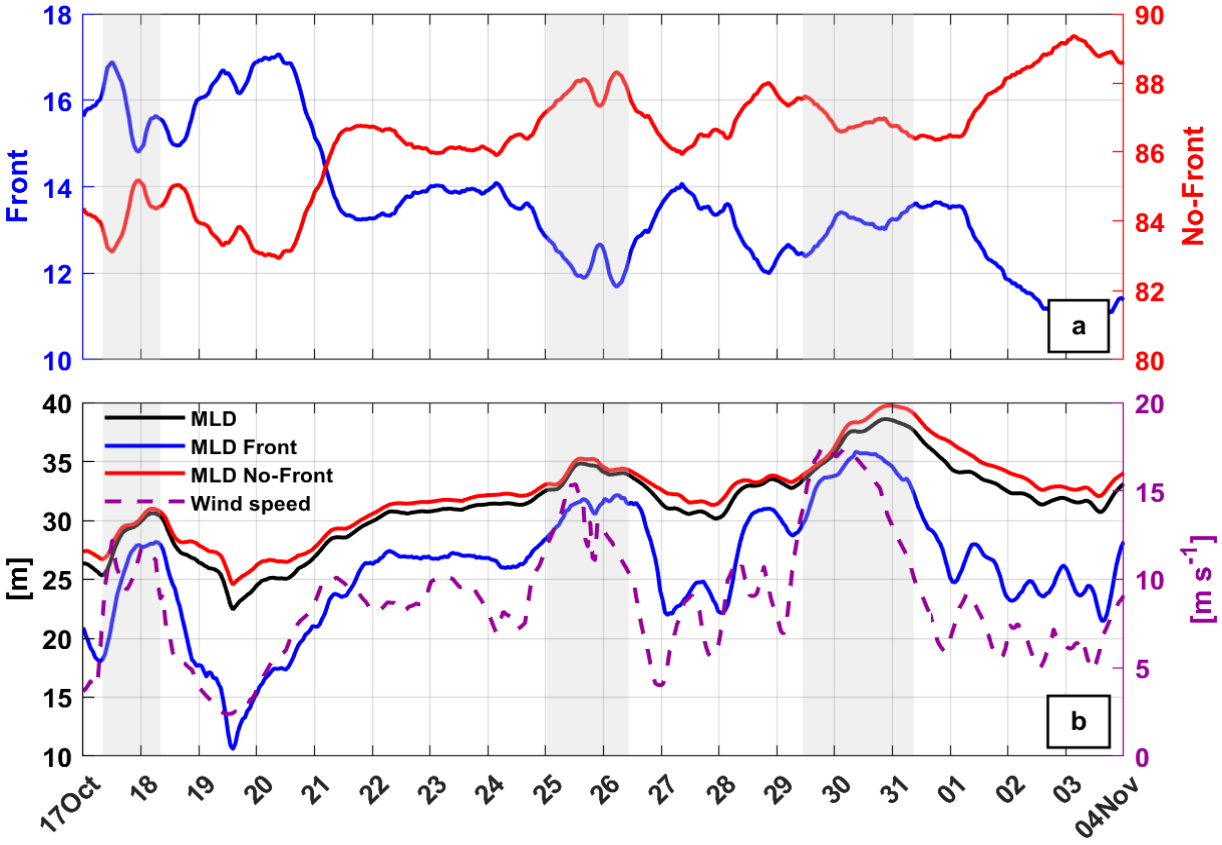

Figure 4.5: Temporal evolution of frontal features and MLD. (a) Percentage of the domain covered with intense lateral buoyancy gradients ("Front", blue line) and without ("No-Front", red) strong gradients, based on the $|\nabla_h b|^2 = 10^{-13}$ s^{-4} threshold. (b) Spatially-averaged time-series of mixed layer depth (left axis) and wind speed (right axis). Mixed layer depth for the entire domain, termed as "MLD" (black line), for the frontal structure, termed as "MLD-Front" (blue), without the front, "MLD No-Front" (red) and wind speed (purple dashed line) for comparison. Light gray shaded areas in both panels indicate the approximate duration of the three successive storm episodes.

regions. The wind speed is also shown for comparison. It is evident that the MLD follows, in general, the variations in the wind speed in all cases, with a small-time lag that reflects the quick restratification time scale. By completely excluding the frontal structures (red line), the MLD becomes slightly deeper. Yet, a comparison between the "MLD" and "MLD No-Front" cases shows that there are no significant differences due to the fact that the frontal structure occupies only a small fraction of the domain and the applied lateral buoyancy gradient threshold is quite high, hence only strong features are included.

Vice-versa, in the "MLD-Front" case (blue curve), focusing exclusively on the frontal regions, the MLD remains substantially shallower during the entire period and shows higher variability. Frontal and filamentary patterns are seen to serve not only for increasing the shoaling after each of the sequential wind events but also for limiting the deepening of the MLD during storms. As seen before, the shoaling of the MLD is more pronounced after the first wind episode (19 October), where upwelling-favorable winds and the calm weather conditions that followed strengthened the frontal features and contributed to the intense restratification of the SML. The higher variability of MLD in the "MLD-Front" case and the quick restratification after each wind episode, which is performed in almost one day, clearly illustrates the efficiency of the restratification process in agreement with previous studies (e.g., Boccaletti et al., 2007).

In the idealized simulations performed by Mahadevan et al. (2010) it was found that "down-front" winds can arrest the submesoscale restratification by creating a destabilizing Ekman transport, that advects dense water over light water. The results presented here, however, suggest that frontal patterns can maintain the vertical stratification in the SML even under the action of intense "down-front" winds and strong buoyancy loss. This is consistent with the findings of Whitt and Taylor (2017), that studied the restratification during a storm event by using LES simulations, and with Couvelard et al. (2015) that focused on the effect of buoyancy loss by cooling a zonal jet, both showing that submesoscale restratification has the ability to compensate the destratifying effect of atmospheric forcing.

4.3 Frontal orientation

Earlier studies suggested that ageostrophic flows evolve on inertial f^{-1} time scales. In a recent study, however, Callies et al. (2020) found that submesoscale turbulence, at scales smaller than 10 km, can evolve on time scales similar to or shorter than the inertial period, displaying characteristics of a subinertial flow that is geostrophically balanced to leading order. At those time scales, the flow arising from a density front is expected to be approximately in geostrophic balance, with the flow being predominantly oriented in the along-front direction (Ullman and Cornillon, 1999). Assuming that SST fronts are not salinity-compensated and density contrasts are present, like the frontal pattern investigated here, then the orientation of the front indicates the direction of the along-front flow (Ullman and Cornillon, 2001). The frontal orientation is generally considered to be normal to the direction of the lateral SST gradient, in an average sense.

It is well known that topography in the oceans acts to constrain the flow on a range of scales. Ullman and Cornillon (1999) used a relationship between the direction of the lateral SST gradient with respect to the bathymetry gradient in order to classify continental shelf fronts, appearing in satellite images in the northeast US coast. Although the proposed generation mechanism of those fronts was primary the strong surface cooling during winter, associated also with salinity differences, they showed that most of the examined frontal features were aligned to the bottom topography. In the Baltic Sea, earlier studies (Kahru et al., 1995; Pavelson et al., 1997) have shown, through the use of satellite images, that large scale fronts are not only aligned to the coastline and isobaths but occur mainly in areas with straight and uniformly sloping bottom topography.

To examine whether this alignment applies also in the simulated autumn front studied here, frontal probability maps were constructed for the period of interest (Figure 4.6). Following the methodology introduced in Section 4.2 the probability was calculated based on the $|\nabla_h b|^2 > 10^{-13}$ s^{-4} threshold and then the mean value was considered. Although this threshold excludes weak fronts that may be abundant in the basin, those features are not expected to contribute significantly to the SML restratification and are, therefore, in that sense, of minor importance. The main frontal pattern is seen to be oriented in an approximately north-south direction during the entire study period. Figure 4.6a shows that the strongest frontal features are more likely to arise in the steep bathymetric slope that is found between the Gotland Deep and the coasts of Latvia.

In the first half of the study period, just before the 25 October wind event, the probability of frontal alignment with the bathymetry gradients is even higher, reaching up to 80% in some regions of the front (Figure 4.6b). This can be explained by available $|\nabla_h b|^2$ snapshots (not shown) indicating that the strong winds that followed smoothened and displaced the frontal pattern to the West. These probability maps suggest that the position of the main frontal pattern, which seems to be generated by the upwelling favorable winds and the general cyclonic circulation in the basin, might be related to the differences in topography.

Besides the main front, high probability is also detected at the southern part of the Gotland island, where the cold upwelled waters increase the temperature contrasts, and along the Latvian coastline (Figure 4.6) although in the latter case submesoscale features are not quite abundant. In this area, lateral salinity differences are seen to dominate over temperature (see Figure 3.4a,b) and the thin front that forms is largely

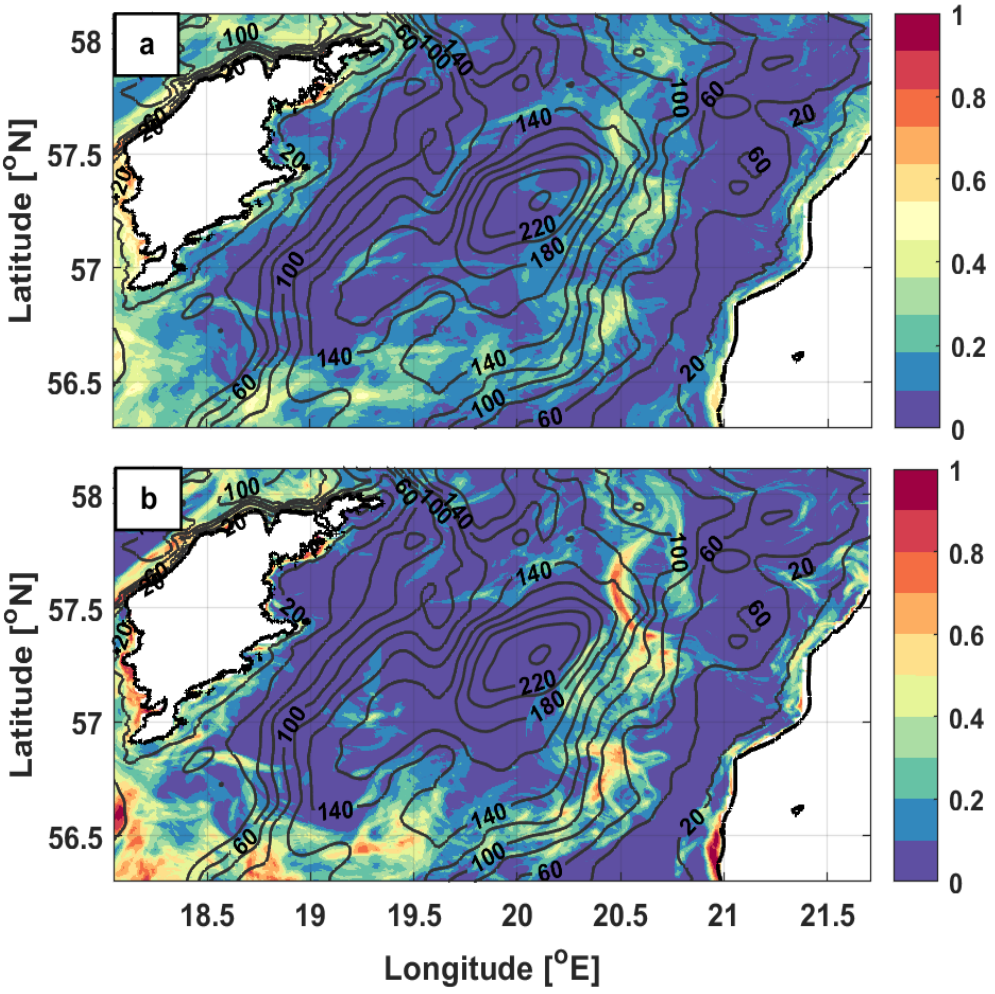

Figure 4.6: Mean frontal probability (a) during the entire study period and (b) during the period 17-24 October, just before the 25 October wind episode. The probability was calculated based on the $|\nabla_h b|^2$ threshold. Values of one correspond to areas where $|\nabla_h b|^2 > 10^{-13}$ s^{-4} during the period of interest, whereas values close to zero indicate regions where the lateral buoyancy gradients are small ($|\nabla_h b|^2 < 10^{-13}$ s^{-4}). The bathymetry of the area is shown with black contours, with a 20 m interval.

salinity-controlled. Although a thorough study of this front is beyond the scope of the current thesis, its persistence might be associated with the freshwater discharge from the Vistula river and the differential cooling observed between the shallower eastern regions and the deeper more stratified waters on the west. Different mechanisms such as the direction of the wind forcing can also play a role in intensifying the already established gradients, as has been noted in previous studies investigating near-shore frontal features (Ullman and Cornillon, 2001). Specifically, Csanady (1978) showed that cross-shore winds directed onshore (from the sea towards the coast) and normal to the orientation of the front, like the ones observed locally during autumn at the coasts of Latvia

(see Figure 3.2b), can create an offshore pressure gradient by raising the sea level at the coast (and vice versa). This pressure gradient can be opposed by the frontal gradient if the latter is directed onshore, which is the case here since the cold waters are close to the coastline (Figure 3.2a). Therefore, if only temperature gradients were present those two opposing gradients would tend to weaken the front (Ullman and Cornillon, 2001). However, since the front here is largely salinity-controlled (Figure 3.4b) with less saline waters found close to the shore, the salinity gradient is directed offshore in alignment with the pressure gradient. This implies that the wind forcing might act to reinforce and sustain this thin frontal feature.

In summary, the probability maps suggest that during the period examined here the main frontal pattern is oriented in an average sense along the isobaths. The frontal orientation is of great interest since fronts can presumably act as a barrier to the cross-shelf exchange of properties and tracers. Moreover, in areas where the frontal probability is large, the MLD is expected to be significantly shallower and present higher variability than the neighborhood regions. This can be seen by comparing Figures 4.6a and 4.1b. It has been suggested that the shallow and highly variable MLDs can induce heterogeneous and patchy phytoplankton blooms in localized regions (Mahadevan, 2016).

CHAPTER 5

Submesoscale frontal mixing

Fronts are sites where near-surface stable stratification and vigorous turbulence and mixing coexist. Frontal instabilities enhance the turbulence levels while inducing a secondary circulation that acts to restratify the flow, by bringing warm water to the surface and cold water to depth. This chapter starts by exploring the physically and numerically induced mixing in the model, in the presence of fronts. First, the spatial distribution of upper-ocean mixing during a restratification event is shown. Then, the behavior of mixing is investigated based on the Rossby number for assessing the contribution of the different dynamical regimes to mixing. By applying the same methodology to MLD, the restratifying effect of submesoscales is highlighted, using a different procedure than the one adopted in Chapter 4 (i.e., $|\nabla_h b|^2$ threshold). Then, the mixing coefficient is used to investigate the complex interplay between processes that act to reduce the near-surface stratification and submesoscale restratification that tends to create stably stratified patches. The main question addressed in this chapter is whether submesoscales can maintain high mixing efficiency in localized regions during storms, that challenges the traditional view of a well-mixed SML that presents inefficient near-surface mixing. Using the Baltic Sea as a natural laboratory for studying those processes, new insights are provided also into the significance of frontal mixing in this brackish basin, where vertical mixing plays a key role in the ecosystem dynamics.

5.1 Physical and numerical mixing

5.1.1 Spatial distribution

To estimate the physically and numerically induced mixing in the model, in the presence of sharp frontal features, the diagnostic method of Burchard and Rennau (2008) is applied here (see also Section 2.2). This method was successfully applied by Gräwe et al. (2015) for discussing the advantages of vertically adaptive coordinates versus sigma coordinates. In this diagnostic method, the physical mixing [Eq. (2.2)] of any arbitrary tracer in the model is treated as the decay rate of the turbulent mean tracer variance, including both the contribution from the lateral processes, which are being parameterized based on Smagorinsky [Eq. (1.12)] and the vertical mixing. On the other hand, the numerical mixing [Eq. (2.1)] arising from the discretization errors of the advection schemes, is defined as the decay rate between the advected square of the tracer variance and the square of the advected tracer (Burchard and Rennau, 2008).

To investigate the physical and numerical mixing in the model, near-surface mixing snapshots for temperature and salinity are illustrated in Figure 5.1, for 17 October. While the physical mixing of temperature is low in most parts of the basin, elevated values appear in the main frontal pattern and along the edges of the filaments where the lateral thermal gradients are strong (Figure 5.1a). In those areas, the mixing of salinity is relatively low (Figure 5.1c). This can be explained using the results of Section 3.3.1, where a prevalence of temperature over salinity in setting the lateral density differences, was shown. Maximum salinity values are detected in this snapshot at the southern part of the Gotland island due to the intense upwelling. Enhanced salinity mixing is observed also along the coasts of Latvia, in the area of the thin elongated salinity-controlled front that was presented in Figure 3.4.

The numerical mixing of tracers (Figure 5.1b,d) presents both positive and negative values. Although the Superbee scheme, used here, has often an anti-dissipative behavior, and thus negative mixing would be expected, lateral shear and baroclinic instability experiments performed by Mohammadi-Aragh et al. (2015) showed that during the development of the instabilities Superbee can show a dissipative behavior and act locally to smoothen the lateral gradients, yielding increased mixing and dissipation rates. This will be further analyzed below. By comparing Figures 5.1(a,c) with 5.1(b,d) respectively, it is evident that the numerical and the physical mixing are highly correlated, presenting not only the same patterns but also similar order of magnitude val-

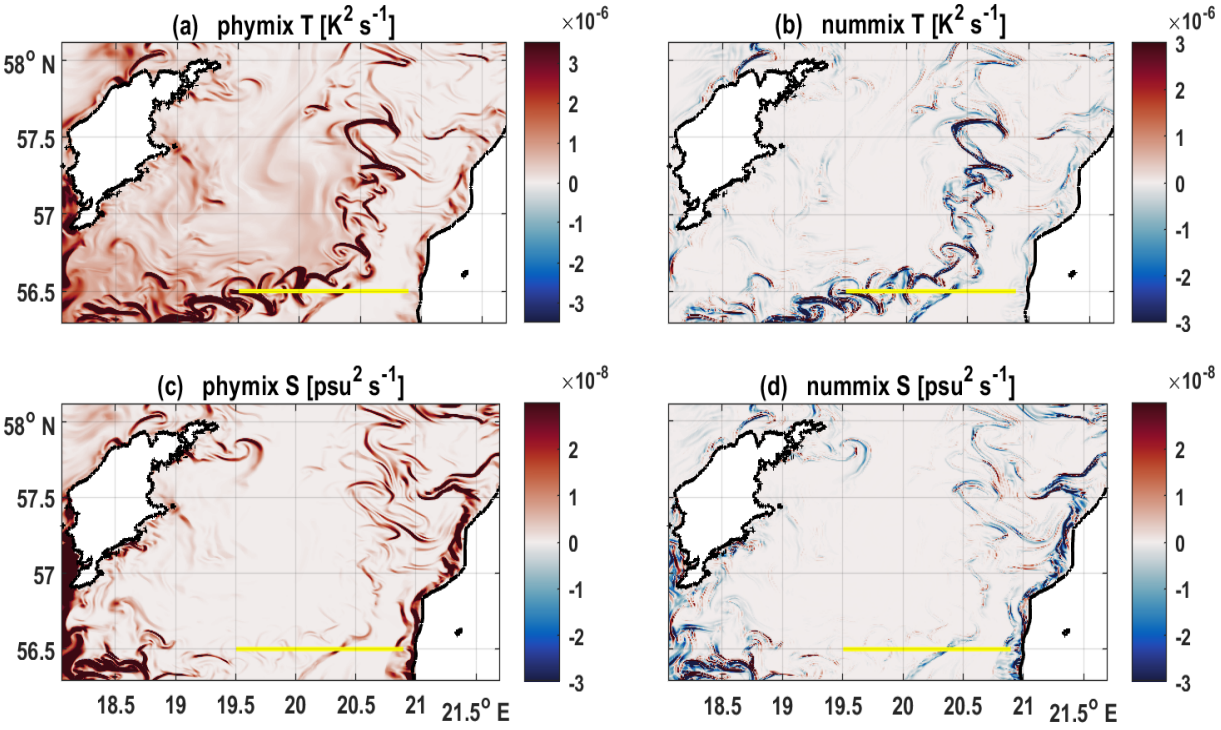

Figure 5.1: Instantaneous physical and numerical mixing of tracers in the Eastern Gotland Basin. (a) physical and (b) numerical mixing of temperature, (c) physical and (d) numerical mixing of salinity. All patterns are surface snapshots for 10:00 UTC 17 October 2017. The yellow line indicates the location of the transect used in Figure 5.2.

ues in some regions, partially with an opposite sign. This behavior has been studied by Hofmeister et al. (2010) and similar findings were reported in the Baltic Sea simulations of Gräwe et al. (2015).

In order to investigate the vertical structure of mixing, an east-west transect across the strong submesoscale filaments, formed at the southern part of the basin, was chosen (Figure 5.2). The location of the transect is indicated in Figure 5.1. The high correspondence between physical and numerical mixing seen previously in the horizontal distribution is also found in the vertical. Elevated temperature mixing is detected in the area of the pycnocline (Figure 5.2a,b), whereas enhanced salinity mixing is found in the interior stratified region below 55 m depth (Figure 5.2c,d). Closer to the surface, the mixing of temperature increases along the outcropping of the isopycnals (shown with gray contours) that actually mark the position of frontal and filamentary features (Figure 5.2a). This can be interpreted as a sign of high mixing inside those structures. As expected, the area between 20.5° and 20.7°E, which is usually occupied by waters well-mixed down to the bottom (see Figure 4.2a,b) does not present elevated mixing.

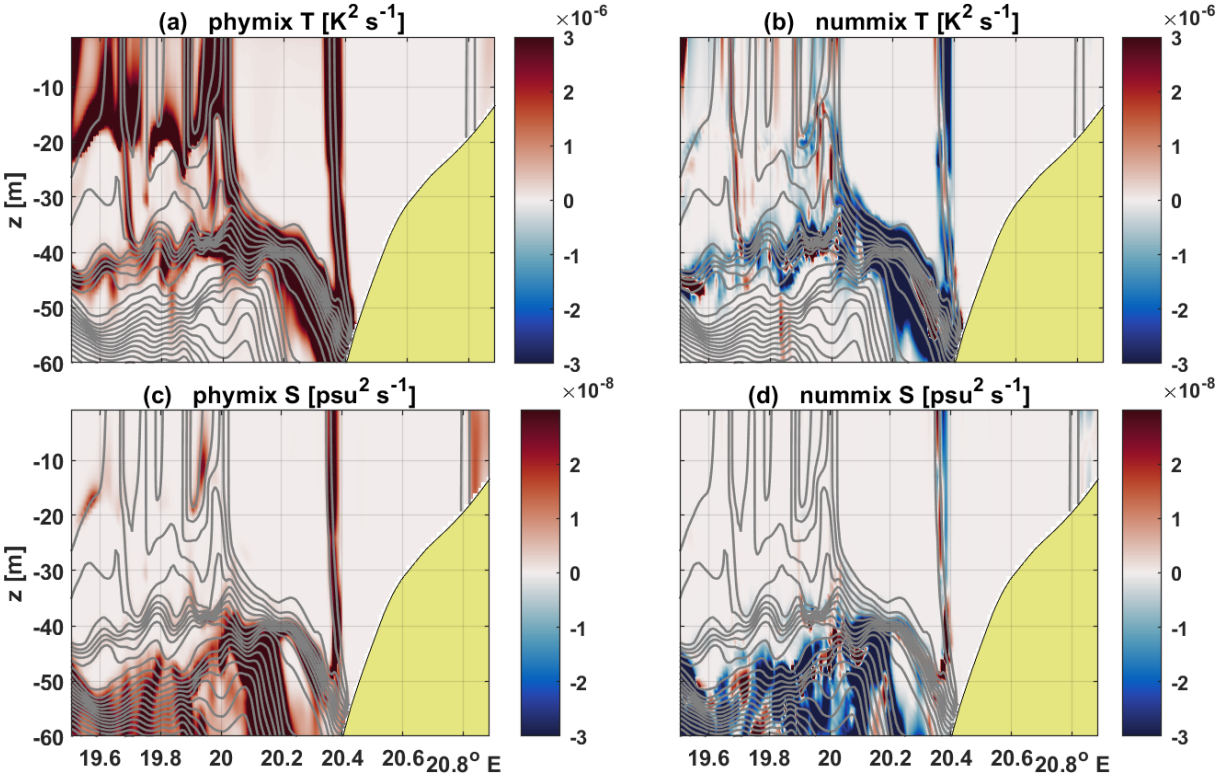

Figure 5.2: Vertical structure of (a) physical and (b) numerical mixing of temperature, (c) physical and (d) numerical mixing of salinity. The position of the transect is shown in Figure 5.1 with a yellow line. All patterns are surface snapshots for 10:00 UTC 17 October 2017.

5.1.2 Rossby number binning

For evaluating the physical and numerical mixing induced by the various dynamical processes in the SML, a binning technique was applied. While in the previous chapter the binning was based on the $|\nabla_h b|^2 > 10^{-13}$ s^{-4} threshold, allowing essentially only two bins representing the frontal areas and the ambient waters respectively, a slightly different approach is adopted here. Focusing only on temperature, which as shown above, is the most relevant tracer in this study, the binning of physical and numerical mixing was performed based on the Rossby number (Ro). This allows the delineation of different dynamical processes such as mesoscale and submesoscale, assuming that those can be identified by the Ro values, as has been shown before (Mohammadi-Aragh, 2014). As a first step, a total of 280 bins were constructed by using a range of Ro values extending between -14 and 14, i.e., the maximum and minimum values occurring in the basin, and by applying a bin size of 0.1. The bin size was chosen accordingly in order to reduce noise levels. Subsequently, the numerical and physical mixing in each grid cell was binned according to its Rossby number class.

As a result, the binning of physical temperature mixing in the Eastern Gotland Basin during the strong restratification phase observed on 19 October is illustrated in Figure 5.3. It is evident that most of the volume-integrated mixing is concentrated in a narrow band around zero, presenting one peak for Ro ~ 0 and another one for the Ro ~ 1 (Figure 5.3a). Those two peaks might correspond to mesoscale and submesoscale dynamics respectively, presuming that Ro is sufficient for identifying the different dynamical regimes (Mohammadi-Aragh, 2014). The volume per Rossby number class displays a Gaussian distribution confined around zero (Figure 5.3b). This suggests that rotation effects dominate the upper-ocean flow, leading to the preponderance of small Ro values. In fact, the majority of atmospheric and oceanic motions exhibit absolute Ro numbers sufficiently below unity, presenting values of Ro ~ 0.2 down to 0.01 (Cushman-Roisin and Beckers, 2011). Yet, by dividing the total mixing with the number of mixing occurrences in each bin a different pattern appears. Figure 5.3c clearly illustrates that most of the mixing occurs now, not at the low, but at the high Ro numbers and specifically for Ro $\mathcal{O}(1)$. The difference seen between panels (a) and (c) arises from the fact that the front occupies only a small part of the domain (Eastern Gotland Basin) and this domain fraction is not considered in panel (a).

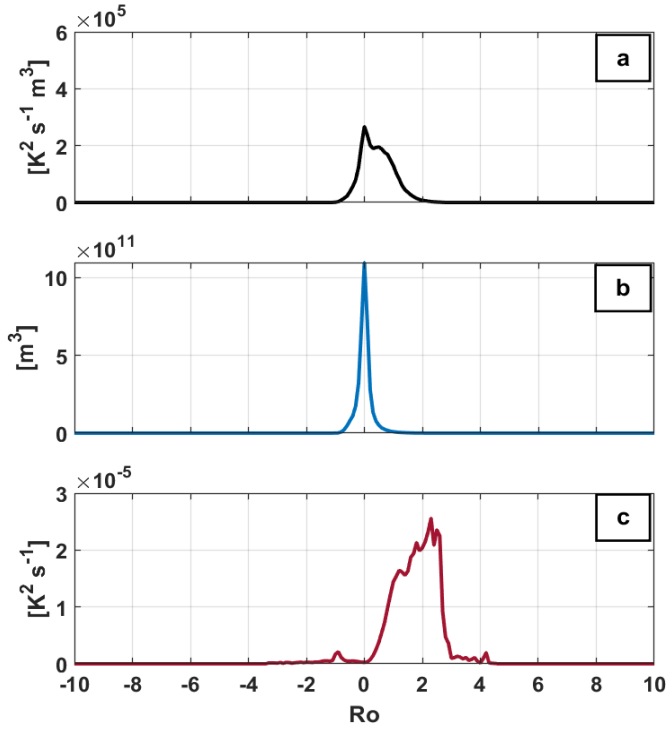

Figure 5.3: Binning of temperature mixing based on the Ro number. (a) Volume-integrated physical mixing, (b) volume per Rossby number class, (c) physical mixing. All panels concern upper-ocean mixing, extending from the surface until 5 m depth during the strong restratification phase on 19 October 2017.

The volume-integrated numerical mixing for the same date (Figure 5.4a) shows both positive and negative values with the latter corresponding to small Ro numbers and the former to processes characterized by large Ro. Similar findings were presented by Mohammadi-Aragh et al. (2015) that tested the behavior of various advection schemes, including Superbee, for configurations with different Ro numbers. By using an idealized re-entrant channel and performing lateral shear and baroclinic instability experiments, Mohammadi-Aragh et al. (2015) showed that during the restratification phase, when the lateral density gradients are strong, all advection schemes were globally diffusive in the configuration with Ro ~ 1, presenting also the same order of magnitude numerical diffusivities. The tendency of increased mixing in high Ro is more evident in panel (c) where the numerical mixing is clearly shifted towards the $\mathcal{O}(1)$ Ro numbers, in consistence with the physical one (Figure 5.3c). A comparison between Figures 5.3c and 5.4c shows also that the numerical mixing is less than the physical one when averaged values are considered instead of just snapshots like the one in Figure 5.1.

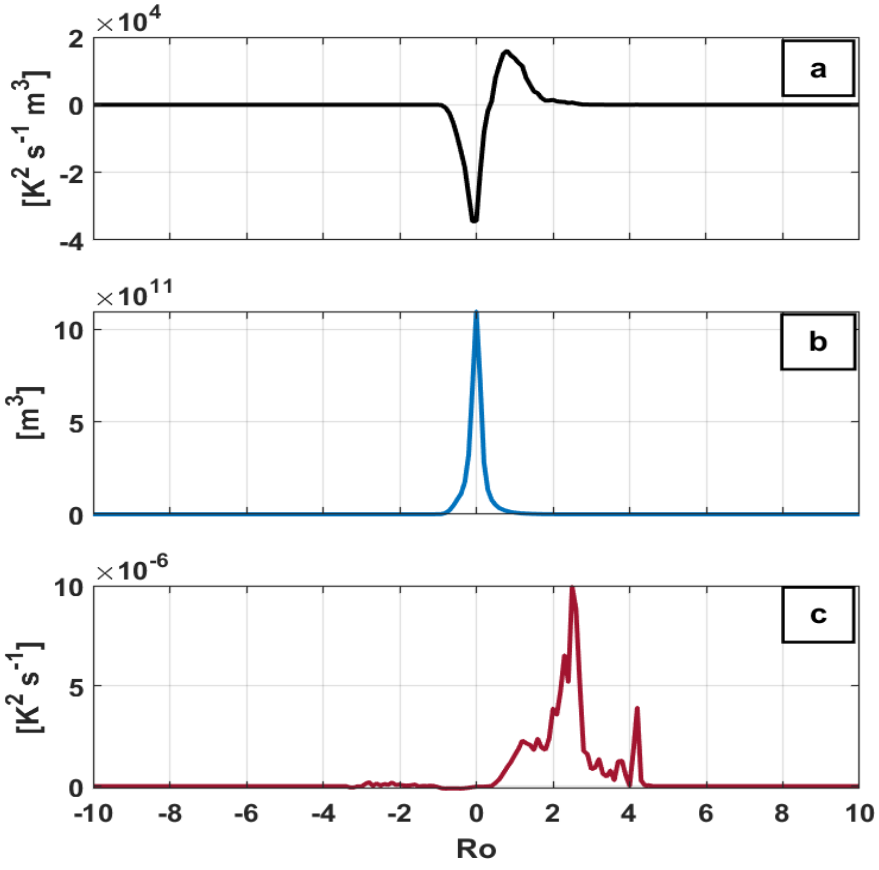

Figure 5.4: Same as Figure 5.3 but for the numerical mixing. Note that the scales are different from Figure 5.3

Figures 5.3 and 5.4 presented the mixing for a single day, during the restratification event that followed the first storm. To assess, the behavior of mixing during the entire period, Hovmöller diagrams of the physically and numerically induced mixing, were constructed based on the binning technique presented above. The Hovmöller diagrams correspond to the panels (c) of Figures 5.3, 5.4, where the fraction of the domain occupied by frontal features and ambient waters is also taken into consideration.

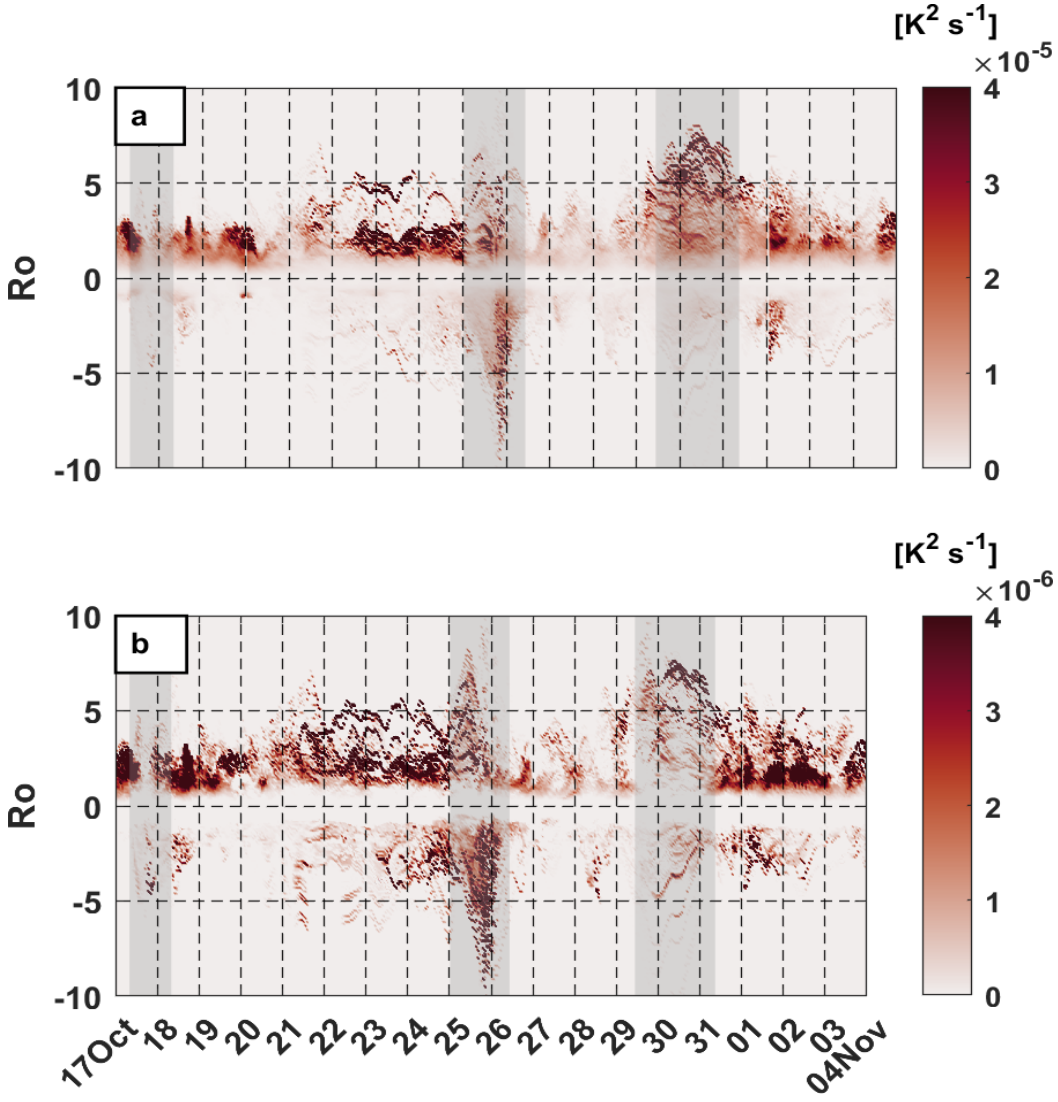

Figure 5.5: Hovmöller diagrams of mixing throughout the entire study period. (a) physically and (b) numerically induced mixing. The diagrams were constructed based on the calculations applied for Figures 5.3c and 5.4c. Both panels concern upper-ocean mixing, extending from the ocean surface until 5 m depth. Note that the scales are different between the two panels. Light gray shaded areas indicate the approximate duration of the three storm events.

While generally enhanced mixing occurs for Ro between 1 and 3, during the storm events maximum values appear at even higher Ro (~ 5). The numerical mixing presents generally the same pattern as the physical one but with values of one order of magnitude smaller. Interestingly, mixing is present mainly at the positive Ro during the entire period. This is most likely associated with the asymmetry in relative vorticity that has been observed in the upper-ocean when submesoscale flows are present. This skewness in ζ, seen also in Section 3.3.1 in the context of Figure 3.3, has been proposed by theoretical studies (Hoskins and Bretherton, 1972) based on potential vorticity conservation and has been further confirmed by shipboard velocity measurements (Rudnick, 2001; Shcherbina et al., 2013), drifter observations (Griffa et al., 2008) and numerical simulations (Boccaletti et al., 2007; Capet et al., 2008a; Klein et al., 2008).

By applying the same binning method to the MLD, it is obvious that MLD decreases substantially as Ro becomes $\mathcal{O}(1)$ (Figure 5.6). This implies the presence of strong lateral density gradients, that as seen in Chapter 4, act to continuously restratify the flow, resulting in MLD shoaling. In summary, the preceding analysis indicates that physical mixing is considerably stronger for $\mathcal{O}(1)$ Ro, when intense lateral density gradients are present. In this case, mixing is also shifted towards the positive Ro which may be related to the observed skewness in ζ. The physical and numerical mixing present the same patterns, partially with an opposite sign. Elevated values are found in frontal and filamentary patterns and along the outcropping of the isopycnals that mark the position of those features. Moreover, negative mixing was found to dominate in small Ro, where the horizontal gradients are weak and the highly diffusive first-order upstream part of the advection scheme is not so active. Vice-versa, a diffusive behavior in the advection scheme used here was detected for higher Ro values, in consistence with earlier findings (Mohammadi-Aragh et al., 2015).

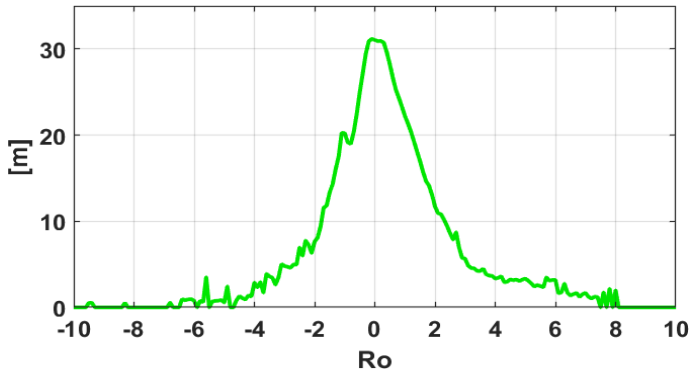

Figure 5.6: Binning of Mixed Layer Depth (MLD) during the entire study period (17 October until 3 November 2017) based on the near-surface Ro number.

5.2 Mixing efficiency in fronts

Turbulence and mixing in frontal regions are determined by a complex interplay between various processes enhancing turbulence (e.g., wind stress, buoyancy loss to the atmosphere, Ekman-induced buoyancy loss, frontal instabilities) and, on the other hand, by SML shoaling that has a tendency to suppress turbulence through restratification. A sensible parameter to quantify these two opposing effects on frontal turbulence is the mixing coefficient, ie.,

$$\Gamma = \frac{k_\rho N^2}{\varepsilon} \,, \tag{5.1}$$

where k_ρ denotes the vertical turbulent diffusivity, and ε the dissipation rate, both computed by the turbulence closure model. The mixing coefficient will be interpreted in the following as mixing efficiency. Previous studies have inferred that an increase in vertical stratification at a given turbulence level is reflected in an increase in Γ up to $\Gamma \approx 0.2 - 0.25$, whereas more energetic turbulence results in a reduction of Γ (see e.g., Shih et al., 2005). This behavior is also consistent with the properties of the second-moment turbulence model applied here (Canuto et al., 2001; Umlauf et al., 2003). As shown in Section 2.2, the turbulence model predicts $\Gamma = 0.22$ in equilibrium turbulence, not far from the canonical value of $\Gamma = 0.2$ (Osborn, 1980).

The horizontal structure of Γ in the SML right after the peak of the last storm (31 October), and during the succeeding restratification phase (3 November) is shown in Figure 5.7. A comparison between Figures 5.7b and 4.2b,d reveals a remarkable correspondence between the high positive Γ values on one hand and the sharp lateral buoyancy gradients and shallow mixed layers on the other. This correlation is especially evident in the area around 56.7°N and 18.7°-20.3°E, that is occupied by a strong filamentary feature with a zonal orientation. Likewise, in the northern part of the basin high mixing coefficients are observed inside an elongated thin filament (Figure 5.7a, marked by a black line). The filament, that started to develop during the passage of the 31 October wind episode disappeared almost completely three days later (Figure 5.7b). This reveals once again the ephemeral nature of submesoscale flows. A more detailed analysis of this filament is presented below. Clearly, in most parts of the basin gravitational instability dominates the flow yielding $\Gamma < 0$ or $N^2 < 0$, as seen in Chapter 3 in the context of Figure 3.5. This leads to unstable near-surface stratification that is more pronounced during nighttime (Figure 5.7a), although similar behavior can also be seen

even during the day (Figure 5.7b) since excessive cooling constitutes a quite typical condition for the Baltic Sea, throughout the period of interest (Reissmann et al., 2009). Unlike those unstable regions, most of the frontal areas remained stably stratified with a mixing coefficient often reaching up to $\Gamma = 0.2 - 0.25$.

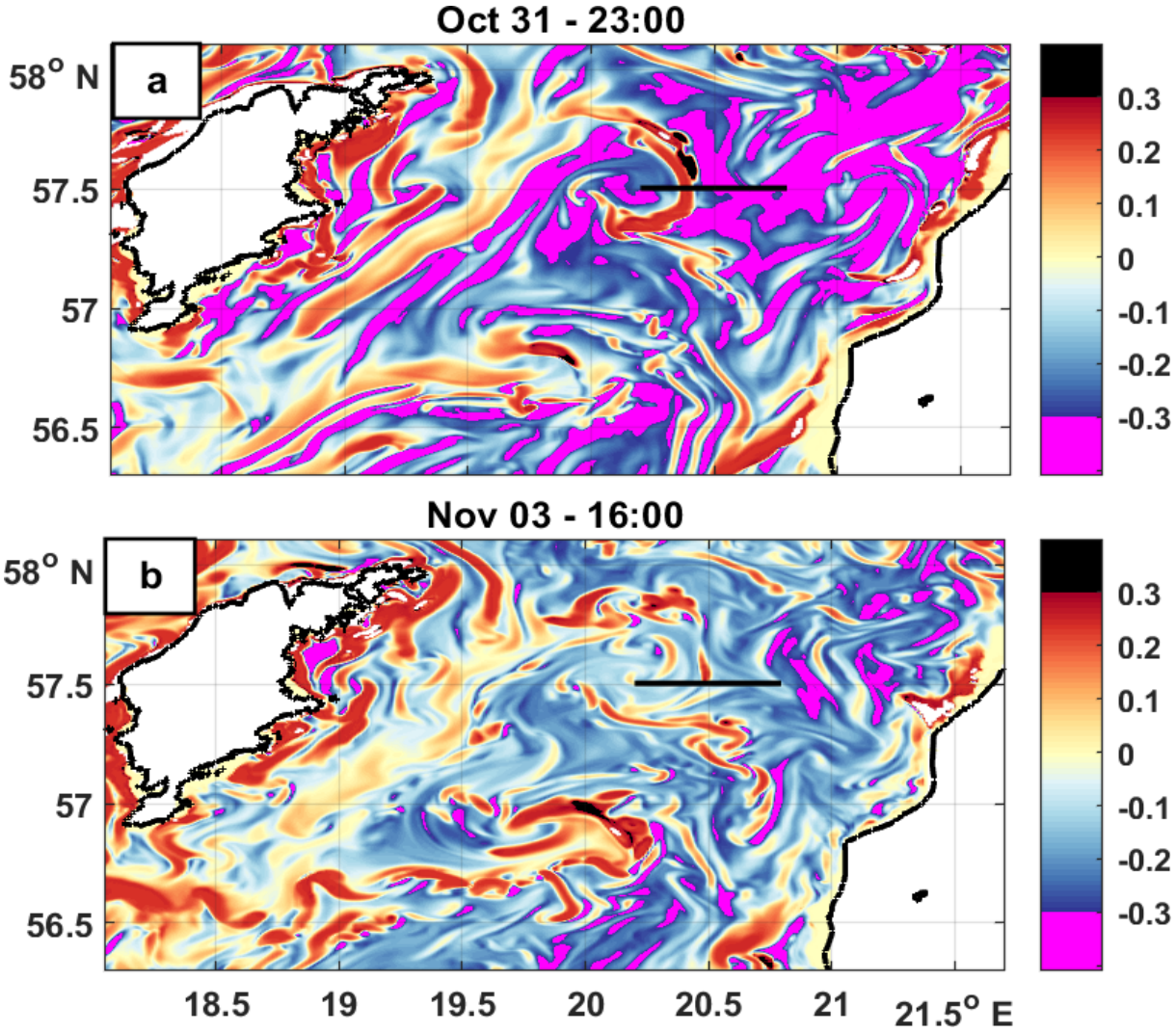

Figure 5.7: Mixing coefficient Γ (a) immediately after the peak of the final storm event, on 31 October and (b) during the restratification phase, on 03 November. Black line in panel (a) indicates the location of the cross-filament transect that is further examined in Figure 5.9. Panel (b) corresponds to the same instance in time as Figure 4.2b,d. Both panels show instantaneous fields at 10 m depth. Weakly-turbulent areas (white regions), where the turbulence model is not active anymore (turbulent kinetic energy smaller than $k_{\min} = 10^{-7}$ m^{2}s^{-2}, see Section 2.2), were excluded from the calculations.

The classical view of reduced stratification and vigorous turbulent mixing induced by atmospheric forcing can, therefore, be modified in the presence of fronts, where the dynamical slumping of the isopycnals can drive fast restratification. The implementation of the feature extraction technique, presented in Section 4.2, can provide detailed insights regarding the temporal evolution of the mixing coefficient inside frontal and non-frontal regions. Following the previously designated nomenclature ("Front" and "No-Front"), the fraction of unstable regions inside (blue) and outside (red) the frontal areas is presented in Figure 5.8a. Here, the unstable regions are defined as those areas where $N^2 < 0$, although the use of $\Gamma < 0$ approach would have been equivalent.

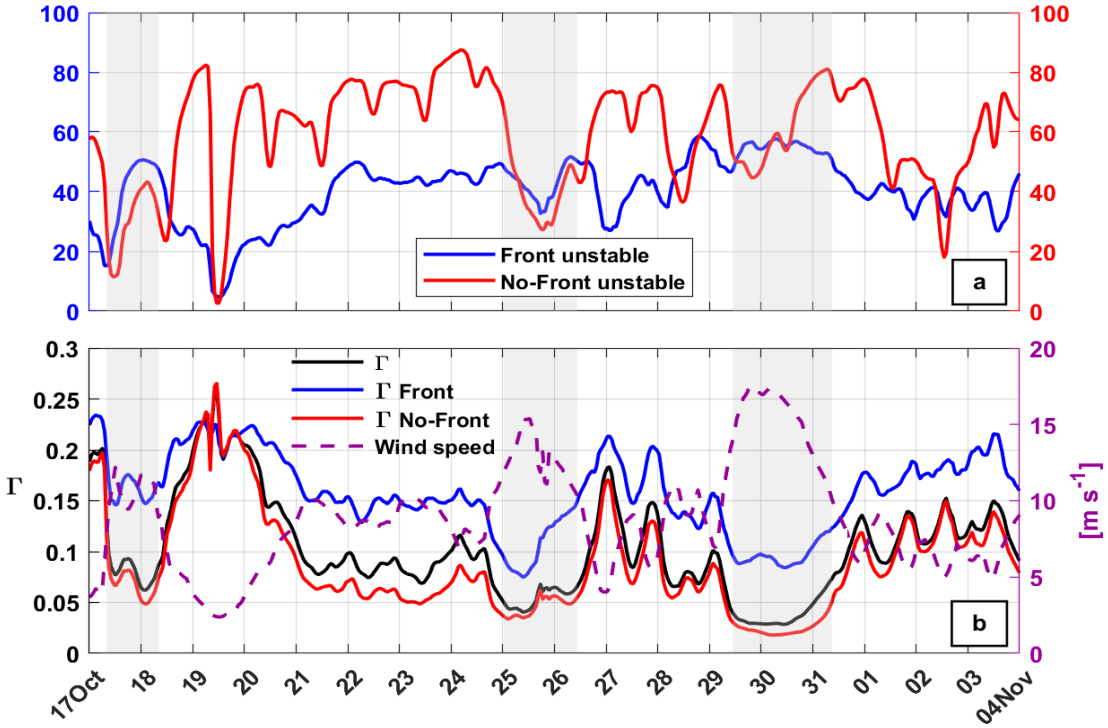

Figure 5.8: Temporal evolution of unstable areas and mixing coefficient, Γ. (a) Spatially averaged fraction of unstable areas in the presence (blue line, "Front") and absence (red line, "No-Front") of small-scale frontal features. The separation of the flow in "Front" and "No-Front" areas is based on the feature extraction method applied in Chapter 4, using the $|\nabla_h b|^2 > 10^{-13}$ s^{-4} threshold. (b) Spatially-averaged time-series of mixing coefficient, Γ (left axis), and wind speed (right axis). Γ for the entire domain, termed as "Γ" (black line), for the frontal structure, termed as "Γ Front" (blue), without the front, "Γ No-Front" (red) and wind speed (purple dashed line) for comparison. Only stable stratified areas ($\Gamma > 0$) are considered here to ease comparison. Also, weakly-turbulent areas, where the turbulence model is not active anymore (turbulent kinetic energy smaller than $k_{\min} = 10^{-7}$ m^{2}s^{-2}, see Section 2.2), were excluded from the calculations. Both panels concern 10 m depth with the light gray shaded areas indicating the approximate duration of the three successive storm episodes.

Outside the frontal regions, 60-80% of the near-surface region remained unstably stratified, except during the wind events, suggesting that surface-layer turbulence is at least partly driven by convection (Figure 5.8a). A clear diurnal cycle can be identified in these "No-Front" regions, indicating more wide-spread convection during nighttime, when atmospherically-driven restratification (i.e., SML heating) plays a smaller role. Stable stratification prevails in these areas only during conditions with extremely low winds, e.g. on 19 October. The frontal regions ("Front"), however, remained predominantly stratified almost throughout the entire period, implying that the persistent restratification can overwhelm the destratification effect of convection. This might also be the reason why a pronounced diurnal signal is not present there.

In order to evaluate the temporal evolution of the basin-averaged Γ, timeseries of "Front" and "No-Front" regions were constructed (Figure 5.8b). Note that only stably stratified regions are considered in Figure 5.8b, whereas weakly turbulent areas, where the turbulence model is not active anymore, were excluded from the calculations. It is evident that the effect of restratification inside the frontal regions (blue curve) is also imprinted in the mixing coefficient, displaying elevated values up to $\Gamma = 0.2 - 0.25$ throughout the entire study period (Figure 5.8b). Outside the frontal areas, however, enhanced values of Γ are only found on 19-20 October, when vertical mixing almost completely collapsed during an incident with extremely low wind conditions.

The well-known reduction of Γ in energetic, weakly stratified turbulence is reflected in the time-series of Γ and wind speed that present an inverse relationship, especially pronounced outside the frontal patterns. Yet, inside the frontal areas enhanced Γ values are maintained ($\Gamma \sim 0.1$) even during the passage of storms. For a location in the center of the SML during a storm event, this is a remarkably high value, suggesting that restratification induced by high lateral density gradients is able to compete with wind-driven and convective mixing also during periods with strong winds. Other studies have also reported efficient submesoscale restratification during storm conditions or periods with excessive cooling (Couvelard et al., 2015; Whitt and Taylor, 2017). Figure 5.8 thus highlights a complex interplay between (i) wind-induced mixing that reduces surface-layer stratification, (ii) atmospheric buoyancy loss that induces unstable stratification and turbulent convection, and (iii) restratification by lateral processes that tends to counteract both effects.

The vertical structure of submesoscale filaments can provide further insights into the effects of SML restratification on frontal turbulence. Although a plethora of filaments is evident in the Eastern Gotland Basin during the period of interest, the subsequent analysis focuses on an exemplary cold filament that appears in Figure 5.7a (marked by a black line), occupying the region from 56.9 to 57.8°N and from 18.7 to 20.5°E. This is a typical elongated submesoscale filament, presenting a mesoscale length and a submesoscale width of around 5 km. The filament, that started to develop during the last storm episode, sharpened when the wind started to subside and it quickly decayed after approximately three days (Figure 5.7b). Here, the focus is the northern tip of the filament that underwent strong filamentogenesis during this period (Figure 5.9).

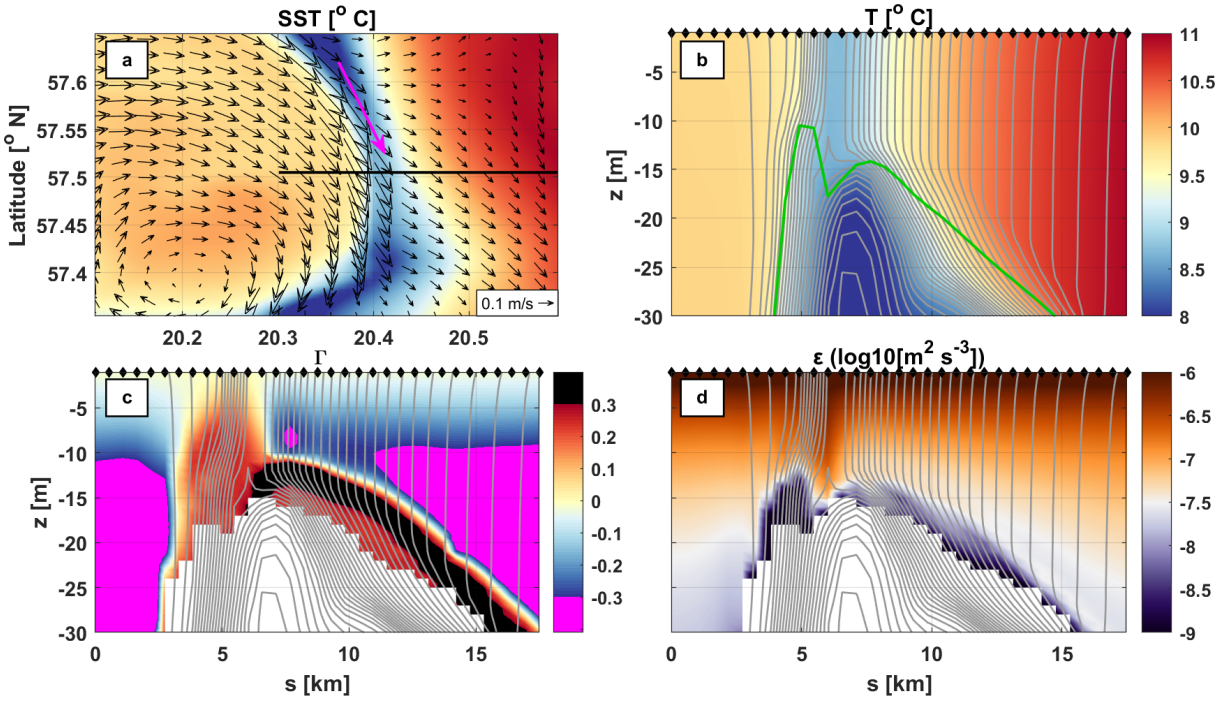

Figure 5.9: Instantaneous patterns of the dense submesoscale filament shown in Figure 5.7a. (a) Enlarged view of SST and surface circulation, and vertical sections of (b) temperature, (c) mixing coefficient, Γ, and (d) dissipation rate ε, along the black line shown in panel (a). The magenta arrow in panel (a) indicates the local direction of the wind speed relative to the orientation of the filament during the 31 October storm event (averaged from 08:00 to 20:00 UTC). The green line in panel (b) indicates the MLD. Gray contours denote isopycnals at 0.01 kg m^{-3} intervals. Black markers indicate the model resolution. Weakly-turbulent areas, where the turbulence model is not active anymore, were excluded (white areas).

As can be seen, by the horizontal patterns of SST and surface circulation (Figure 5.9a), the cold elongated filament sharpened as it got stretched and deformed by the local shear flow and a small anticyclonic eddy, that strengthened the filament unevenly, on its western side. The existence of this strong lateral density gradient in combination with the convergent strain field created favorable conditions for filamentogenesis, as has also been noted in previous studies (Capet et al., 2008b; Gula et al., 2014). At the western side of the filament, the filamentogenesis mechanism might have been enhanced further by "down-front" winds, during the passage of the preceding storm. This wind event, that passed over the field site a few hours earlier than the snapshot illustrated in Figure 5.9, was characterized by intense northerly winds (see magenta arrow in Figure 5.9a or Figure 3.1 for atmospheric conditions), and thus had a "down-front" component at the western side of the filament that acted to strengthen the gradients there, whereas the "up-front" component observed at the eastern side, served to decelerate the filament narrowing at that side (Thomas and Lee, 2005).

The strong lateral thermal gradients at the edges of the filament led to a local outcropping of the isopycnals from around 30 m depth (Figure 5.9b). The filament is relatively shallow and seems to be confined in the upper layers most likely due to the strong stratification that underlies the mixed layer and prohibits a deeper penetration. As expected, the MLD is substantially shallower in the center of the filament due to the effect of restratification (green line in Figure 5.9b). Stable stratification and enhanced values of Γ are detected inside the filament, while unstable stratification and a substantial contribution of convection to overall SML turbulence (note the small $\Gamma < -0.2$) are observed in large parts of the ambient waters.

The significant impact of submesoscale restratification on SML turbulence can be seen particularly clearly in the narrow front bounding the filament from West (3 km $< s <$ 6 km, approximately). While the mixing coefficient is only of the order of a few percent in the (nearly) well-mixed near-surface region ($z > -5$ m), it quickly increases up to maximum values around $\Gamma = 0.2 - 0.25$ at greater depth. There, the slightly tilting isopycnals imply a competition between restratification and mixing (Figure 5.9c). The strongest diapycnal mixing is therefore expected in the intermediate depth range (-12 m $< z < -5$ m), where the mixing coefficient is large (Figure 5.9c) and turbulence levels are still high (Figure 5.9d). For even greater depth, however, restratification becomes so strong that turbulence collapses (see purple and white areas in Figure 5.9d). While the mixing coefficient is still large in these regions, little diapycnal mixing is expected because turbulence is weak. The sheltering of the mixed layer by frontal and

filamentary features examined previously in the context of Figure 3.4e, appears also here, albeit not so pronounced. Inspection of Figure 5.9d shows lower dissipation rates in the area surrounding the filament compared with the ambient waters, especially on the strong western side of the filament. Overall, the preceding analysis illustrates an ambivalent impact of SML restratification on diapycnal mixing: restratification may increase diapycnal mixing by increasing the mixing efficiency in strongly turbulent regions that would otherwise be "well-mixed". But, on the other hand, if too strong, it may also result in a complete collapse of turbulence. The latter effect is seen to dominate here at greater depths.

CHAPTER 6

Conclusions

6.1 Summary and discussion

High-resolution remote sensing data indicate a plethora of submesoscale patterns in the SML of the Baltic Sea, evidenced by their imprint on the fine-scale structure of cyanobacteria blooms (see Figure 1.3). This suggests that this semi-enclosed brackish marine system forms an ideal natural laboratory for the study of submesoscale motions while pointing additionally to the importance of submesoscale structures for the dynamics of the marine ecosystems. Motivated by these observations, high-resolution realistic hindcast simulations were conducted, using a numerical ocean model to investigate the effects of submesoscale fronts and filaments on near-surface turbulence and Mixed Layer Depth (MLD) variations during storms. Thus previous idealized simulations (e.g., Nurser and Zhang, 2000; Boccaletti et al., 2007) were extended towards more realistic applications.

Before starting the submesoscale analysis, the numerical model was thoroughly validated in Chapter 2. The validation was based on available vertical temperature and salinity profiles, satellite images, and high-resolution microstructure temperature data collected across frontal and filamentary features during the field campaign. The com-

parison between the model results and remote sensing data showed that the model is able to capture the surface signature of submesoscale motions. The striking agreement found between an observed and a simulated transect across a typical cold submesoscale filament further indicates that the model resolution and setup are appropriate for the study of submesoscale motions.

In Chapter 3 the main characteristics of submesoscale motions were explored. A strong and persistent frontal structure was captured in the Eastern Gotland Basin for the first time. This sharp front was persistent throughout the entire autumn 2017, driven by the general cyclonic circulation in the basin and reinforced by upwelling favorable winds near the island of Gotland. In the vicinity of this frontal structure, the basin was found to be rich in cold elongated submesoscale filaments, indicating that lateral density gradients are instrumental for submesoscale genesis. The filaments presented horizontal widths of a few kilometers, a vertical scale of $\mathcal{O}$(10-100) m and lifetimes of a few days. These ephemeral features, abundant in the SML, were characterized by $\mathcal{O}(1)$ Ro and Ri_b, an indicator of ageostrophic dynamics with a preference in cyclonic vorticities, sharp lateral buoyancy gradients, intense surface convergence, and associated downwelling. The vertical velocities were remarkably large, reaching up to $\mathcal{O}(10^{-3})$ m s^{-1} during the filamentary intensification. As noted by McWilliams (2016), the vertical velocities induced by submesoscales are much higher than the ones found in mesoscale eddies. Studies (e.g., Lapeyre and Klein, 2006; Lévy et al., 2012; Mahadevan, 2016) have suggested that this secondary ageostrophic circulation might impact the air-sea gas exchange and transfer nutrients to the euphotic zone, affecting the upper-ocean biogeochemistry in localized areas.

The developed filaments were seen to strengthen significantly during upwelling favorable winds, with their density contrasts being largely controlled by the temperature differences. For the autumn conditions examined here, gravitational instability was the dominant term most of the days over the entire basin, as documented in Reissmann et al. (2009). During the periods of minimum buoyancy loss, a lateral zone emerged, consisting of more stratified waters in the western deeper parts of the basin when compared to the east. Leppäranta and Myrberg (2009) argued that, in the long-term mean, the strong bathymetric difference between the Latvian coast and the Gotland Deep can yield such a lateral zone with waters mixed down to the bottom in the shallower eastern parts of the Gotland Basin and relatively more stratified waters in the deeper western parts. A more careful investigation is needed, however, to determine whether the same explanation is valid and/or sufficient for the shorter time scales ex-

amined here. In the area of the front, stably stratified patches were forming inside the strong filaments with evidence of Symmetric Instability (SI) occurrence. These symmetrically unstable regions increased substantially during the first two storm episodes when strong "down-front" winds dominated the basin and largely decreased during the "up-front" winds of the last storm. The effect of excessive cooling and "down-front" winds on SI has been investigated in previous studies (e.g., Thomas et al., 2013b).

Submesoscale processes manifest different kinds of instabilities that have the ability to restratify the SML, by tilting the nearly vertical isopycnals towards the horizontal, allowing for SML shoaling. Forced symmetric instability, for example, a common feature of frontal areas (Thomas et al., 2013b) has a significant contribution to the upper-ocean stratification. However, its exact contribution cannot be evaluated with the numerical model applied here (because only the SI criteria can be simulated, see Chapter 3). Another instability with a restratification capacity is the Mixed Layer Instability (MLI). As described by Boccaletti et al. (2007), during the passage of a storm, increased winds may homogenize the upper ocean while maintaining the lateral density gradients. Once the wind subsides, surface cooling can generate gravitational overturning, that under the influence of planetary rotation, leads to a geostrophical adjusted state. This state is further susceptible to MLIs that can dynamically restratify the SML by slumping the nearly vertical isopycnals. During multiple sequential wind episodes, restratification can be achieved only if MLIs grow fast enough to compete with the destratifying effect of convection.

Independent of the instability type, the results presented in Chapter 4 indicate that a significant restratification and excessive shoaling takes place inside frontal and filamentary features, consistent with previous studies (Tandon and Garrett, 1994; Nurser and Zhang, 2000). The restratification generated a substantial difference (more than 30 m in some regions) in MLDs between the center of the filaments and the ambient waters. The shallowest MLDs coincided with the sharpest lateral buoyancy gradients. The simulations showed that these structures are able to create extremely shallow MLDs with significant spatial variability. It has been proposed that this variability in MLDs along with submesoscale stirring can create intense patchiness in plankton communities and affect the ecosystem functioning (Lévy et al., 2012; Mahadevan, 2016).

As one of the most important results of this thesis, it turned out that strong SML restratification and shoaling can be observed in the vicinity of submesoscale fronts even during strong wind events, underlining the real-ocean relevance of previous more ide-

alized configurations by Whitt and Taylor (2017) and Couvelard et al. (2015). The former, focusing on the effect of wind forcing, showed that submesoscales can maintain strong stratification even during intense "down-front" winds, by using large-eddy simulations, whereas the latter showed, by cooling an idealized turbulent jet, that submesoscale processes can limit the deepening of the MLD even during excessive cooling by balancing the destratifying effect of convection. Moreover, after each wind episode, a rapid and strong reduction of the MLD was observed within less than a day, pointing to the short time scales associated with submesoscale restratification. The shoaling was especially striking after the first storm where the combination of upwelling favorable winds and the following calm weather conditions contributed to the strengthening of the lateral buoyancy differences and the reinforcement of the restratification process. The bulk of the restratification was seen to occur in patches inside the sharpest fronts and filaments that emerged after the storm episodes. These features manage to counter-balance the destratifying effect of convection, yielding regions with shallow mixed layers.

The submesoscale restratification was also imprinted in the mixing coefficient Γ, typically used in field studies to relate observed dissipation rates to diapycnal mixing. Here, it was used as an indicator of the efficiency of mixing inside frontal regions. A remarkable correspondence was found between regions with large Γ values from one hand, and sharp lateral buoyancy gradients and shallow mixed layers from the other. One surprising finding of Chapter 5 was that, even during storm conditions with strong buoyancy loss, the SML remained stably stratified inside the strong small-scale frontal features, and mixing efficiencies were of the order of the canonical value for mixing in the stratified interior of the ocean ($\Gamma = 0.2$). This opposes the traditional view that near-surface mixing is generally inefficient because the SML is already well mixed. Considering that diapycnal mixing is comparable to cross-front mixing of different densities, the high Γ values inside submesoscale patterns may be relevant for the generation of density-compensated fronts that have been widely observed in the world's ocean (e.g., Rudnick and Ferrari, 1999). Outside the filamentary patterns, the SML remained unstably stratified, except during the wind events, suggesting that surface-layer turbulence is at least partly driven by convection. A clear diurnal cycle was identified in these regions, indicating a relatively more wide-spread convection during nighttime, when atmospheric heating plays a minor role. The frontal regions, however, presented a weak diurnal signal, implying that persistent restratification can overwhelm the destratification effect of convection. Within a typical submesoscale filament, Γ was found to increase with depth along with the increasing impact of restrat-

ification up to a point where turbulence was completely overwhelmed by stratification and collapsed. This process was shown to set the MLD inside sharp filaments. Overall, the findings suggest that high mixing efficiencies inside fronts result from the interplay between (i) wind-induced mixing that reduces surface-layer stratification, (ii) atmospheric buoyancy loss that induces unstable stratification and turbulent convection, and (iii) submesoscale restratification that tends to counteract both effects.

Using the diagnostic method of Burchard and Rennau (2008) the physical and the numerical mixing in the model were investigated. The physical mixing of temperature and the numerical mixing showed similar patterns, with maximum values detected in the frontal area and along the outcropping of the isopycnals, that mark the position of the frontal features. Using a binning technique based on the Ro number, it was shown that most of the physical mixing occurred at the relatively high Ro. The numerical mixing was positive for $\mathcal{O}(1)$ Ro and negative for Ro ~ 0, with an anti-dissipative behavior, as has been noted before (Mohammadi-Aragh, 2014). Interestingly, mixing was strongly skewed towards the positive Ro numbers which may be associated with the prevalence of cyclonic vorticities seen in Chapter 3. It is worth noting here that typically the Ro number is not considered sufficient for identifying submesoscale motions and thus, a combination of $\mathcal{O}(1)$ Ro and Ri_b would have been more accurate. Nonetheless, the analysis presented here clearly indicates the different mixing behaviors.

The results provided also new insights into the significance of submesoscales in the Baltic Sea, that despite their ubiquity, their properties and dynamics are still largely unexplored. Two notable exceptions are a study by Väli et al. (2017) who showed that upwelling events in the Gulf of Finland are associated with intense submesoscale activity and a recent study by Onken et al. (2020) who showed a plethora of submesoscale features in the western Baltic Sea. The high-resolution numerical simulations applied in this thesis revealed that the Eastern Gotland Basin, an area of major importance for the biogeochemistry of the entire Baltic Sea, contains a submesoscale active zone as well, associated with a strong and persistent frontal structure that had not been reported previously. The processes highlighted in this study, particularly the intense submesoscale vertical velocities and the ability of submesoscales to create stably localized patches with enhanced mixing efficiencies, introduce important implications for the biochemistry of the upper ocean.

Akin to the open ocean, the large vertical velocities induced by the submesoscale regime are expected to influence the air-sea gas exchange in the semi-enclosed Baltic

Sea, allowing for a possible increase in the anthropogenic carbon uptake. Moreover, earlier studies focusing on the Baltic Sea, e.g., Kahru et al. (1995) have shown that fronts are associated with increased cyanobacterial productivity and play a crucial role in cyanobacterial bloom formation. The submesoscale vertical velocities can also trigger plankton blooms by increasing the nutrient supply into the euphotic zone. According to Mahadevan (2016), whether the vertical velocities are strong enough to draw nutrients from the pycnocline and bring them to the upper layers, depends on the strength of the lateral density gradients and the depth of the outcropping.

In the Eastern Gotland Basin, it is possible that pumping of nutrients from the pycnocline to the surface, will not be significant in the strongly stratified deeper parts of the basin, but it can be important in the shallower areas. Although further research needs to be undertaken to estimate the material eddy fluxes in strongly stratified basins such as the Baltic Sea, recent satellite images have revealed that large cyanobacteria blooms in the basin can be associated with intense submesoscale activity (McWilliams, 2016). Submesoscale phytoplankton patchiness caused by horizontal stirring and vertical transport of nutrients within submesoscales (Lapeyre and Klein, 2006), is very often present in satellite images and has been extensively studied (Taylor and Ferrari, 2011; Lévy et al., 2012; Mahadevan, 2016). As noted by Taylor and Ferrari (2011), the reduced turbulent mixing, also seen in this thesis, and the increased light exposure due to the restratification process can also trigger blooms in areas where the nutrient depletion is not the primary issue. The significance of submesoscales on marine biology was further highlighted by Klein and Lapeyre (2009), suggesting that the vertical exchanges in submesoscale structures, can be one of the missing physical mechanisms that could close the nutrient budget, through enhanced vertical nutrient supply. Supposing that strong submesoscale motions that can substantially modify the MLD are ubiquitous in the world's ocean, parameterizations for the submesoscale restratification should be included in coupled climate models (Fox-Kemper et al., 2011) to reduce biases in the SML.

6.2 Future work

It has long been recognized that frontal regions in the Baltic Sea are associated with interleavings, intrusions, strong current shears, and mixing (Kahru et al., 1984). There, cyanobacterial blooms are also likely to form especially under the presence of intense submesoscale activity. Using the Baltic Sea as an easily accessible natural laboratory, future work should focus on clarifying the role of submesoscale features on biogeochemistry in non-tidal, strongly stratified systems like the Baltic Sea, along with their potential relation to cyanobacteria bloom formation. Further investigation using e.g., tracer release experiments or ocean biogeochemistry models can clarify to what extent submesoscale processes are relevant for the diapycnal transport of nutrients in basins where strong stratification underlies the surface mixed layer. The use of slowly rising Lagrangian tracers mimicking cyanobacteria could also be used to test to what degree the surface patterns observed from space (see e.g., Figure 1.2) can be reproduced by the model.

Studies have shown that contrary to mesoscale structures submesoscales exhibit a clear seasonal cycle with increased activity during the wintertime when the mixed layer, which serves as an energy supply, is deep (Mensa et al., 2013; Brannigan et al., 2015). It would thus be interesting to investigate the seasonality of those features and the overall significance of submesoscale restratification in different sub-basins of the Baltic Sea and compare the potential regional differences in each sub-basin. Since this thesis focused only on a limited period during autumn 2017, a study with longer time periods can also shed some light on the duration and/or seasonality of the main frontal structure that seemed to persist throughout fall. This could also help to clarify the processes that control the generation and the position of the frontal pattern that here was seen to be largely aligned with the isobaths.

Moreover, during the EMB169 field campaign turbulence microstructure measurements were collected using an ocean glider. The measurements were taken after the 25 October wind event and showed that fronts can shelter and damp turbulence in the SML, while simultaneously generating turbulence through instabilities. A future study could, therefore, combine those in situ data with the numerical simulations in order to better understand the evolution of those processes. An example of this "sheltering" effect, as seen by the numerical simulations, was provided in the context of Figure 3.4e.

Using a box model and available observations Burchard et al. (2017) showed that under the influence of upwelling-favorable winds during summer, salinity inversions can occur in the Eastern Gotland Basin, leading to the formation of localized patches characterized by salinity minima. It would thus be of interest to further examine whether submesoscales are present during those inversions and to what extent they can contribute to the generation of this observed salinity minima through subduction of surface waters.

Bibliography

Becherer, J.K., Umlauf, L., 2011. Boundary mixing in lakes: 1. Modeling the effect of shear-induced convection. Journal of Geophysical Research: Oceans 116.

Blumberg, A.F., Mellor, G.L., 1987. A description of a three-dimensional coastal ocean circulation model. Three-dimensional coastal ocean models , 1–16.

Boccaletti, G., Ferrari, R., Fox-Kemper, B., 2007. Mixed Layer Instabilities and Restratification. Journal of Physical Oceanography 37, 2228–2250.

Brannigan, L., Marshall, D.P., Naveira-Garabato, A., George Nurser, A.J., 2015. The seasonal cycle of submesoscale flows. Ocean Modelling 92, 69–84.

Brannigan, L., Marshall, D.P., Naveira Garabato, A.C., Nurser, A.J.G., Kaiser, J., 2017. Submesoscale Instabilities in Mesoscale Eddies. Journal of Physical Oceanography 47, 3061–3085.

Brüggemann, N., Eden, C., 2015. Routes to dissipation under different dynamical conditions. Journal of Physical Oceanography 45, 2149–2168.

Burchard, H., Basdurak, N.B., Gräwe, U., Knoll, M., Mohrholz, V., Müller, S., 2017. Salinity inversions in the thermocline under upwelling favorable winds. Geophysical Research Letters 44, 1422–1428.

Burchard, H., Baumert, H., 1995. On the performance of a mixed-layer model based on the k-ε turbulence closure. Journal of Geophysical Research: Oceans 100, 8523–8540.

Burchard, H., Beckers, J.M., 2004. Non-uniform adaptive vertical grids in one-dimensional numerical ocean models. Ocean Modelling 6, 51–81.

Burchard, H., Bolding, K., 2002. GETM: A general estuarine transport model. Tech. Rep. EUR 20253 EN, Eur. Comm. , 157.

Burchard, H., Bolding, K., Feistel, R., Gräwe, U., Klingbeil, K., MacCready, P., Mohrholz, V., Umlauf, L., [van der Lee], E.M., 2018. The Knudsen theorem and the Total Exchange Flow analysis framework applied to the Baltic Sea. Progress in Oceanography 165, 268–286.

Burchard, H., Hetland, R.D., 2010. Quantifying the contributions of tidal straining and gravitational circulation to residual circulation in periodically stratified tidal estuaries. Journal of Physical Oceanography 40, 1243–1262.

Burchard, H., Hetland, R.D., Schulz, E., Schuttelaars, H.M., 2011. Drivers of residual estuarine circulation in tidally energetic estuaries: Straight and irrotational channels with parabolic cross section. Journal of Physical Oceanography 41, 548–570.

Burchard, H., Janssen, F., Bolding, K., Umlauf, L., Rennau, H., 2009. Model simulations of dense bottom currents in the Western Baltic Sea. Continental Shelf Research 29, 205–220.

Burchard, H., Rennau, H., 2008. Comparative quantification of physically and numerically induced mixing in ocean models. Ocean Modelling 20, 293–311.

Callies, J., Barkan, R., Garabato, A.N., 2020. Time Scales of Submesoscale Flow Inferred from a Mooring Array. Journal of Physical Oceanography 50, 1065–1086.

Callies, J., Flierl, G., Ferrari, R., Fox-Kemper, B., 2016. The role of mixed-layer instabilities in submesoscale turbulence. J. Fluid Mech 788, 5–41.

Canuto, V.M., Howard, A., Cheng, Y., Dubovikov, M.S., 2001. Ocean turbulence. Part I: One-point closure model-momentum and heat vertical diffusivities. Journal of Physical Oceanography 31, 1413–1426.

Capet, X., McWilliams, J.C., Molemaker, M.J., Shchepetkin, A.F., 2008a. Mesoscale to submesoscale transition in the California Current system. Part I: Flow Structure, Eddy Flux, and Observational Tests. Journal of Physical Oceanography 38, 29–43.

Capet, X., McWilliams, J.C., Molemaker, M.J., Shchepetkin, A.F., 2008b. Mesoscale to submesoscale transition in the California Current system. Part II: Frontal processes. Journal of Physical Oceanography 38, 44–64.

Capet, X., McWilliams, J.C., Molemaker, M.J., Shchepetkin, A.F., 2008c. Mesoscale to submesoscale transition in the California current system. Part III: Energy balance and flux. Journal of Physical Oceanography 38, 2256–2269.

Carpenter, J.R., Rodrigues, A., Schultze, L.K., Merckelbach, L.M., Suzuki, N., Umlauf, L., 2020. Shear instability and turbulence within a submesoscale front following a storm. Unpublished paper.

Charney, J.G., 1971. Geostrophic turbulence. Journal of the Atmospheric Sciences 28, 1087–1095.

Couvelard, X., Dumas, F., Garnier, V., Ponte, A.L., Talandier, C., Treguier, A.M., 2015. Mixed layer formation and restratification in presence of mesoscale and submesoscale turbulence. Ocean Modelling 96, 243–253.

Cronin, M., Sprintall, J., 2001. Wind And Buoyancy-forced Upper Ocean. Encyclopedia of Ocean Sciences , 3219–3226.

Csanady, G.T., 1978. Wind effects on surface to bottom fronts. Journal of Geophysical Research: Oceans 83, 4633–4640.

Cushman-Roisin, B., Beckers, J.M., 2011. in: Cushman-Roisin, B., Beckers, J.M. (Eds.), Introduction to Geophysical Fluid Dynamics. Academic Press. volume 101 of *International Geophysics*, pp. 521 – 551.

D'Asaro, E., Lee, C., Rainville, L., Harcourt, R., Thomas, L., 2011. Enhanced turbulence and energy dissipation at ocean fronts. Science (New York, N.Y.) 332, 318–22.

de Boyer Montégut, C., Madec, G., Fischer, A.S., Lazar, A., Iudicone, D., 2004. Mixed layer depth over the global ocean: An examination of profile data and a profile-based climatology. Journal of Geophysical Research: Oceans 109, 1–20.

Fairall, C.W., Bradley, E.F., Hare, J.E., Grachev, A.A., Edson, J.B., 2003. Bulk parameterization of air-sea fluxes: Updates and verification for the COARE algorithm. Journal of Climate 16, 571–591.

Fennel, W., Seifert, T., Kayser, B., 1991. Rossby radii and phase speeds in the Baltic Sea. Continental Shelf Research 11, 23–36.

Ferrari, R., Wunsch, C., 2009. Ocean Circulation Kinetic Energy: Reservoirs, Sources, and Sinks. Annual Review of Fluid Mechanics 41, 253–282.

Fox-Kemper, B., Danabasoglu, G., Ferrari, R., Griffies, S.M., Hallberg, R.W., Holland, M.M., Maltrud, M.E., Peacock, S., Samuels, B.L., 2011. Parameterization of mixed layer eddies. III: Implementation and impact in global ocean climate simulations. Ocean Modelling 39, 61–78.

Fox-Kemper, B., Ferrari, R., Hallberg, R., 2008. Parameterization of Mixed Layer Eddies. Part I: Theory and Diagnosis. Journal of Physical Oceanography 38, 1145–1165.

Galperin, B., Kantha, L.H., Hassid, S., Rosati, A., 1988. A quasi-equilibrium turbulent energy model for geophysical flows. Journal of the Atmospheric Sciences 45, 55–62.

Garrett, C., 1996. Processes in the surface mixed layer of the ocean. Dynamics of Atmospheres and Oceans 23, 19–34.

Gräwe, U., Holtermann, P., Klingbeil, K., Burchard, H., 2015. Advantages of vertically adaptive coordinates in numerical models of stratified shelf seas. Ocean Modelling 92, 56–68.

Gräwe, U., Klingbeil, K., Kelln, J., Dangendorf, S., 2019. Decomposing mean sea level rise in a semi-enclosed basin, the Baltic Sea. Journal of Climate 32, 3089–3108.

Griffa, A., Lumpkin, R., Veneziani, M., 2008. Cyclonic and anticyclonic motion in the upper ocean. Geophysical Research Letters 35.

Gula, J., Molemaker, M.J., McWilliams, J.C., 2014. Submesoscale Cold Filaments in the Gulf Stream. Journal of Physical Oceanography 44, 2617–2643.

Gula, J., Molemaker, M.J., McWilliams, J.C., 2015. Topographic vorticity generation, submesoscale instability and vortex street formation in the Gulf Stream. Geophysical Research Letters 42, 4054–4062.

Haine, T.W.N., Marshall, J., 1998. Gravitational, symmetric, and baroclinic instability of the ocean mixed layer. Journal of Physical Oceanography 28, 634–658.

Hofmeister, R., Beckers, J.M., Burchard, H., 2011. Realistic modelling of the exceptional inflows into the central Baltic Sea in 2003 using terrain-following coordinates. Ocean Modelling 39, 233–247.

Hofmeister, R., Burchard, H., Beckers, J.M., 2010. Non-uniform adaptive vertical grids for 3D numerical ocean models. Ocean Modelling 33, 70–86.

Holtermann, P., Burchard, H., Gräwe, U., Klingbeil, K., Umlauf, L., 2014. Deep-water dynamics and boundary mixing in a nontidal stratified basin: A modeling study of the Baltic Sea. Journal of Geophysical Research : Oceans , 3134–3157.

Holtermann, P., Umlauf, L., Tanhua, T., Schmale, O., Rehder, G., Waniek, J.J., 2012. The Baltic Sea Tracer Release Experiment: 1. Mixing rates. Journal of Geophysical Research: Oceans 117, 1–18.

Hoskins, B.J., 1974. The role of potential vorticity in symmetric stability and instability. Quarterly Journal of the Royal Meteorological Society 100, 480–482.

Hoskins, B.J., 1982. The mathematical theory of frontogenesis. Annual review of fluid mechanics. Volume 14 , 131–151.

Hoskins, B.J., Bretherton, F.P., 1972. Atmospheric Frontogenesis Models: Mathematical Formulation and Solution. Journal of the Atmospheric Sciences 29, 11–37.

J. Pavelson, 1988. Nature and some characteristics of thermohaline fronts in the Baltic Proper, in: Proceedings of the 16th Conference of the Baltic Oceanographers, Kiel, pp. 796–805.

Kahru, M., Elken, J., Kotta, I., Simm, M., Vilbaste, K., 1984. Plankton distributions and processes across a front in the open Baltic Sea. Marine Ecology Progress Series 20, 101–111.

Kahru, M., Håkansson, B., Rud, O., 1995. Distributions of the sea-surface temperature fronts in the Baltic Sea as derived from satellite imagery. Continental Shelf Research 15, 663–679.

Karimova, S., 2012. Spiral eddies in the Baltic, Black and Caspian seas as seen by satellite radar data. Advances in Space Research 50, 1107–1124.

Klein, P., Hua, B.L., Lapeyre, G., Capet, X., Le Gentil, S., Sasaki, H., 2008. Upper ocean turbulence from high-resolution 3D simulations. Journal of Physical Oceanography 38, 1748–1763.

Klein, P., Lapeyre, G., 2009. The Oceanic Vertical Pump Induced by Mesoscale and Submesoscale Turbulence. Annual Review of Marine Science 1, 351–375.

Klingbeil, K., Mohammadi-Aragh, M., Gräwe, U., Burchard, H., 2014. Quantification of spurious dissipation and mixing - Discrete variance decay in a finite-Volume framework. Ocean Modelling 81, 49–64.

Kondo, J., 1975. Air-sea bulk transfer coefficients in diabatic conditions. Boundary-Layer Meteorology 9, 91–112.

Kononen, K., Nômmann, S., 1992. Spatio-Temporal Dynamics of the Cyanobacterial Blooms in the Gulf of Finland, Baltic Sea. In: Marine Pelagic Cyanobacteria: Trichodesmium and other Diazotrophs. Springer Netherlands, Dordrecht. pp. 95–113.

Lapeyre, G., Klein, P., 2006. Impact of the small-scale elongated filaments on the oceanic vertical pump. Journal of Marine Research 64, 835–851.

Large, W.G., McWilliams, J.C., Doney, S.C., 1994. Oceanic vertical mixing: A review and a model with a nonlocal boundary layer parameterization.

Leppäranta, M., Myrberg, K., 2009. Physical oceanography of the Baltic Sea. volume 378. Springer Berlin Heidelberg, Berlin, Heidelberg.

Lévy, M., Ferrari, R., Franks, P.J., Martin, A.P., Rivière, P., 2012. Bringing physics to life at the submesoscale. Geophysical Research Letters 39.

Mahadevan, A., 2016. The Impact of Submesoscale Physics on Primary Productivity of Plankton. Annual Review of Marine Science 8, 161–184.

Mahadevan, A., Tandon, A., 2006. An analysis of mechanisms for submesoscale vertical motion at ocean fronts. Ocean Modelling 14, 241–256.

Mahadevan, A., Tandon, A., Ferrari, R., 2010. Rapid changes in mixed layer stratification driven by submesoscale instabilities and winds. Journal of Geophysical Research: Oceans 115.

McWilliams, J.C., 2016. Submesoscale currents in the ocean. Proceedings of the Royal Society A: Mathematical, Physical and Engineering Science 472, 20160117.

McWilliams, J.C., 2019. A survey of submesoscale currents. Geoscience Letters 6.

McWilliams, J.C., Colas, F., Molemaker, M.J., 2009. Cold filamentary intensification and oceanic surface convergence lines. Geophysical Research Letters 36, L18602.

McWilliams, J.C., Gula, J., Jeroen Molemaker, M., Renault, L., Shchepetkin, A.F., 2015. Filament frontogenesis by boundary layer turbulence. Journal of Physical Oceanography 45, 1988–2005.

Meier Markus, H.E., 2007. Modeling the pathways and ages of inflowing salt- and freshwater in the Baltic Sea. Estuarine, Coastal and Shelf Science 74, 610–627.

Mensa, J.A., Garraffo, Z., Griffa, A., Özgökmen, T.M., Haza, A., Veneziani, M., 2013. Seasonality of the submesoscale dynamics in the Gulf Stream region. Ocean Dynamics 63, 923–941.

Mohammadi-Aragh, M., 2014. The impact of advection schemes on lateral shear and baroclinic instability. PhD dissertation. University of Hamburg.

Mohammadi-Aragh, M., Goessling, H.F., Losch, M., Hutter, N., Jung, T., 2018. Predictability of Arctic sea ice on weather time scales. Scientific Reports 8, 1–7.

Mohammadi-Aragh, M., Klingbeil, K., Brüggemann, N., Eden, C., Burchard, H., 2015. The impact of advection schemes on restratifiction due to lateral shear and baroclinic instabilities. Ocean Modelling 94, 112–127.

Mohammadi-Aragh, M., Losch, M., Goessling, H.F., 2020. Comparing arctic sea ice model simulations to satellite observations by multiscale directional analysis of linear kinematic features. Monthly Weather Review .

Molemaker, M.J., McWilliams, J.C., Capet, X., 2010. Balanced and unbalanced routes to dissipation in an equilibrated Eady flow. Journal of Fluid Mechanics 654, 35–63.

Molemaker, M.J., McWilliams, J.C., Yavneh, I., 2005. Baroclinic instability and loss of balance. Journal of Physical Oceanography 35, 1505–1517.

Munk, W., Armi, L., Fischer, K., Zachariasen, F., 2000. Spirals on the sea. Proceedings of the Royal Society A: Mathematical, Physical and Engineering Sciences 456, 1217–1280.

Nurser, A.J.G., Zhang, J.W., 2000. Eddy-induced mixed layer shallowing and mixed layer/thermocline exchange. Journal of Geophysical Research: Oceans 105, 21851–21868.

Okubo, A., 1970. Horizontal dispersion of floatable particles in the vicinity of velocity singularities such as convergences. Deep-Sea Research and Oceanographic Abstracts 17, 445–454.

Onken, R., Baschek, B., Angel-Benavides, I.M., 2020. Very high-resolution modelling of submesoscale turbulent patterns and processes in the baltic sea. Ocean Science 16, 657–684.

Osborn, T.R., 1980. Estimates of the local rate of vertical diffusion from dissipation measurements. Journal of Physical Oceanography 10, 83–89.

Pavelson, J., Laanemets, J., Kononen, K., Nõmmann, S., 1997. Quasi-permanent density front at the entrance to the Gulf of Finland: Response to wind forcing. Continental Shelf Research 17, 253–265.

Peng, J.P., Holtermann, P., Umlauf, L., 2020. Frontal Instability and Energy Dissipation in a Submesoscale Upwelling Filament. Journal of Physical Oceanography 50, 2017–2035.

Pietrzak, J., 1998. The use of TVD limiters for forward-in-time upstream-biased advection schemes in ocean modeling. Monthly Weather Review 126, 812–830.

Placke, M., Meier, H.E., Gräwe, U., Neumann, T., Frauen, C., Liu, Y., 2018. Long-term mean circulation of the Baltic Sea as represented by various ocean circulation models. Frontiers in Marine Science 5, 287.

Reissmann, J.H., Burchard, H., Feistel, R., Hagen, E., Lass, H.U., Mohrholz, V., Nausch, G., Umlauf, L., Wieczorek, G., 2009. Vertical mixing in the Baltic Sea and consequences for eutrophication - A review. Progress in Oceanography 82, 47–80.

Rudnick, D.L., 2001. On the skewness of vorticity in the upper ocean. Geophysical Research Letters 28, 2045–2048.

Rudnick, D.L., Ferrari, R., 1999. Compensation of horizontal temperature and salinity gradients in the ocean mixed layer. Science 283, 526–529.

Shcherbina, A.Y., D'Asaro, E.A., Lee, C.M., Klymak, J.M., Molemaker, M.J., McWilliams, J.C., 2013. Statistics of vertical vorticity, divergence, and strain in a developed submesoscale turbulence field. Geophysical Research Letters 40, 4706–4711.

Shih, L.H., Koseff, J.R., Ivey, G.N., Ferziger, J.H., 2005. Parameterization of turbulent fluxes and scales using homogeneous sheared stably stratified turbulence simulations. Journal of Fluid Mechanics 525, 193–214.

Siegelman, L.I., 2020. Energetic submesoscale dynamics in the ocean interior. Journal of Physical Oceanography 50, 727–749.

Smagorinsky, J., 1963. General Circulation Experiments With the Primitive Equations. Monthly Weather Review 91, 99–164.

Stamper, M.A., Taylor, J.R., 2017. The transition from symmetric to baroclinic instability in the Eady model. Ocean Dynamics 67, 65–80.

Su, Z., Wang, J., Klein, P., Thompson, A.F., Menemenlis, D., 2018. Ocean submesoscales as a key component of the global heat budget. Nature Communications 9, 775.

Sullivan, P.P., McWilliams, J.C., 2018. Frontogenesis and frontal arrest of a dense filament in the oceanic surface boundary layer. Journal of Fluid Mechanics 837, 341–380.

Tandon, A., Garrett, C., 1994. Mixed Layer Restratification Due to a Horizontal Density Gradient. Journal of Physical Oceanography 24, 1419–1424.

Taylor, J.R., Ferrari, R., 2009. On the equilibration of a symmetrically unstable front via a secondary shear instability. Journal of Fluid Mechanics 622, 103–113.

Taylor, J.R., Ferrari, R., 2010. Buoyancy and wind-driven convection at mixed layer density fronts. Journal of Physical Oceanography 40, 1222–1242.

Taylor, J.R., Ferrari, R., 2011. Ocean fronts trigger high latitude phytoplankton blooms. Geophysical Research Letters 38, 1–5.

Thomas, L.N., Lee, C.M., 2005. Intensification of Ocean Fronts by Down-Front Winds. Journal of Physical Oceanography 35, 1086–1102.

Thomas, L.N., Tandon, A., Mahadevan, A., 2013a. Submesoscale Processes and Dynamics. American Geophysical Union (AGU). pp. 17–38.

Thomas, L.N., Taylor, J.R., D'Asaro, E.A., Lee, C.M., Klymak, J.M., Shcherbina, A., 2016. Symmetric instability, inertial oscillations, and turbulence at the Gulf Stream front. Journal of Physical Oceanography 46, 197–217.

Thomas, L.N., Taylor, J.R., Ferrari, R., Joyce, T.M., 2013b. Symmetric instability in the Gulf Stream. Deep-Sea Research Part II: Topical Studies in Oceanography 91, 96–110.

Ullman, D.S., Cornillon, P.C., 1999. Satellite-derived sea surface temperature fronts on the continental shelf off the northeast US coast. Journal of Geophysical Research: Oceans 104, 23459–23478.

Ullman, D.S., Cornillon, P.C., 2001. Continental shelf surface thermal fronts in winter off the northeast US coast. Continental Shelf Research 21, 1139 – 1156.

Umlauf, L., Burchard, H., 2005. Second-order turbulence closure models for geophysical boundary layers. A review of recent work. Continental Shelf Research 25, 795–827.

Umlauf, L., Burchard, H., Hutter, K., 2003. Extending the k-ω turbulence model towards oceanic applications. Ocean Modelling 5, 195–218.

Väli, G., Zhurbas, V., Lips, U., Laanemets, J., 2017. Submesoscale structures related to upwelling events in the Gulf of Finland, Baltic Sea (numerical experiments). Journal of Marine Systems 171, 31 – 42.

Vortmeyer-Kley, R., Holtermann, P., Feudel, U., Gräwe, U., 2019. Comparing Eulerian and Lagrangian eddy census for a tide-less, semi-enclosed basin, the Baltic Sea. Ocean Dynamics 69, 701–717.

Whitt, D.B., Taylor, J.R., 2017. Energetic Submesoscales Maintain Strong Mixed Layer Stratification during an Autumn Storm. Journal of Physical Oceanography 47, 2419–2427.